UNIVERSITY OF CALIFORNIA
SANTA CRUZ

INVESTIGATING UPGRADE OPTIONS FOR A HIGH REPETITION RATE, ULTRA-LOW EMITTANCE ELECTRON PHOTOINJECTORS

A dissertation submitted in partial satisfaction of the
requirements for the degree of

DOCTOR OF PHILOSOPHY

in

PHYSICS

by

Nora Norvell

December 2022

The Dissertation of Nora Norvell
is approved:

Professor Bruce Schumm, Chair

Professor Steven Ritz

Professor Jason Nielsen

Peter Biehl
Vice Provost and Dean of Graduate Studies

Table of Contents

List of Figures

List of Tables

Abstract

Investigating Upgrade Options for a High Repetition Rate, Ultra-Low Emittance Electron Photoinjectors

by

Nora Norvell

As accelerator breakthroughs progress, Accelerator Physicists are greatly concerned with managing the so-called emittance of a particle beams. Emittance is defined as the momentum and position phase space area of a particle beam and is associated with the ability to focus and concentrate a beam. In general, lower emittance means higher beam quality. We care about emittance as it dictates many other key parameters that predict the success of an accelerator project. Collider experiments desire low emittance for higher luminosity, yielding more collisions to record. For free electron lasers (FEL), emittance directly determines how efficiently the electron beam microbunches, as microbunching is required to start the exponential growth of x-ray production in undulator magnets.

As FELs become more popular and scientifically in demand, the FEL user community is pushing for higher x-ray energies and higher repetition rates to enable new science. This presents a huge challenge for the accelerator community as the high repetition rate requirement coupled with the need for an ultra-low emittance beam is currently limiting the range of FELs. This dissertation explores this bottleneck for high repetition rate FEL light sources with the focus on a notable case study: SLAC's Linac Coherent Light Source II (LCLS-II). Simulations predict that decreasing the emittance at the undulators from the current estimate of 0.4 mm mrad to 0.1 mm mrad would expand SLACs LCLS-II x-ray energy upper bound from 15 keV to 22 keV. The benefit from lower emittance is even more pronounced for further linac energy upgrades.

With the LCLS-II emittance goals in mind, in this dissertation, I investigate emittance improvements for an electron injector system for FEL-like applications that would satisfy a high repetition rate requirement. I focused on two areas of potential improvement: using a Superconducting RF (SRF) gun cavity with a higher RF gradient on the cathode, or a higher quality cathode that produces a lower initial electron momentum distribution. I started with a detailed simulation study that decouples gun cavity improvements from cathode improvements. To do this, I utilized a genetic algorithm to optimize various injector lattices at different cathode qualities. I demonstrate that to realistically meet the demands of the FEL community, we will need both the higher gun gradients of SRF guns as well as improvements from the cathode.

I next present work on developing the solenoid component for a SRF gun developed at KEK in Japan to advance SRF gun cavity technology. I lay out the steps taken to design a superconducting solenoid that accommodates the unique requirement of a SRF gun cavity to have negligible magnetic field on the gun cavity wall material. The solenoid was tested and the operational results were compared to the expected performance of the solenoid design field with an acceptable agreement between the fields found. The solenoid will be used in a SRF gun test stand to add to experimental research for SRF gun cavities that can accommodate a higher RF gradient on the cathode.

To Carolyn Gee

Acknowledgments

I took a very winding path in graduate school and, as such, interacted with countless people who helped me while I was a graduate student some of which I will highlight here. To start, so many of my coworkers at SLAC helped foster engagement in the accelerator communities and are responsible for my original enthusiasm for particle accelerators. Lia Merminga, thanks for being the original mastermind of the SLAC/UCSC grad school idea and then to Bruce Dunham for enabling the opportunity to continue my grad school ambitions at SLAC. My Accelerator Operations coworker and managers were particularly supportive of my ambition to pursue graduate school while I worked as an accelerator operator and I am eternally grateful for their flexibility to accommodate my school requirements.

Outside of SLAC, the Cornell Center for Bright Beams, particularly Ivan Bazarov and Jarad Maxson, provided excellent technical guidance and really helped frame the big questions that needed answering in the simulation campaign. Thanks to the Ozaki exchange program for funding the invaluable fellowship opportunity to pursue graduate research in Japan. I hope to further the goal of increasing collaboration between American and Japanese scientists forward in my career. To the KEK staff who were truly excellent hosts and mentors to me, especially Konomi-san, Tsuchiya-san, Miyajima-san and Olga-san amongst countless others, thank you for sharing your kindness, time and expertise.

While this research work is not included in this dissertation, thank you to the UC National Lab In-residence Graduate Fellowship program for a year of graduate support to develop a Submerged Wireless Imaging Monitor (SWIM). Los Alamos National Lab's Rod McCrady and my own UCSC advisor Bruce Schumm provided excellent technical mentorship that produced plenty of transferable skills for my post-graduate school life.

Lastly, thank you to my advisor Bruce Schumm whose perseverance to convince me to finish this dissertation was applaudable. I am a better technical writer for all of your edits and I really appreciate the time you took helping me develop a technical writing skillset.

Outside of research, my fellow UCSC cohort really added positively to the graduate school experience. Classmates Carolyn Gee and Roy Sfadia provided a plethora of graduate school support, starting with group homework session and most recently including zoom thesis writing sessions from afar. To Carolyn specifically, the only other woman in our UCSC physics cohort, I really would not have finished this dissertation without your motivation to stick it out together.

Chapter 1

Introduction

1.1 Accelerators and Free Electron Lasers: An Overview

The majority of the 20th and 21st centuries have showcased the versatility and applicability of particle accelerator physics. At the most basic level, a particle accelerator is anything that accelerates beams of particles such as electrons, positrons and protons. The development of particle accelerators started as a tool to further scientific exploration to understand the fundamental building blocks of matter but, as we continue to develop accelerators, these machines have spun off into various aspects of society. The Department of Energy summarized the diverse use cases of accelerators in their 2010 report, Accelerators for America's Future:

> "A beam of the right particles with the right energy at the right intensity can shrink a tumor, produce cleaner energy, spot suspicious cargo, make a better radial tire, clean up dirty drinking water, map a protein, study a nuclear explosion, design a new drug, make a heat-resistant automotive cable, diagnose a disease, reduce nuclear waste, detect an art forgery, implant ions in a semiconductor, prospect for oil, date

> an archaeological find, package a Thanksgiving turkey or discover the secrets of the universe" [25]

Many of the applications above are possible because we can bend, wiggle or undulate a highly relativistic electron beam with alternating magnet poles in such a way that the electrons lose energy in the form of x-rays. Originally, the emitted light from a bending particle beam was considered a nuisance to high energy physics experiments and a problem that had to be mitigated. Slowly, scientists figured out that the high intensity x-ray byproducts can be used for imaging experiments. The short wavelength of x-ray light (relative to that of visible light) coupled with the high brightness generated from accelerators enables studies that probe structures on the molecular and atomic scales. These x-rays proved to be very scientifically valuable and the first accelerator to be used as a dedicated light source came online in the 1980s [3]. These particle storage rings, called synchrotrons, enable many of the imaging capabilities proclaimed in Accelerator's for America's Future statement, such as imaging a protein for a new drug.

The phenomenon of high energy electrons losing energy as useful x-rays photons have married the field of accelerator and photon sciences. To such end, accelerator scientists are constantly trying to push the envelope of the electron beam in order to generate higher energy and brighter photon beams. Synchrotron facilities originally only made use of bend magnets but researchers made a large step to increase the x-ray brightness by adding wiggling or undulator magnets to extract even more energy loss from the electron beam.

The next big leap forward in light sources came with the development of the Free Electron Lasers (FEL)[16]. FELs are driven by a linear accelerator, or linac, and have a much longer undulating magnet section where the electron beam and emitted light are allowed to co-propagate and interact with each other for many undulating cycles. At first, the electron beam gives and takes energy in equal mea-

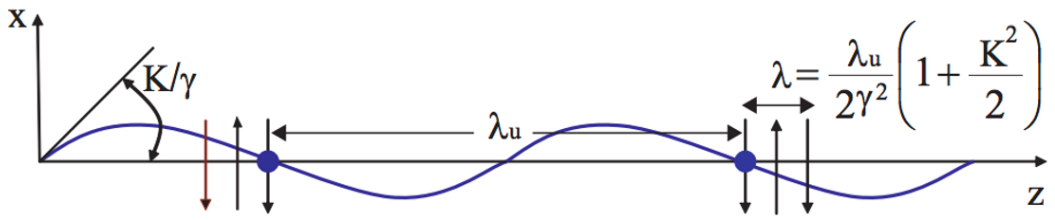

Figure 1.1: The trajectory of the electron beam as it travels through the undulator magnets and the pictorial descriptions of the magnet deflection parameter, K, the undulator period, λ_u. The wavelength of the resonant photons is centered around the distance the electron beam slips from the photon beam after an undulator period [13].

sure each time it overlaps with the light created by upstream electrons. However, an electron that gives energy to the light beam has less energy and will take a slightly longer path through the undulator magnets. In contrast, an electron that takes energy from the light beam will have more energy and take a slightly shorter path. After several cycles, the electron beam starts to form microbunches and creates a resonance condition with a characteristic wavelength that is dependent on the electron energy and on the periodicity and strength of the undulator magnets. The resonance wavelength is described pictorially in Figure 1.1 and given quantitatively by Eq. 1.1, where λ_u is the Undulator period, K is the undulator deflection parameter and γ is the Lorentz factor of the electrons [16]:

$$\lambda = \frac{\lambda_u}{2\gamma^2}\left(1 + \frac{K^2}{2}\right) \tag{1.1}$$

Once the electron beam is sufficiently microbunched, the rate of energy transfer from the electrons to the photon beam begins to dominate the energy transferred back into the electron beam causing exponential gain in photon production at a very specific wavelength.

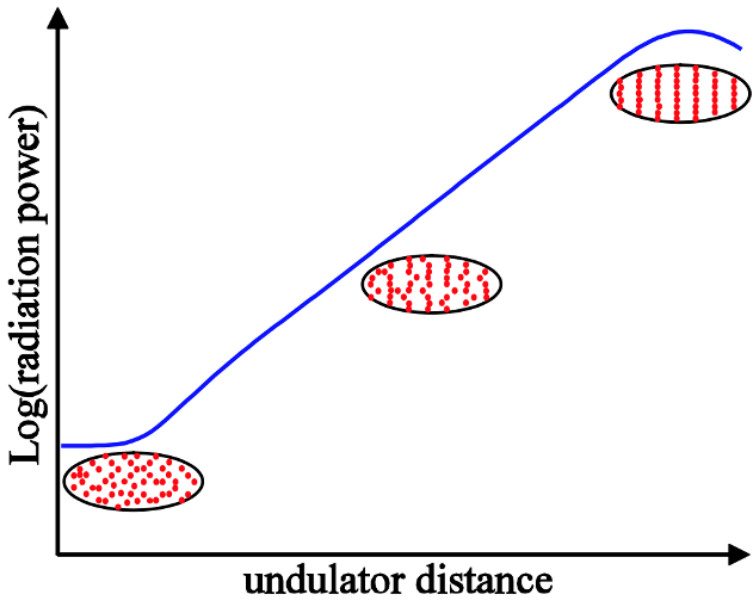

Figure 1.2: The blue line is the log of the expected radiated power as a function of electron beam location in the undulator magents. The ovals illustrate the state of microbunching in the electron beam at three locations in the undulator magnets [13].

Figure 1.2 illustrates the beam bunching at three spots along the undulator magnets. The result is a very short flash of x-rays with a laser-like, narrow wavelength spectrum that is many orders of magnitude brighter than light from a synchrotron. This process is called self-amplified spontaneous emission, or SASE, and is a second approach to achieve lasing, completely independent of the more common lasing method that stimulates emission between stable atomic states [16]. Figure 1.3 showcases the dramatic brightness improvements from the FEL process over a standard synchrotron.

FELs concentrate the light into a short flash on the order of femto-seconds (10^{-15} sec) and these short, bright pulses enable new applications that are not possible with a synchrotron. The microbiology community was one of the original scientific communities that pushed for x-ray FEL facilities in order to use FELs to image "live" viruses and bacteria that are not possible to be crystallized into a lattice. The coherent FEL light pulses can produce a sufficient Bragg interference pattern image for an amorphous target, relying on self-interference from a single scattering center rather than needing a periodic array of scattering centers (i.e, crystal) to form the Bragg pattern. In addition, the duration of the FEL pulse is short enough that the Bragg pattern is formed before there is sufficient time for the radiation damage from the intense x-ray pulse to cause significant damage.

FELs also enable imaging of fast dynamical processes as FELs can provide a flash of light on a time scale faster than that of the unfolding of the dynamical process itself. An example of such an application is the exploration of molecular dynamics - the process of formation or dissociation of molecular bonds. For example, researchers using an FEL to study chemical reactions pertinent to novel solar cells and memory storage found that "With each X-ray pulse lasting just 50 femtoseconds, the team could observe the electronic excitation by light and the

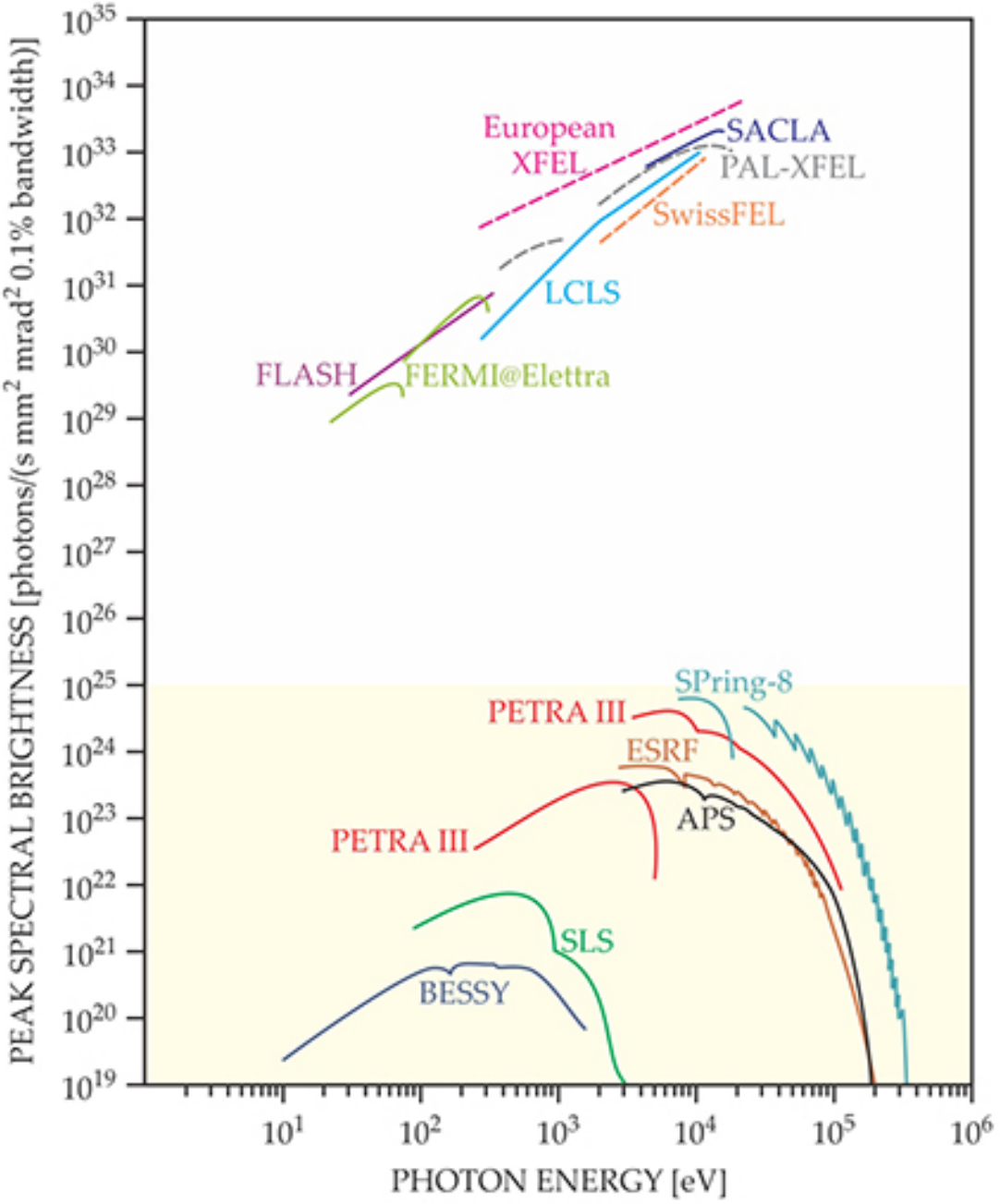

Figure 1.3: A brightness comparison between operating Synchrotrons and FELs. The machines in the yellow block are synchrotrons while the upper machines are FELs [6].

following breathing process at much shorter intervals than ever before and obtain a more complete picture in real time" [32].

Today, there are close to 10 x-ray FEL user facilities that are heavily in demand to run experiments. A downside of a FEL is that, while there are creative ways to share beam-time, an FEL can only be pointed to one user at a time. Additionally, a typical sample can only be imaged once as the high power x-rays typically destroy the sample.

As applications of FELs expands within the photon science community, experimenters find uses for FEL beams with every increasing repetition rate and intensity. FELs have sufficient demand from the FEL user community that there is a real scientific need to speed up the data collection process. Furthermore, there is a push to increase the photon energy in order to increase the resolution of imaging experiments and enable new science.

SLAC National Accelerator Lab, where the author of this dissertation worked for six years, has hosted the premier x-ray FEL of the early 2010's: the Linac Coherent Light Source (LCLS). The LCLS first came online in April 2009 and recently expanded its photon range to deliver 200 eV-25 keV photons [1]. However, the LCLS utilizes copper accelerating cavities that limit the machine to 120 Hz due to heat and power constraints.

To safely and efficiently increase the repetition rate to meet demand, future accelerators are being built using superconducting radio frequency (SRF) technology. These next-generation accelerator cavities are usually made from niobium instead of copper and are housed in cryogenic cavities filled with liquid helium. The niobium cavity is cooled until the material becomes superconducting. For reference, the LCLS-II cavities operate at 2 Kelvin [33]. The cavity is then filled with RF electromagnetic radiation to accelerate the electrons. While superconductive,

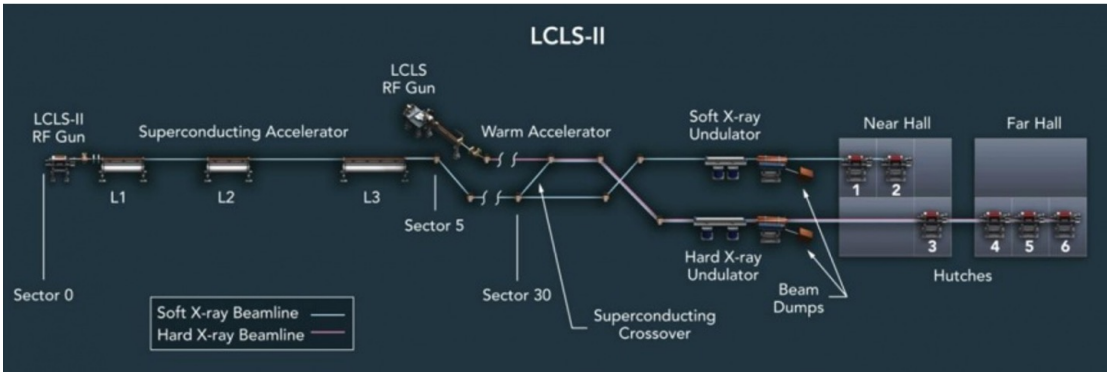

Figure 1.4: The facility overview for the LCLS-II project at SLAC [1]. The superconducting portion extends from the LCLS-II gun through L3.

the cavity material has no wall resistance when filled with RF, eliminating the main way RF energy is converted into unwanted heat.

SLAC is currently commissioning a MHz repetition rate FEL, the Linac Coherent Light Source II (LCLS-II), to follow up the success of the 120 Hz LCLS. LCLS-II has one kilometer of accelerating SRF cryomodules and 100 meters of undulator magnets. The SRF LCLS-II will accelerate electrons to 4 GeV (and then likely to 8 GeV in a proposed upgrade) and be able to deliver photons between 200 -5000 eV at the MHz repetition rate [33]. An LCLS and LCLS-II combined facility overview is shown in Figure 1.4.

The goal of this dissertation is to investigate improvements to the electron injector system, or first 10 meters of the electron accelerator structure, that will ultimately increase the photon production and increase the upper range of photon energies beyond 5 keV while accommodating this MHz rep rate.

1.2 Metrics of an Electron Beam

Generally speaking, the ultimate metrics of an FEL are the number of photons produced, the shortness of the photon pulse, and the compactness of the phase-

space volume occupied by the photons in the beam. So how do we optimize an electron beam to optimize these photon parameters? Since we will focus on the electron injector system in this dissertation, more specifically, how do we optimize an injector system that, in the case of LCLS-II, is an entire kilometer upstream of the undulator hall? The lasing process is dependent on the ability of the electron beam to microbunch as the electron beam and photon beams interact as they traverse through the undulator magnets. If the transverse electron beam size is very large or has a large transverse momentum spread, the beam quality is too poor to sufficiently microbunch and no exponential gain in photon production is possible.

Accelerator physicists have quantified the electron beam phase space of electron momentum versus position and defined this phase space area as the beam emittance. At the highest level definition, the emittance is the 6 dimensional phase space volume formed by the ensemble of the beam electron's x, x', y , y', z and z' values. x, y and z are the cartesian coordinates of each electron, with z being the beam direction. x', y' and z' are the momenta of each axis divided by the total momentum, such as $x' = \frac{p_x}{p_{total}}$.

Since it is often a good approximation to consider the beam behavior in three dimensions of space to be decoupled from one another, it can be convenient to consider the area of each of the three spatial coordinates separately, i.e, in terms of the trace space emittance, or the three two-dimensional projections, xx', yy', or zz'. Practically as well, experimentalists cannot measure a 6D phase space. Furthermore, we would like to be able to compare the emittance coming out of the injector system with emittance at various locations in the linac. According to Liouville's theorem, the local density in phase space must remain constant under conservative forces [8]. Applying this to the particle phase space of an

electron beam, the phase space will change shape but the phase space area, or the emittance, will remain the same under linear forces. Acceleration is not a linear force, so to get an invariant beam quality measurement that we can compare at various locations in an accelerator, we must normalize the emittance.

For the purposes in this dissertation, we will define the normalized RMS emittance mathematically for each respective trace space according to Eq. 1.5, where γ is the relativistic Lorentz factor, $\gamma = E_{total}/mc^2$, and $\beta = v/c$. Additionally we define the RMS beam size, angular divergence and correlation in Eq. 1.2, Eq. 1.3, and Eq. 1.4 respectively, with N_e the total number of electrons.

$$\text{RMS beam size: } \sigma_x^2(z) = \langle x^2 \rangle = \frac{1}{N_e} \sum_j x_j^2 \tag{1.2}$$

$$\text{RMS beam angular divergence: } \sigma_{x'}^2(z) = \langle x'^2 \rangle = \frac{1}{N_e} \sum_j x_j'^2 \tag{1.3}$$

$$\text{RMS beam correlation: } \langle xx' \rangle = \frac{1}{N_e} \sum_j x_j x_j' \tag{1.4}$$

$$\text{Normalized RMS Emittance: } \epsilon_x = \beta\gamma\sqrt{\langle x^2 \rangle \langle x'^2 \rangle - \langle xx' \rangle^2} \tag{1.5}$$

In the work that follows, we will make use of a simulation tool that sums up the emittance contributions of all the particles in the full beam and then sorts them in ascending order. We would like to focus on the high density core of the beam as our quality metric. Thus, for much of the simulation work that will be detailed in Chapter Two, we used the 95% RMS emittance value, or the emittance without including the 5% of particles that contribute most to the emittance calculation in Eq. 1.5, as the optimization parameter.

Another metric that impacts the ability of the beam to produce photons with

a narrow bandwidth is the energy spread of the beam, defined in Eq. 1.6.

$$\text{Energy Spread} = \sigma_E = \sqrt{\langle E^2 \rangle - \langle E \rangle^2} \tag{1.6}$$

In order to maximize the FEL gain at the undulators, the energy spread generally should be minimized by the time the beam gets to the undulator hall. For the beam coming out of the injector system, while we certainly care about minimizing the energy spread, the relationship of the electron energy versus electron longitudinal position in the electron bunch is important to consider as well. An energy versus z position dependance with a linear or second-order polynomial shape can be dealt with downstream of the injector. However, an energy spread with a higher order (HO) polynomial dependance to z position cannot be corrected for, and so is permanently in the beam. Therefore a metric we used for the simulation work was to quantify the amount of the Higher Order (HO) energy spread in the beam coming out of the injector system. To quantify the HO energy spread contribution, we found the second-order polynomial of best fit for the energy versus z position dependance, subtracted out the second-order polynomial of best fit, and then found the remaining RMS energy spread. Figure 1.5 demonstrates a menagerie of longitudinal phase spaces at the end of injector systems that showcase a range of energy versus z position dependance. These longitudinal phase spaces were seen during the simulation campaign to explore various injector designs, described in detail in Chapter Two.

Lastly, the longitudinal length, σ_z, of the beam out of the injector is important. At the entrance to the undulator hall, the length of the electron beam is approximately the same as the photon bunch that will be produced. Although the linac downstream from the injector can reduce or "compress" the longitudinal length of the beam coming out of the injector, there is still a maximum specification for

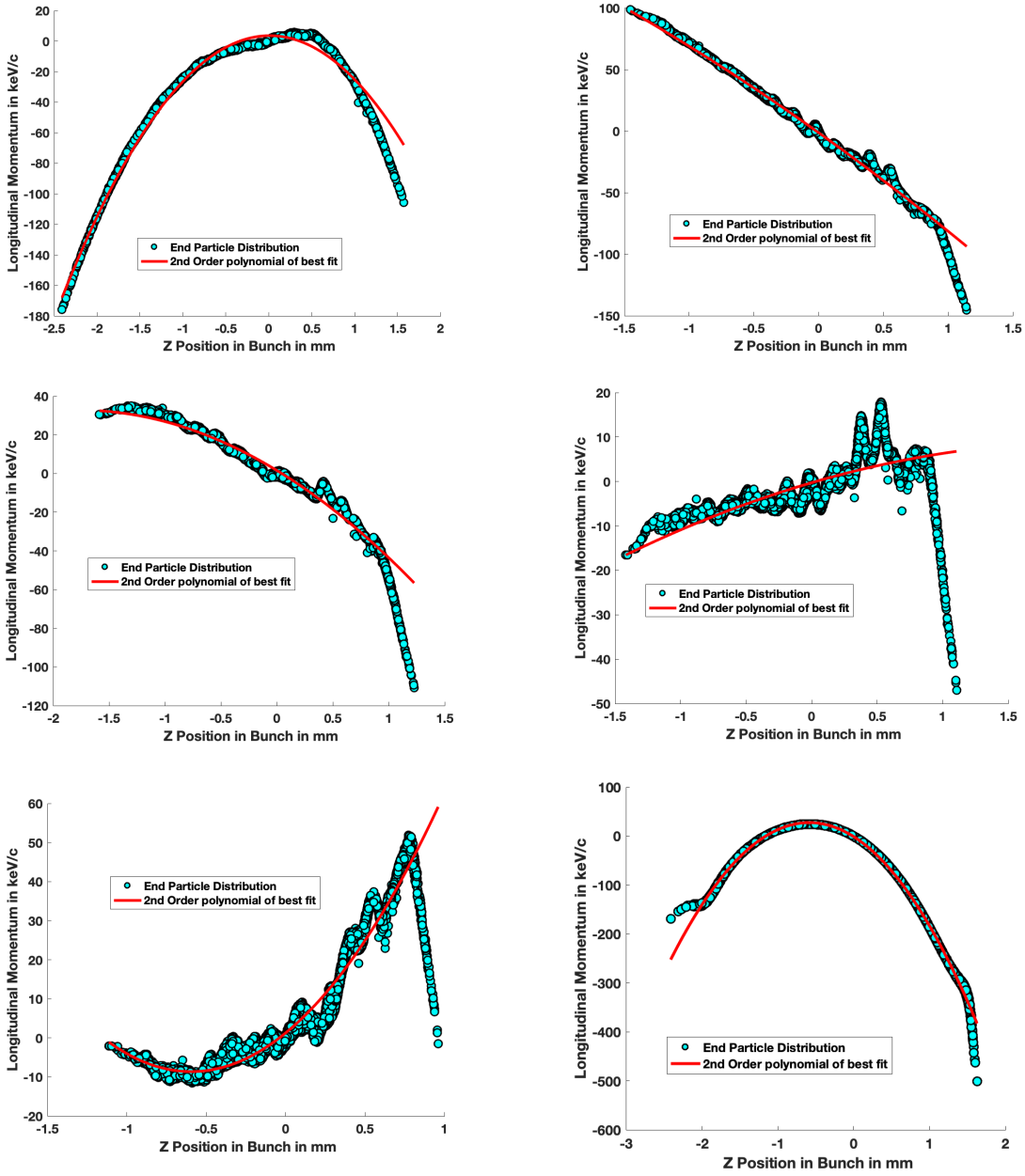

Figure 1.5: Various electron beam longitudinal phase space profile outputs at the end of a trial injector lattice from optimized ASTRA simulations detailed in Chapter Two. A second-order fitting polynomial (Red) is plotted with the raw particle output (Cyan). For the HO Energy spread metric, the Red polynomial of best fit would be subtracted from the Cyan raw data and then the remaining RMS energy spread would be found.

the σ_z at the exit of the injector. For the LCLS-II project, the injector needs to deliver around 3 picosecond, or 1 mm, long electron pulses so that the linac can sufficiently compress the electron beam to be around 10-100 femtoseconds at the undulator hall.

1.3 The Need for Injector Improvements

The LCLS-II project will initially run with a 4 GeV superconducting linac with a 200 eV to 5 keV photon range, but plans are already underway to upgrade the linac further in order to accelerate electrons to 8 GeV for LCLS-II HE (High Energy) and increase the maximum deliverable fundamental x-ray energy up to almost 15 keV[28].

Even after the upgrades to the LCLS-II facilities, FEL users would like a higher photon energy range from the LCLS-II complex. There are two ways to achieve this goal: higher energy electrons with more undulators, or more efficient lasing with the existing undulators. The LCLS-II project already has 100 meters of undulator magnets to stimulate the electron lasing process so space and cost is a limitation for the first option. Hence, research investigations for improving the photon energy range have focused on the latter option.

At higher electron energies, the x-ray energy range becomes throttled by emittance if the number of undulator magnets are not increased[28]. Lowering the beam emittance increases the efficiency of the interaction between the electrons and the co-propagating photons within the undulator magnets. Emittance directly determines how efficiently the electron beam microbunches as beam microbunching is required to start the exponential growth of x-ray production in wiggling undulator magnets[13]. 3D FEL theory is outside the scope of this dissertation but qualitatively, the electron beam size should be roughly less than the size of

the radiated photon beam, yielding the constraint in Eq. 1.7:

$$\sigma_x \lesssim \sqrt{\frac{\lambda}{4\pi} L_g} \tag{1.7}$$

L_g is the FEL power gain length and λ is the FEL resonant wavelength given by Eq. 1.1. However, for finite emittance, attempts to further reduce the beam spot size σ_x will result in an increased beam angular spread, introducing a corresponding spread in the resonant photon wavelength, which will still decreases the FEL efficiency. To not adversely effect the FEL gain, the electron beam angular divergence should be less than that of the emitted photon beam, yielding another constraint given by Eq. 1.8:

$$\sigma_{x'} \lesssim \sqrt{\frac{\lambda}{4\pi L_g}} \tag{1.8}$$

The limits on σ_x and $\sigma_{x'}$ taken together give an emittance threshold for a given x-ray wavelength λ, given by Eq. 1.9[13]. A beam emittance above this threshold will start to heavily hamper x-ray production.

$$\epsilon_{x,y} \lesssim \gamma \frac{\lambda}{4\pi} \tag{1.9}$$

Eq. 1.9 suggests that for the starting LCLS-II parameters of a 4 GeV electron beam and a desired 5 keV x-ray upper delivery, the transverse emittance should be below 0.15 mm mrad. LCLS-II currently expects a transverse emittance of 0.4 mm-mrad at the first undulator for a 100 pC electron beam. As shown in Figure 1.6, simulations predict that decreasing the normalized emittance at the undulators from 0.4 to 0.1 mm-mrad with an 8 GeV electron beam would increase the LCLS-II HE x-ray energy upper bound from 15 keV to 22 keV [28]. The benefit from lower emittance is even more drastic for FELs driven with higher electron

energies that desire even higher photon energies with a similar undulator hall.

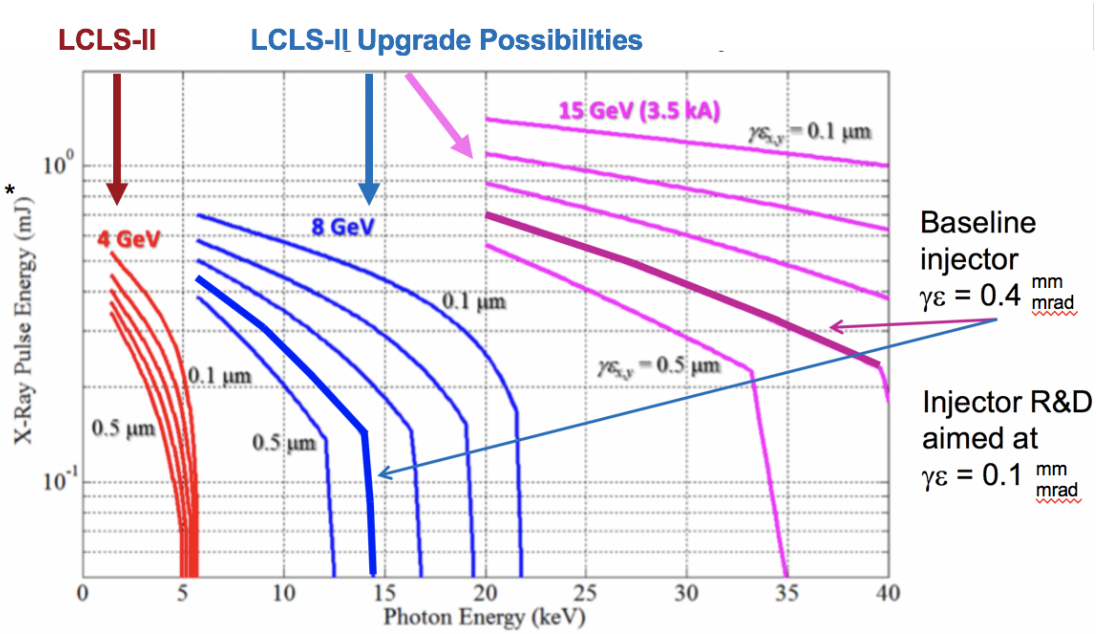

Figure 1.6: Expectations for how the emittance will effect the photon range for the LCLS-II and potential upgrades for various linac energies. The curves are predicted from the Ming Xie equations that numerically find the power gain length for x-ray generation [28].

Accelerator physicists have not yet discovered a way to deliver a 100 pC beam at 1 MHz with 0.1 mm mrad transverse normalized emittance. The quality of the electron beams produced in an accelerator facility is inherently limited by the emittance of the beam produced in the injector system. The current LCLS-II injector system simulations predict a 95% transverse emittance of 0.23 mm mrad out of the injector, indicating that injector improvements are necessary and the correct place to start looking to bring overall emittance down[2][34].

While this dissertation investigates injector improvements for FELs, with the specific goals of the LCLS-II HE project in mind, the general benefits of lower emittance in any accelerator are well documented elsewhere and would benefit a multitude of projects.

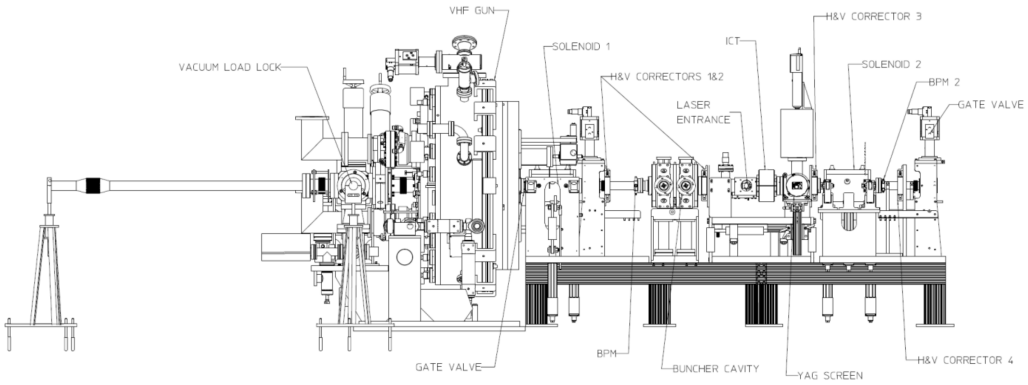

Figure 1.7: A schematic of the LCLS-II injector system. After the right most gate valve is the first accelerating cryomodule which is additionally included in the definition of the injector system for this dissertation [14].

1.4 The Injector System: Components and their Expected Emittance Contributions

The emittance coming out of the injector system cannot be decreased later on in the linac so emittance improvements from the injector are required if the LCLS-II HE project is going to meet a 0.1 mm mrad transverse 95% emittance specification at the undulator hall. This next section will describe what makes up the injector system and the expected emittance contributions of each components to motivate areas for emittance reduction.

This dissertation will define the injector system as the system that frees the electrons from some sort of material, called the cathode, and accelerates the electrons to about 100 MeV. 100 MeV is selected as a good boundary to an injector system as 100 MeV is where space charge effects can largely be ignored as the electrons are sufficiently relativistic. We will use the LCLS-II injector, shown in Figure 1.7, as a baseline for introducing an electron injector system, but generally the components are relatively similar across injector systems.

The beam is freed from a cathode with an intrinsic, or thermal, emittance. The

beam emittance will grow as it goes through the injector lattice and the emittance contributions from lattice components add to the original thermal emittance in quadrature. We will explore the individual emittance growth contributions of common injector components in the forthcoming sections.

It is necessary to note that the back (or tail) and front (or head) of the beam are not necessary aligned in x, x' phase space. The projected, or full beam, transverse emittance can look deceptively large, or oscillate in value when measured at certain areas of the injector lattice when, in reality, this is just the misalignment of phase space temporal slices and the emittance of a thin slice of the beam is still sufficiently small. The alignment of beam slices in phase space is called emittance compensation and is crucial to minimizing the projected transverse emittance in order to minimize the space charge emittance growth in accelerating sections [8]. A pictorial description of emittance compensation is shown in Figure 1.8.

1.4.1 The Cathode and Laser

The first job of the injector system is to free electrons from a cathode. Current state of the art is to use the photoelectric effect to free electrons from a metal or semiconductor cathode material. The cathode material that is best suited for a photoinjector system is highly dependent on the desired electron current and repetition rate. At a relatively low rep rate, the original LCLS uses a standard copper puck with a UV laser to excite electrons for each bunch. A copper cathode has a low quantum efficiency of $4e10^{-5}$ per 4.86 eV photon, where quantum efficiency is defined as number of electrons emitted per number of photons. For the MHz LCLS-II project, using a copper cathode would necessitate an unfeasibly high power UV laser. Therefore the LCLS-II project is using a cesium telluride, semiconductor cathode, Cs_2Te, that will have a quantum efficiency of $9.2e10^{-2}$

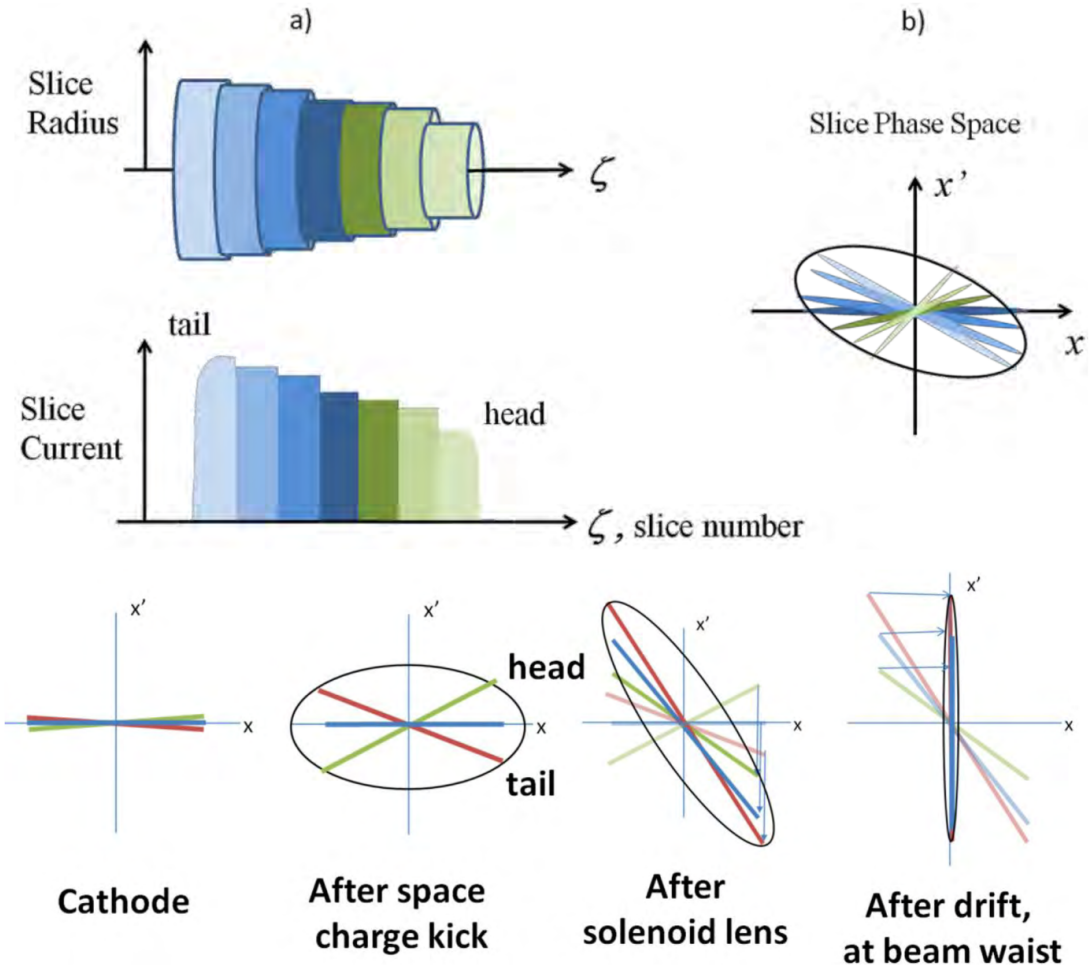

Figure 1.8: A pictorial description of emittance compensation, courtesy of the Engineering Guide to Photoinjectors [27]. The top images show how the beam is split into different temporal slices. The slices can have varying RMS transverse sizes or current magnitude. Each slice can have a small emittance but if the slices are not aligned in phase spaces, the total beam projected emittance can appear significantly larger, as shown in the upper right image. The bottom series of images shows an example of how the slice and resulting projected emittance change as it goes through a beam lattice.

per 4.66 eV photon[33].

Ideally we free the electrons with no excess energy or energy spread but, in practice, there will always be a kinetic energy distribution of the electrons freed from the cathode material that results in a transverse momentum component. This causes an initial emittance spread off of the cathode, called the thermal or intrinsic emittance, given by Eq. 1.10:

$$\epsilon_x^{th} = \sigma_x \sqrt{\frac{\hbar\omega - \phi_{eff}}{3mc^2}} \tag{1.10}$$

ϕ_{eff} is defined as $\phi_w - \phi_{schottky}$ where ϕ_w is the material work function (4.85eV for copper for example) and $\phi_{schottky}$ is the Schottky work function, or the amount of work the RF field does on the cathode surface.

To minimize the thermal emittance off the cathode, it is desirable to use a wavelength as close to the work function of the cathode material. However, the laser wavelength has to be sufficiently above the material work function to have a quantum efficiency high enough to get the required bunch charge with reasonable laser power. The thermal emittance is linearly dependent on the laser spot size that generates the initial transverse rms spot size of the electron beam so smaller initial spot sizes will result in a decreased thermal emittance.

1.4.2 The Gun Cavity

The cathode is placed in an initial cavity (or cavities) that is filled with RF, called the gun cavity, that will take the newly freed electrons and give the initial beam acceleration. For the original LCLS project, the gun is a 1.5 cell copper cavity that is pulsed with 2856 MHz RF and runs with an acceleration gradient around 115 MV/m.

Due to the properties of Maxwell's equations in a source-free region of space,

the entrance and exit of an RF cavity act as a focusing and defocusing lens that balance each other for a normal accelerating cavity. However, the beam originates in the gun cavity resulting in the exit of the RF cavity acting as a defocusing lens for the electron beam, the focal length given in Eq. 1.11 [27]:

$$f_{RF} = \frac{-2\beta\gamma mc^2}{eE_0 \sin(\phi_0)} \tag{1.11}$$

where γ is the Lorentz factor of the electrons at the end of the gun cavity, E_0 is the peak RF field and ϕ_0 is the phase of the electron bunch with respect to the peak electric field. The strong defocusing of the gun cavity necessitates a strong focusing lens, usually a solenoid, to capture the beam. The properties of the solenoid will be described in a forthcoming section.

As the RF fields are time dependent, the RF fields introduce both a transverse and longitudinal emittance contribution, approximated for a gaussian beam in Eq. 1.12 and Eq. 1.13 respectively [8]:

$$\epsilon_x^{rf} = \frac{k^3\alpha}{\sqrt{2}}\sigma_x^2\sigma_z^2 \tag{1.12}$$

$$\epsilon_z^{rf} = \sqrt{3}(\gamma - 1)k^2\sigma_z^3 \tag{1.13}$$

where $\alpha = \frac{eE_0}{2mc^2k}$, where E_0 is the peak RF field, $k = \frac{2\pi\nu_{rf}}{c}$, and ν_{rf} is the RF frequency. γ is the final average γ, or Lorentz factor, of the electron at the gun cavity exit.

The transverse RF emittance contribution grows proportionally to $\sigma_x^2\sigma_z^2$ motivating that the beam transverse spot size and longitudinal length should be kept small to minimize this emittance contribution. Additionally, the emittance increases with both increasing frequency and accelerating gradient.

1.4.3 Space Charge Emittance Contributions

The injector system requires care to address emittance growth due to space charge effects. Throughout the entire injector lattice, the coulomb repulsion that the electrons feel from the other electrons in the beam before the beam is sufficiently relativistic causes nonlinear, time-dependent, space charge forces that increase the emittance. The specific relation of space charge-induced emittance growth is dependent on the shape of the beam and is non-trivial to calculate. For a drift section, the space charge emittance growth is approximated by Eq. 1.14 [7]:

$$\epsilon_x^{sc} = \frac{qIz}{16\pi\epsilon_o m_o c^3 \gamma^2 \beta^2} G(\gamma\sigma_z/\sigma_x) \tag{1.14}$$

where I is the beam peak current, z is the drift distance, and G is a geometric factor that depends on the beams aspect ratio in the reference frame of the beam.

Eq. 1.14 shows the inverse scaling with beam energy, motivating the case to accelerate the beam as quickly as possible. To better showcase the dependance on the beam size dimensions, Kwang-Je Kim integrated Eq. 1.14 specifically for the photoinjector gun cavity [7]. The instantaneous RF emittance growth described in Eq. 1.12 depends on the square of the rms beam size. Thus the additional radial expansion from space charge repulsions additionally adds to the RF emittance growth, coupling the RF and space charge emittance growth in the gun cavity. Kim determined that for a gaussian beam coming out of an RF gun cavity, the space charge induced emittance at the end of the cavity is approximated by Eq. 1.15 for the transverse emittance and Eq. 1.16 for the longitudinal emittance [8][27]:

$$\epsilon_x^{sc} \approx \frac{c}{8\alpha\nu_{rf}} \frac{I}{I_A} \frac{\sigma_z}{3\sigma_x + 5\sigma_z} \tag{1.15}$$

$$\epsilon_z^{sc} \approx \frac{c}{8\alpha\nu_{rf}} \frac{I}{I_A} \left(\frac{1.1}{1 + 4.5\frac{\sigma_x}{\sigma_z} + 2.9\left(\frac{\sigma_x}{\sigma_z}\right)^2} \right) \tag{1.16}$$

where I_A is the characteristic, or Alfven, current which is $\approx 1.7e10^4\beta\gamma$ for electrons [29]. $\alpha = \frac{qE_0}{2mc^2k}$ where E_0 is the peak RF field, ν_{rf} is the RF frequency and $k = \frac{2\pi\nu_{rf}}{c}$. I is the peak current of the beam at the beam center.

As the electrons gain energy, the added space charge emittance growth scales inversely with γ. For an electron with 100 MeV kinetic energy, $\gamma \approx 200$ and added emittance growth from space charge effects becomes negligible for the beam currents most commons with accelerators that drive FELs.

When the beam comes off the cathode, the space charge forces give varying kicks to the head and tail of the beam depending on the beam current. This space charge kick is shown in Figure 1.8. This phase space misalignment causes an increase in the projected emittance that needs to get corrected down stream, usually done by the solenoid.

1.4.4 The Solenoid

The solenoid plays dual roles in the injector lattice. Firstly, the solenoid is necessary to capture the electrons that are initially defocused coming out of the RF gun. Secondly, the solenoid helps performs emittance compensation to align the phase space slices in the beam to lower the projected beam emittance.

As the beam comes off the cathode, space charge forces gives different kicks to the head and tail of the beam, misaligning the phase space slices of the beam and increasing the projected emittance. When the beam goes through the solenoid,

the solenoid provides an angular kick to the head, middle and tail of the bunch. This angular kick is derived and defined in Appendix A. This angular kick from the solenoid gives the same sign for the divergence for all parts of the bunch which, when followed by a drift section, will cause the phase space slices to align at a beam waist. This process is shown in the bottom part of Figure 1.8. While hidden from view in Chapter Two, the maximum fields of the solenoids in the trial injector lattices are chosen to optimally perform emittance compensation. The simulation work in Chapter Two optimizes the total beam transverse emittance at the end point of the injector which is only at a minimum when the phase space slices are aligned.

The solenoid is also needed to counter the defocusing effects for the RF gun cavity and derivation of the solenoid focal length for an electron beam is done in detail in Appendix A. To summarize from there, the expected focal length of the solenoid, f_{sol} is given by Eq. 1.17.

$$f_{sol} = \frac{v_z^2 4m^2\gamma^2}{q^2 \int B^2 dz} \tag{1.17}$$

where v_z is the average longitudinal velocity of the electron beam going through the solenoid and $\int B^2 dz$ is the integral of the square of the magnetic field magnitude on the center beam axis.

The solenoid introduces emittance that results from an energy spread in the beam, called the chromatic emittance. The solenoid chromatic emittance arises from the different focal length electrons of different energy will have. In the thin lens approximation, the solenoid chromatic emittance growth scales as Eq. 1.18. $k_{sol} = \frac{eB_{sol}}{2\gamma mc}$ and l_{sol} is the effective length of the solenoid. σ_γ is the induced energy spread of the electron beam is defined as $\sigma_\gamma = \sqrt{<\gamma^2>}$.

$$\epsilon_{ch} = \sigma_\gamma k_{sol}^2 l_{sol} \sigma_x^2 \tag{1.18}$$

The solenoid also contributes emittance growth from geometric aberrations. Solenoid magnetics exhibit third-order aberrations that can be calculated for a known axial field using an off axis field perturbations. Determining the off-axis fields is done in detail in Appendix B. However, the aberrations from non-linear off-axis fields don't perfectly predict the expected emittance growth, and the current way to calculate the geometric aberration emittance growth is to do so numerically in order to take into account beam dynamic effects. An example of this is done in Chapter Three.

1.4.5 The Buncher Cavity

Beams out of the RF gun can be relatively long to minimize space charge repulsion effects on the cathode that degrade beam quality. Therefore, it is common to have a buncher cavity after the gun that is run off-crest, or a phase difference away from peak acceleration, to compress the bunch coming out of the RF gun cavity. In a pure buncher cavity, the RF cavity is timed to run 90 degrees off crest in a direction such that energy is taken away from the head of the bunch and added to the tail. Since the electron beam out of the gun cavity is not fully relativistic yet, the tail speeds up while the head slows down, compressing the length of the beam. We will look at various gun cavities that deliver a wide range of electron beams out of the gun cavity, $\approx$ 400 keV to 2 MeV, later on in this dissertation. At the higher end of this range, a buncher is not strictly always needed. For the simulation work detailed in the upcoming chapters, we included a cavity after the gun cavity in our trial layouts that could act like a buncher if needed but could also, especially for the higher energy, purely accelerate the beam ($\phi = 0$ deg) or

run at a phase that acted as hybrid bunching and accelerating cavity (such as $\phi = -45$ deg).

Since the beam enters and exits the buncher cavity, there is no net focusing or defocusing effect that needs to be dealt with. The emittance growth from the buncher cavity is similar to that of the gun cavity emittance contributions detailed in Eq. 1.12 and Eq. 1.13.

1.4.6 Emittance Contribution Summation

The sections above detail the emittance growth expected as the beam goes through the injector lattice. In general, the total emittance growth out of various lattice elements add in quadrature, as given by Eq. 1.19 for the transverse emittance:

$$\epsilon_x = \sqrt{\epsilon_{th}^2 + \epsilon_{rf}^2 + \epsilon_{sc}^2 + \epsilon_{sol}^2} \tag{1.19}$$

This emittance growth happens locally and if we are able to just look at a slice of the phase space, we would see the emittance growth effects described in the sections above. However, accelerator physicists cannot easily measure emittance for a temporal subset of the beam, and if left uncorrected during acceleration, the misaligned phase spaces will ultimately increase the slice and overall emittance. Therefore, it is imperative to manage the emittance compensation as part of the optimization for any injector system.

The components of an injector lattice described above would select for competing beam attributes if we optimized the emittance contribution of a component in isolation. For example, to minimize emittance growth from the time dependent RF field, we would like the length of the beam to be as short as possible. But if the beam is short, then the space charge emittance growth increases. If we expand

the transverse spot size of the beam, we can mitigate the space charge effects but then the thermal emittance off the cathode increases. On top of that, we have additional beam parameters that we care about, such as longitudinal length, beam energy and energy spread. To maximally reduce the emittance out of an injector system is a complicated, multi-parameter optimization challenge. To foreshadow how this dissertation will optimize an injector lattice, Chapter Two will present an optimization method that couples a particle tracking simulation tool with a genetic algorithm.

1.5 Injector Improvement Ideas

Currently, injector physicists have identified two areas of improvement for research to decrease the emittance out of an injector system: increasing the acceleration gradient in the gun cavity and looking at new cathode materials. Cathode researchers are looking to improve the beam thermal, or intrinsic, emittance from the cathode while still delivering the desired charge specifications with reasonable laser powers. Gun physicists are researching methods to raise the gun gradient on the cathode to mitigate space charge emittance contributions while still satisfying the repetition rate requirements of the larger accelerator.

1.5.1 Current Cathode Options

Finding new, improved cathode material is a complicated endeavor that would motivate a standalone dissertation for that research alone. Cathodes need to optimize the thermal emittance against the cathode lifetime, laser power requirements and deliverable charge, amongst other parameters. This dissertation will not dive into cathode physics. Instead, this dissertation will treat the cathodes as an ide-

alized source of electrons into the gun cavity, and will simplify cathodes down to various thermal emittance per beam rms spot size.

Currently the semi-conductor, cesium telluride cathodes for the LCLS-II project are estimated to produce a beam with a thermal emittance of ≈ 1 mm mrad / σ_x. In this dissertation, I looked at the impacts of various cathode thermal emittances on the final emittance at the end of the injector lattice without specifying the specific material. Many of the thermal emittances used are not possible yet but the goal of the simulation campaign in Chapter Two is to show, if cathode physicists *could* produce a cathode that produced the simulated thermal emittance, what improvements to the final beam emittance could be expected after the various degrading effects associated with the remainder of the injector system.

1.5.2 Current Photoinjector Options

Currently there are three types of injectors that are being developed to drive these high rep rate experiments: Direct Current (DC), Normal Conducting RF (NCRF), and Superconducting RF (SRF) guns.

DC guns operate with constant high voltage on the cathode and naturally meet the high repetition rate requirement. Generally, for high current accelerators, DC guns are the necessary choice. DC guns have reliably operated for many years at several labs. However, DC guns are limited by high voltage breakdown and therefore have a relatively low gradient at the cathode. Currently, a state of the art DC electron gun can deliver a 7 MV/m acceleration gradient on the cathode and can deliver around 500 keV electrons [19]. This limits the beam quality that a DC gun can deliver at the higher bunch charges (as higher bunch charge brings higher space charge emittance contributions) that are needed for an FEL.

The 120 Hz, Normal conducting LCLS utilizes an 2856 MHz NCRF gun to

provide up to 1 nC bunches and has successfully and reliably delivered a high quality electron beam for over 10 years. Because the RF is pulsed with a 0.05 % duty cycle, the LCLS NCRF gun can provide a gradient of 115 MV/m and still dissipate the heat generated by eddy currents in the RF structure. To operate in the MHz repetition rate or higher reg, pulsed RF is no longer an option and gun cavities must operate in a continuous wave, or CW, mode. If we changed the LCLS NCRF gun to CW, we would expect the gun to go from dissipating 4 kW on average to about 8 MW [10]. For reference, 8 MW is about 70% of the power needed to operate a Eurostar 20-carriage train, and in a NCRF gun the vast majority dissipates as heat. This amount of power is a nonstarter for a NCRF gun cavity.

For the LCLS-II project, DC, NCRF and SRF guns were looked at and evaluated based on the project specifications, beam quality and reliability. Ultimately the project chose to go with the Advanced Photoinjector Experiment (APEX) gun developed at Lawrence Berkeley National Lab (LBNL). The APEX gun is a NCRF gun but with significant differences to the original 120 Hz LCLS gun. The APEX gun operates at a much lower RF frequency, 187.5 MHz, which enlarges the cavity significantly and reduces heat loss in the walls. It also has a much lower maximum electric field at 20 MV/m. The APEX gun is expected to use 100 kW of power when fully operational [33].

SRF guns attempt to solve the heating bottleneck discussed above for NCRF guns. When the the cavity material is superconducting, there is no resistance in the cavity walls to turn the RF into heat. Therefore the RF power cost is negligible and the main power consideration comes from the cryoplant that is necessary to provide liquid helium. The SRF gradient is therefore not limited by power but instead by the fact that higher gradients enables more dark current

(current accelerated that is not emitted from the cathode) and the ultra clean requirements that, when not done with the utmost care, will cause small regions of the cavity material to quench. There are currently only two SRF guns used in beam facilities: The SRF Gun II at the Helmholtz-Zentrum Dresden-Rossendorf (HZDR) and the Quarter Wave Resonator at Brookhaven National Lab (BNL). Consequently, while SRF guns have the potential to get higher gradients upwards of 50-60 MV/m on the cathode in CW operation, the technology is currently not reliable enough to consistently demonstrate the SRF advantages.

SRF guns are currently under-researched but have promise of contributing to high rep rate FEL projects if the reliability challenges can be addressed. This dissertation aims to contribute to the development of SRF guns both through simulations and experimental SRF work to improve gun cavity performance. The simulation campaign in Chapter Two aims to show if injector physicist *could* improve the reliability of SRF guns, what improvements to the final beam emittance could be expected. The work in Chapter Three designs a superconducting solenoid magnet to go with a test stand for a new SRF gun cavity to contribute to the SRF experimental effort.

1.5.3 Injector Improvement Investigation in this Dissertation

In this dissertation, I will investigate both gun cavity and cathode upgrade options through simulation with the goal to demonstrate how much emittance reduction is expected for each upgrade option. SRF gun cavities have the most potential to meet the high rep rate demands while delivering the highest quality beam. Therefore two SRF cavity candidates are compared to the current LCLS-II gun, the APEX gun, in the simulation work. Lastly in Chapter Three, I will focus

on SRF gun cavities and detail contributions to building the solenoid component for a test stand injector to test a new SRF gun cavity design.

Chapter 2

Injector Optimization Simulations

2.1 Introduction

Building an electron photoinjector system is incredibly costly so the work presented in this chapter describes an injector improvement study through a simulation campaign. This dissertation work focuses specifically on improvements for a continuous wave (CW) injector system that could be capable of driving an experiment like the Linac Coherent Light Source II (LCLS-II) at SLAC National Accelerator Laboratory. The major nominal requirements for the electron beam out of the LCLS-II injector system are provided in Table 2.1 for reference.

The current LCLS-II injector lattice had been designed and optimized prior to this dissertation work by researchers predominantly at SLAC, Cornell and Lawrence Berkeley National Laboratory (LBNL)[2]. The injector system layout as presented in the LCLS-II final design report is shown in Figure 2.1. The prior simulation work for the LCLS-II injector serves as the baseline result that results from the simulation campaign described in this chapter will be compared to.

The highest level goal for this simulation campaign is to improve upon the performance of the existing LCLS-II injector system by identifying ways to decrease

Parameter	Nominal Requirement
Energy at gun exit	750 keV
Electron energy	$\approx$ 100 MeV
Bunch repetition rate	0.62 MHz
Bunch charge	100 pC
Bunch length RMS	1 mm
Slice emittance	0.4 mm mrad
Cathode Thermal Emittance	$<$ 1 mm-mrad/mm

Table 2.1: The major LCLS-II requirements for the Injector Beam [33].

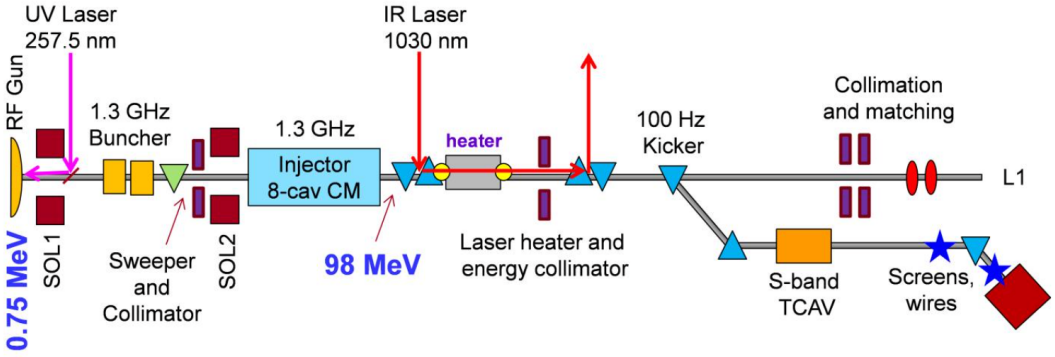

Figure 2.1: A cartoon portrayal of the entire LCLS-II injector system [33].

the emittance out of the injector system to improve the wavelength range and brightness of the photon beam generated from the FEL process. To accomplish the desired emittance reduction, the high rep rate photoinjector community is currently pursuing quality improvements in two main areas: Improving the thermal emittance of the electron beam off of the cathode and increasing the electric field gradient in the gun cavity to better mitigate space charge emittance growth.

The original LCLS-II simulations assumed a cathode material that produced a thermal emittance of 1 mm mrad/mm (rms) in the emitted electron beam. The LCLS-II project will initially utilize cesium telluride cathodes that have experimentally demonstrated thermal emittance measurements around 0.75 mm mrad/mm [33]. Other materials have promise to produce beams with a lower thermal emittance but are currently limited by either lifetime, quantum efficiency or vacuum requirement shortcomings. In this chapter, we will document the emittance gains the accelerator community could expect as a function of the degree of improvements of the cathode thermal emittance. Additionally, we will provide an estimate of the thermal emittance required from a cathode needed to achieve 95% envelope 0.1 mm mrad emittance out of an injector system similar to the LCLS-II injector lattice for three difference gun cavity designs that satisfies the LCLS-II injector design requirements in Table 2.1.

The current LCLS-II Normal Conducting RF (NCRF) gun is a duplicate of the Advanced Photoinjector Experiment (APEX) designed and commissioned at LBNL [31]. The APEX gun cavity is shown in Figure 2.2. The APEX gun is currently limited to a maximum gradient of 20 MV/m due to power and heating constraints. SRF electron guns are an appealing prospect to use as a future LCLS-II gun cavity as SRF guns have the potential to reliably operate at higher gradients for high repetition machines which would help limit the emittance growth due

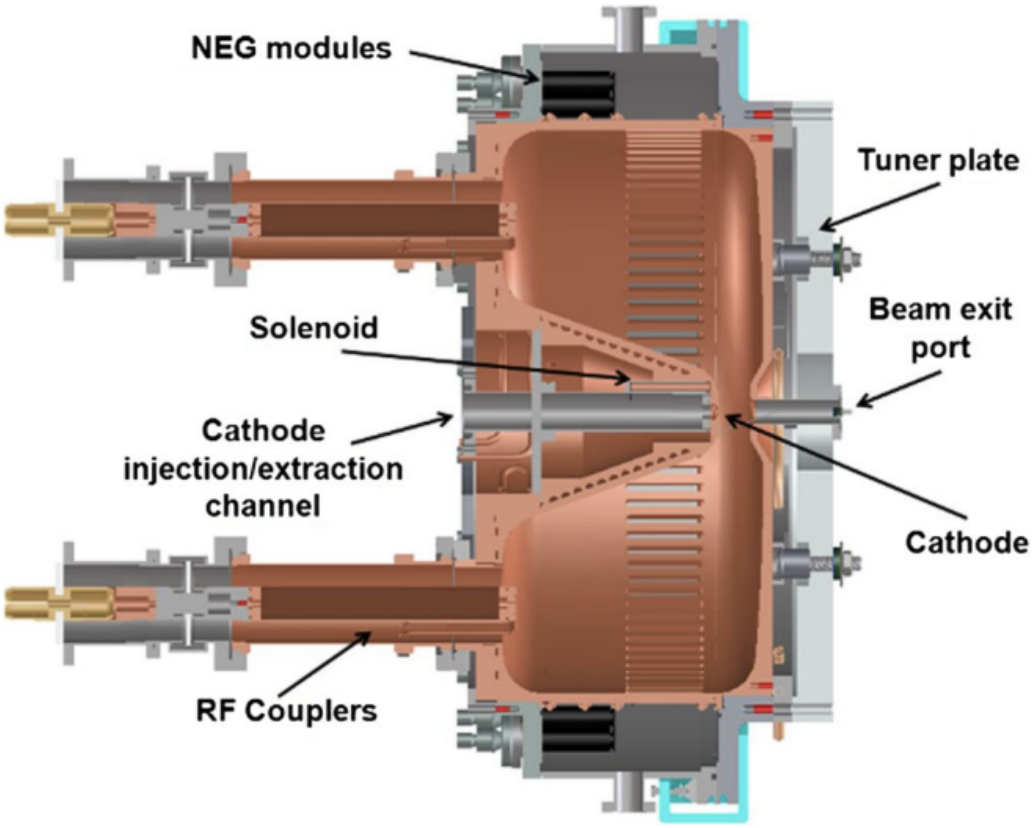

Figure 2.2: The APEX gun cavity design that is used as the current LCLS-II gun cavity. The gun cavity is NCRF and will run with a maximum gradient of 20 MV/m [30].

to space charge. Currently, standard SRF accelerating cavities can produce a maximum electric field above 65 MV/m, though SRF gun cavities need substantial development to reach these same specifications [20]. This chapter will document how cathode improvements, with no other changes to the current LCLS-II injector, will improve the final injector transverse emittance. Additionally, we will also explore the potential emittance benefits of two proposed superconducting RF (SRF) cavity designs that would allow significantly higher gun cavity gradients.

In this chapter, we aspire to decouple gun cavity upgrades from cathode quality upgrades through a systematic simulation study. The ultimate objective here is to motivate where more research and development is needed and provide guidance for experimental studies on how to prioritize the research effort of the photoinjector community to best meet the needs of the larger accelerator community. To decouple the cathode performance from cavity improvements, we start each gun cavity upgrade idea with a perfect cathode. This dissertation will define perfection as an initial beam with no transverse or longitudinal momentum, i.e 0 mm mrad/ mm (rms) thermal emittance off of the cathode. We evaluate the theoretical performance for each injector lattice with three different gun cavity designs with an idealized perfect cathode in order to isolate the theoretical minimum emittance contributions of injector lattices driven by the three investigated gun cavities, two of which operate at substantially higher gun cavity gradient. We then increase the cathode thermal emittance in 0.2 mm mrad / mm (rms) step sizes until the cathode emittance reaches the conservative estimate of the current LCLC-II cathode, 1 mm mrad/ mm, to illustrate each injector's sensitivity to the cathode emittance. Through this campaign, we present a study in a manner that uncouples the expected emittance improvements from moving to an SRF gun cavity design versus improvements to the beam quality off of the cathode.

2.2 Gun Improvement Candidates

There is a long lead time to develop and test a new electron gun so, for this simulation campaign, we investigated SRF gun cavities already at various stages of development. The anticipated electric field files for the gun cavities were simulated prior to the start of the study detailed here.

2.2.1 SRF Quarter Cell Gun Cavity: the WiFEL Gun

University of Wisconsin-Madison developed and commissioned a 200 MHz quarter cell SRF gun cavity that will be referred to here as the Wisconsin Free Electron Laser, or WiFEL, gun. The WiFEL gun was specifically designed to drive a high rep rate FEL such as the LCLS-II project [5]. The cavity was designed to have a gradient around 50 MV/m with an original experimental goal of 40 MV/m. The University of Wisconsin-Madison team commissioned the WiFEL gun cavity in 2013. A layout of the gun cavity in the commissioning cryostat is shown in Figure 2.3. The team measured a maximum cavity gradient of 35 MV/m when the cavity was pulsed without the cathode, that deteriorated to 20 MV/m when the cathode was inserted in CW mode. The commissioning team recommended more RF cavity conditioning to better clean the cavity as a means to increase gradient performance but further measurements were not possible before commissioning activities concluded [5].

For the simulation campaign, we simulated the WiFEL gun cavity with a maximum gradient up to 50 MV/m to estimate the expected performance of the WiFEL gun if the gun could be operated at design potential.

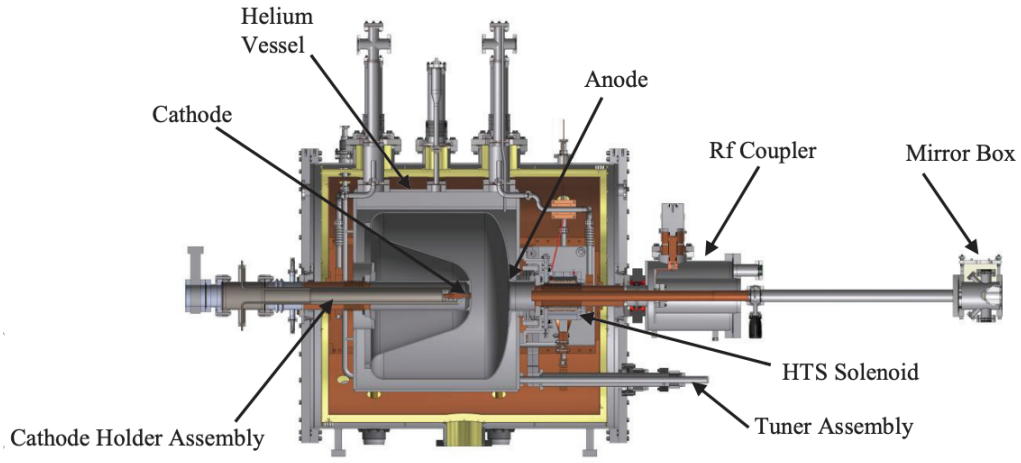

Figure 2.3: A schematic of the WiFEL gun cavity in the commissioning cryostat. The cryostat houses a liquid helium vessel, the cathode and the high temperature superconducting (HTS) solenoid [20].

2.2.2 SRF 1.5 Cell Gun Cavity: the KEK Gun

The High Energy Accelerator Research Organization in Tsukuba Japan, known as KEK, is developing a 1.3 GHz, 1.5 cell SRF gun cavity that will henceforth be known here as the KEK gun [18]. The KEK gun was designed to drive a CW energy recovery linac (ERL) but presented a ready opportunity to ascertain the potential advantages of a higher gradient gun with a higher RF frequency and multiple RF cells for an FEL application, as both the APEX and WiFEL guns are quarter cell cavities. An RF cavity is a vessel driven by an RF source with the KEK gun comprised of 1.5 coupled cells. One cell is designed to resonate with a half wavelength standing wave at the design RF frequency (1.3 GHz for the KEK gun).

The KEK SRF group has fabricated multiple KEK gun cavities and performed gradient performance tests without generating an electron beam. The KEK gun design is shown in Figure 2.4. The preliminary gradient tests have been extremely promising, albeit inconsistent and highly dependent on the integrity of the cavity

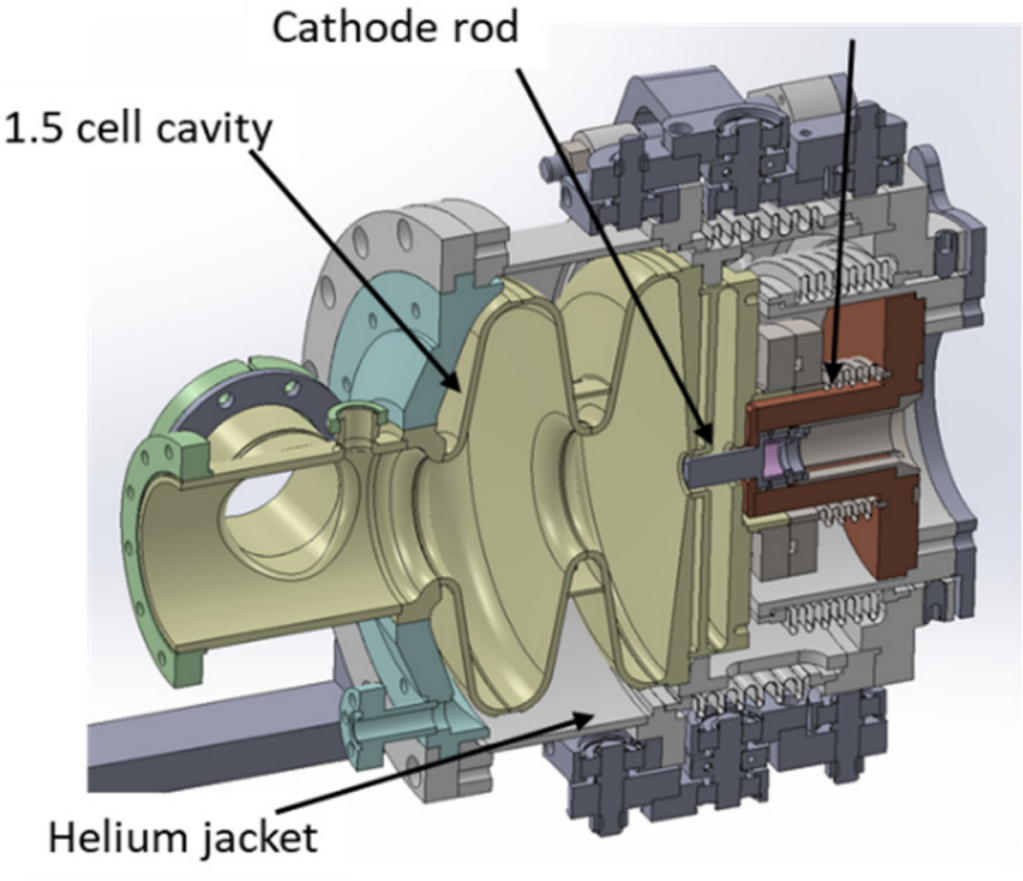

Figure 2.4: A schematic of the KEK gun cavity in a helium jacket and gun holder [18].

cleaning protocol. The KEK team has recorded a peak gradient upwards of 75 MV/m in the gun cavity, and have ambitions of 42 MV/m with a cathode stalk inserted and an electron beam generated, which are known to hamper the maximum achievable gun cavity gradient [18]. For the simulations with the KEK gun, we kept the maximum allowable gradient at 50 MV/m as a suitably optimistic, but reachable, gradient upper bound. Additionally, this gradient bound matched the WiFEL gun maximum gradient to facilitate a better comparison between the respective 1.5 cell and quarter cell cavity designs.

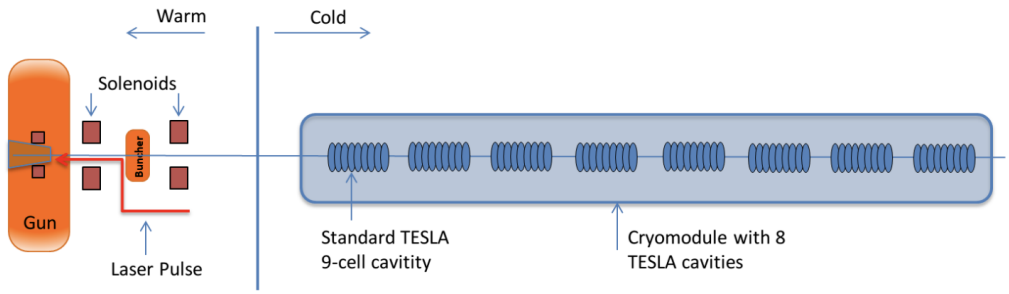

Figure 2.5: A cartoon of the LCLS-II injector showing components used in the ASTRA simulations [22].

2.3 Optimization Methodology

As mentioned above, I started this simulation campaign with the end result of the optimization from the original LCLS-II optimization campaign [2] [22]. I used the LCLS-II injector lattice that is currently being commissioned at SLAC as the lattice starting point. A simplified LCLS-II injector system with only the components used in the injector lattice simulations is shown in Figure 2.5. From this LCLS-II baseline, the task at hand became to re-optimize the injector lattice after either the cathode quality or gun cavity were upgraded.

2.3.1 Injector Simulations with ASTRA

To simulate an injector system, we used A Space charge TRacking Algorithm (ASTRA) [12] to track as electron beam through the various injector components. ASTRA splits the particle beam (typically 100 pC of charge for the simulations presented here) into a specified number of macro-particles that get assigned to the nearest point on a grid. We typically used 10,000 macro-particles for the ASTRA simulations described here. ASTRA assumes cylindrical symmetry for all fields generated by injector components. ASTRA reads in field files that describe the field on the center beam axis for the various injector components, such as gun field,

Parameter	Result
Longitudinal bunch length	1.0 mm
100% RMS x emittance	0.30 mm mrad
95% RMS x emittance	0.23 mm mrad
End Injector Energy	93.9 MeV

Table 2.2: The simulation starting point for the LCLS-II injector for a 100 pC electron beam. These emittance, bunch length and energy predictions were simulated with the ASTRA simulation tool.

solenoid fields etc. (typically the electric or magnetic field magnitude as a function of longitudinal position at $r = 0$). ASTRA then solves Maxwell's equations accordingly to extrapolate the provided fields on the center beam axis to anticipated fields at varying radii away from the center beam axis. The resulting fields are then used to calculate the effects on the trajectory of each macro-particle during the given time step, before the process is repeated at the next simulation time step. ASTRA additionally models the space charge repulsion between electrons in the beam. The ASTRA simulation baseline result for the LCLS-II injector system is shown in Table 2.2 and is the expected emittance and bunch length for a 100 pC electron beam at the end of the injector system. The injector knob settings for the LCLS-II injector results shown in Table 2.2 were selected during the LBNL LCLS-II injector optimization campaign [2].

2.3.2 Multiobjective Genetic Algorithms for Photoinjector Lattice Optimization

The main challenge when attempting to assess the impact of an injector system upgrade, such as changing the gun cavity or improving the cathode thermal emittance, is that many of the injector settings need to be adjusted to provide optimum performance for a given upgrade. As described in Section 1.4, each of the injector system components contribute emittance growth in various ways,

providing a significant optimization obstacle. Once the components of the lattice are selected, the list of variables that could be optimized is rather long: laser spot size and pulse duration, cavity gradients and phases, solenoid strengths and component lattice positions. Additionally, we have multiple and often conflicting figures of merit that are important to consider: emittance, bunch length, end energy and energy spread to name a few. To suitably optimize, we require a way to balance several key parameters and objectives to determine the usefulness of an injector system for an FEL type application. To do this, we will employ the use of evolutionary algorithms.

In 2005, researchers from Cornell University applied evolutionary algorithms to optimize a high brightness DC gun photoinjector [4]. Since then, using evolutionary algorithms, or Multiobjective Genetic Algorithm (MOGA) optimization, has proven to be an effective, and popular, tool to design, tune and optimize an injector lattice. For this simulation study, we used the same simulation tool that the LCLS-II injector researchers used for their MOGA optimization: the non-dominated sorting genetic algorithm II (NSGA-II) [9] that drove parallel ASTRA simulations [22].

We used NSGA-II to select injector lattice knob settings to determine the solution set that maps the trade-off between the two main objectives: the final 95% transverse emittance and the final longitudinal bunch length. A shorter bunch length occurs at the expense of increased space charge effects which adversely competes with minimizing the emittance. Therefore, there exists a set of solutions that place slightly different weights on either the bunch length or the transverse emittance. This set of solutions showing how the two competing objectives trade-off is called a Pareto Front. Our goal is to find the emittance and bunch length Pareto Fronts for all the lattice configurations we will explore. The LCLS-II

project is nominally interested in a bunch length around 1 mm at the end of the injector system so, lastly, I will select one specific population member with a bunch length around 1 mm from the Pareto Front solution set to compare across differing lattice setups.

The details of the NSGA-II algorithm are outside of the scope of this dissertation but we will provide a brief overview of the most salient features for the NSGA-II as implemented for an injector lattice optimization [9]. We input into the NSGA-II algorithm the number of and range for various injector knobs, or variables of interest, such as initial electron beam spot size rms or gun phase. To begin, the evolutionary algorithm makes a large number of population members, N, that are initially generated with randomly assigned knob values within the specified variable range. For our implementation, the trial solutions are ASTRA simulations that run on parallel compute platforms with changed injector parameters. Once the ASTRA simulations are complete, the emittance, bunch length and constraint parameters are collected.

For the first generation, the sorting is done with just the results of the N initial population members. For every generation past the initial generation, the past results of the Parent population are combined with the results of the newly run Offspring population to form a $2N$ population for sorting to determine the next Parent population. The inclusion of the Parent population in the sorting process ensures that successful population members from previous generations are carried through.

In addition to the two main objectives, emittance and bunch length, additional end parameters are necessary for feasibility of an injector system, such as end energy and energy spread. NSGA-II accommodates these as a binary constraint flag where end results are compared against a suitable cut-off threshold that is

user specified. The $2N$ population members are initially categorized and ranked based on number of constraints violated. For population members with the same number of constraints violated, the members are sorted into non-dominated sets, F_i. A population member, X, is said to dominate another population member, Y, if neither objective in X is worse than in Y, and there is at least one objective in X better than the same objective in Y. F_1 is populated by all the population members that are not dominated by any other population members. F_2 is populated by all the non-dominated population members once F_1 members are no longer considered. This process is repeated until all population members with the same number of constraints violated have been sorted into their respective F_i.

The next Parent population is selected by letting in the non-dominated F sets one at a time until there is no more space to let in the entire F set. This last F set is sorted to let in population members that minimize solution crowding to fill out the remaining spots of a new, N sized Parent population. The NSGA-II sorting process is pictorially described in Figure 2.6.

Once the Parent Population for the forthcoming generation has been selected, NSGA-II needs to create a new trial Offspring population. To make a new Offspring population member, NSGA-II crosses traits from two populations members from this new Parent populations with a preference for fitter populations. The algorithm also employs a mutation operator to add a random perturbation to some variables in a population member to diversify the generated Offspring. NSGA-II does this N times to fill out a new Offspring population. With the new Offspring population generated, another batch of ASTRA simulations are run to determine the improvement of this next generation. This process continues for numerous generations until the final generation converges on an optimum Pareto Front that maps out the dependence of the two competing objectives for various injector

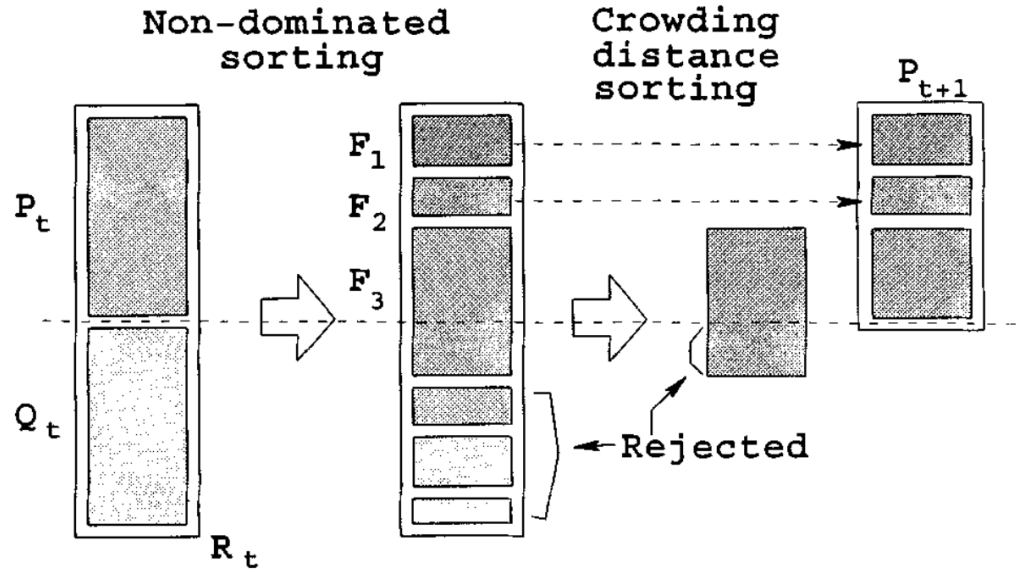

Figure 2.6: An overview of the NSGA-II sorting procedure. P is the parent population, while Q is the offspring population. For generations after the first generation, the Parent and Offspring populations are combined and assigned to sets F, where no solution dominates within a set. The next parent population is then selected by letting in the non-dominated F sets one at a time until there is not more space, where then the last F set is sorted to minimize crowding [9].

component settings.

I started with the previous LCLS-II lattice optimization settings which was the basis for the lattice elements used for the forthcoming simulation results. We kept the general flow of the LCLS-II injector lattice as pictorially described in Figure 2.5: a gun cavity where the beam originates followed by a solenoid that captures the beam and does the majority of the emittance compensation, a buncher cavity to help compress the electron beam if the beam is longer coming out of the injector, another solenoid for more emittance compensation and then the initial acceleration cryomodule which consists of eight 9-cell cavities to provide the bulk of the acceleration. The LCLS-II injector will utilize a low gradient, 2-cell NCRF cavity as a buncher cell. However, with an SRF gun, we would not

be limited to the lower gradient NCRF 2-cell cavity that was designed for the LCLS-II injector lattice that is currently driven by the NCRF APEX gun. For simulations with the KEK and WiFEL guns, I did some optimization runs prior to the start of this study that produced lower emittance results with a 9-cell instead of 2-cell buncher cavity. Therefore, for the simulations presented here, injector lattices with either the WiFEL or KEK gun use a SRF 9-cell cavity that matches the SRF cavities in the first accelerating cryomodule as the buncher cavity instead of the 2-cell buncher cavity used with the APEX gun. Additionally, the WiFEL gun project had progressed to gun tests with an electron beam and therefore had a solenoid designed to go with the WiFEL gun cavity. Since the KEK gun was also superconducting and did not have a solenoid designed for it yet, I used the WiFEL solenoid field file with the WiFEL and KEK lattices instead of the solenoid designed for the LCLS-II injector lattice.

The previous LBNL optimization campaign helped inform the knobs, or injector parameters, that would be varied here to optimize an injector lattice, with some additional knobs added for lattices with the WiFEL or KEK gun. The LCLS-II is in the process of commissioning with the APEX gun [31] so for simulations with the APEX gun, we wanted solely to determine the dependence of the final emittance if only the cathode was updated. Accordingly, we froze the positions of the components of the beamline to correspond to the injector that is currently being built at SLAC. Since the WiFEL and KEK gun cavities do not have dedicated injector systems for them yet, we did incorporate component position as knobs that could be optimized for lattices with the KEK and WiFEL guns. In the original simulations, the team wanted to be resilient to cavity failures in the initial cryomodule, which is made up of eight 9-cell cavities. To accomplish this, researchers intentionally set the RF amplitude of cavities two and three to

Knob	APEX Value Range	WiFEL Value Range	KEK Value Range
RMS sigma at cathode	0.05-2 mm	0.05 - 1 mm	0.05 -1mm
Bunch length at cathode	5-50 ps	5 - 70 ps	5-70 ps
Gun Gradient	20 MV/m	20-50 MV/m	20-50 MV/m
Gun phase	-45-10 deg.	-60 - 60 deg.	-60 - 60 deg.
Sol. 1 field	0.01-0.2 T	0 - 0.4 T	0 - 0.4 T
Buncher cavity field	0-2 MV/m	0 - 32 MV/m	0 - 32 MV/m
Buncher cavity phase	-120-0 deg.	-180 - 180 deg.	-180 - 180 deg.
Buncher cavity offset	-	0-2 m	0-2 m
Sol. 2 field	0-0.2 T	0 - 0.3 T	0 - 0.3 T
Sol. 2 offset	-	0 - 1.5 m	0 - 2 m
Cryomodule offset	-	0-3 m	0 - 3 m
Cavity 1 field	0-32 MV/m	0-32 MV/m	0-32 MV/m
Cavity 2 field	0 MV/m	0-32 MV/m	0-32 MV/m
Cavity 4 field	0-32 MV/m	0-32 MV/m	32 MV/m
Cavity 1 phase	-90-90 deg.	-90-90 deg.	-90-90 deg.
Cavity 2 phase	-	-90-90 deg.	-90-90 deg.
Cavity 4 phase	-90-90 deg.	-90-90 deg.	-90-90 deg.

Table 2.3: The knobs, or injector parameters, that were changed during the MOGA optimization and the range that the knobs were allowed to change. Zero degrees is defined as the phase for max acceleration and the field gradients are the value of the maximum field in the field file. For configurations with the APEX gun, the buncher cavity was a 2-cell cavity while the WiFEL and KEK guns used a 9-cell cavity buncher cavity.

zero, with the intention that if another cavity became inoperable, either cavity two or three would be brought on with minimal impact to the beam quality. For lattices with the KEK or WiFEL guns, I was more optimistic about the future reliability of SRF technology and only set cavity three to zero to act as a spare cavity. The parameters I changed, along with the allowable ranges, for lattices with one of the three studied guns are documented in Table 2.3. The field profiles of a typical layout are depicted in Figure 2.7.

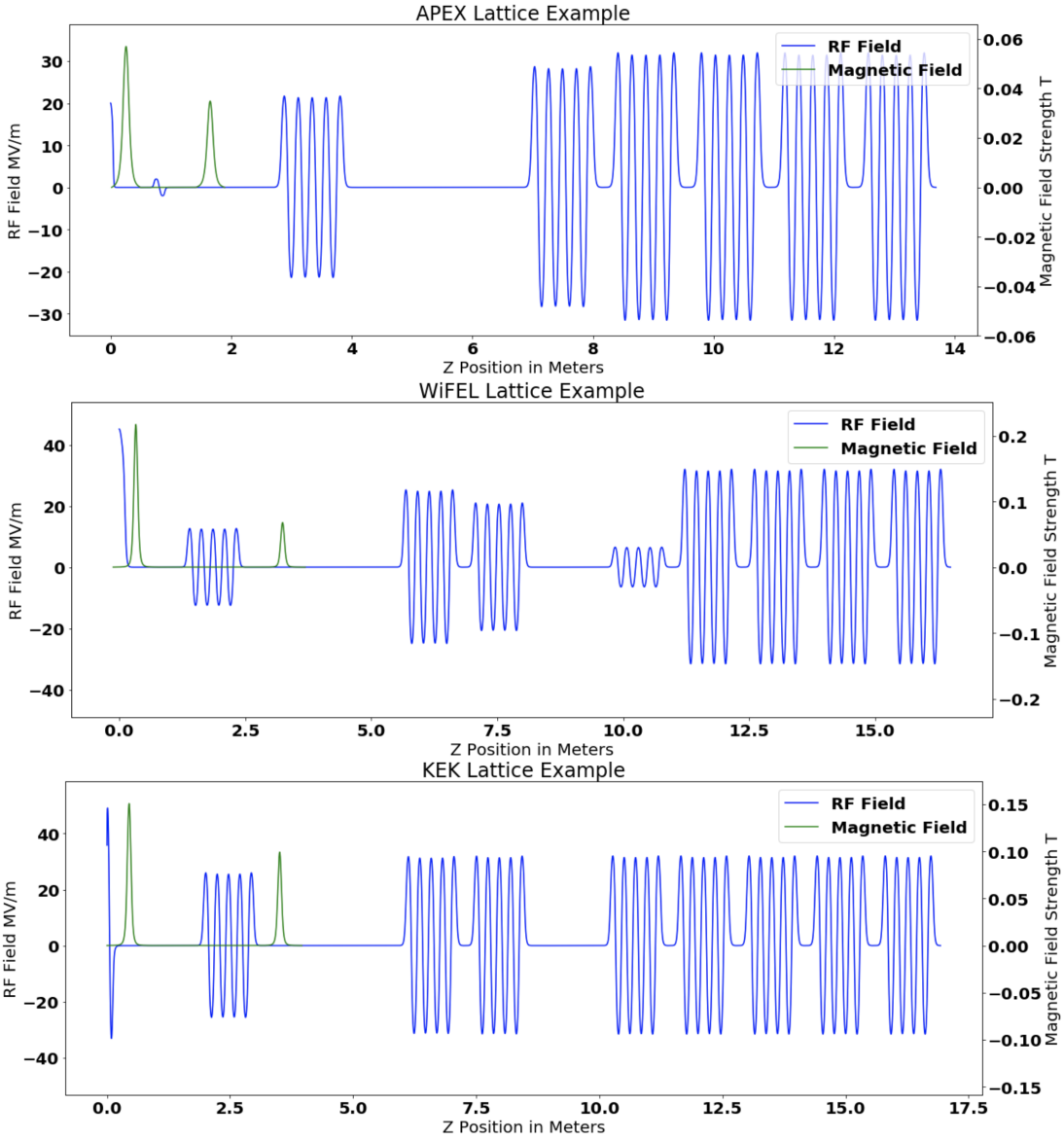

Figure 2.7: The field layouts for the various injector systems presented. The layouts consists of a gun cavity, solenoid, 2-cell or 9-cell cavity, another solenoid and finally the initial acceleration cryomodule that consisted of eight, 9-cell SRF cavities.

2.3.3 Perfect Cathode Simulations

The first simulation scenarios explored here are injector systems with beam emitted from a perfect cathode in order to document the theoretical Pareto Front for the minimum emittance and bunch length limit of injector lattices with one of the three different gun cavities. To create a perfect beam, I used ASTRA's particle generator program [12] to create a beam emerging from a perfect cathode where the emitted beam contains no longitudinal or transverse momentum spread. For the first runs with a perfect cathode, we did not want to limit solutions to FEL accelerator applications, which have high demands on energy spread constraints. We also were wary of over-constraining the algorithm which could give us a local optimized Pareto Front instead of the global optimized Pareto Front. Therefore, to start, I imposed fairly loose constraints on the energy spread of the beam at the end of the injector lattice, which allowed the optimizer to find an initial Pareto Front solution for multiple accelerator applications. As discussed above, constraints are binary conditions where population members are initially ranked on the number of constraints violated. The constraint flags used are:

1. The end energy is > 90 MeV
2. RMS bunch length must be less than 1.5 mm
3. 100% transverse emittance must be less than 1.0 mm mrad
4. Final energy spread < 500 keV
5. Higher Order (HO) Energy spread < 50 keV
6. The average $x_{pos}x_{angle}$ for all the electrons/ ASTRA particles in the beam is negative so we have a converging beam.

The higher order (HO) energy spread is calculated by fitting a second-order polynomial to the energy distribution in the beam versus longitudinal position and finding an RMS energy spread after subtracting out this polynomial of best fit. Section 1.2 provides more details about how the constraint values are calculated.

The NSGA-II algorithm started the perfect cathode simulation effort by creating 80 population members. A population member is defined as a unique set of values for the knob parameters detailed in Table 2.3. For example, for the WiFEL gun lattices, a population member would be a point in the 17-dimensional knob parameter space. Initially the knob values are assigned randomly in the specified range. The NSGA-II then writes an ASTRA input file with the selected knob values. The 80 ASTRA files are run in parallel until complete, when pertinent end values are reported to the NSGA-II algorithm, such as end emittance, bunch length and energy spread.

As discussed above, NSGA-II then ranks the Offspring and Parent population members together based on number of constraints violated first. If the number of constraints violated are the same, emittance and bunch length values are compared to sort population members into non-dominated sets. A population member dominates if neither emittance or bunch length have a worse/higher value and either the emittance and/or the bunch length is better/lower. The top 80 ranked Offspring and Parent populations are then the new 80-member Parent population for the next generation. NSGA-II creates a new Offspring population that selects knob values from the sorted new Parent generation with a preference for higher ranked, or fitter, population members with new knob settings incorporated through a "mutation" process done at a specified rate. The next generation is run with this newly assembled population and the process is repeated for many generations until a Pareto Front converges.

We obtained converged Pareto Fronts with a perfect cathode and then wanted to see how more stringent energy spread constraints would move the Pareto Fronts for each of the three guns. First, we tightened the overall energy spread constraint from 500 keV to 200 keV. The 200 keV constraint values matches previously per-

formed LCLS-II optimization work and was imposed to ensure a sufficiently small energy spread at the undulator hall[22]. To save computing time, which is a legitimate bottleneck of this simulation work, we did not assign the initial populations members with randomly assigned knob values but instead seeded the initial population with the knob values from the final generation from the perfect cathode run with looser energy constraints. We then continued optimizing for sufficient generations to get a satisfactory Pareto Front with the harder energy spread constraint setting.

Next, we took the end generation with the tightened energy spread constraint and further tightened the higher order (HO) energy spread constraint from 50 keV to 5 keV. The constraint threshold of 5 keV was selected on the advice of LCLS-II accelerator physicists who were noticing large energy spreads at just the head and tail of the beam at the start of the undulator hall in their simulations that modeled the beam through the entire linac lattice. A comparison of the three Pareto Fronts with a perfect cathode for the various energy spread constraints for the three gun types are in Figure 2.8 to Figure 2.10. A discussion of how the Pareto Fronts changed in response to the various energy spread constraints will be provided in Section 2.4.

2.3.4 Simulations with Cathode Emittance

The next part of the simulation study was to determine how introducing cathode emittance effects the optimization between the end transverse emittance and bunch length. For this cathode emittance study, we focused on FEL applications and used the stricter, FEL specific constraints for the end RMS energy spread and higher order energy spread of 200 keV and 5 keV respectively.

We simulated the cathode quality by using a set Thermal Emittance (TEmit),

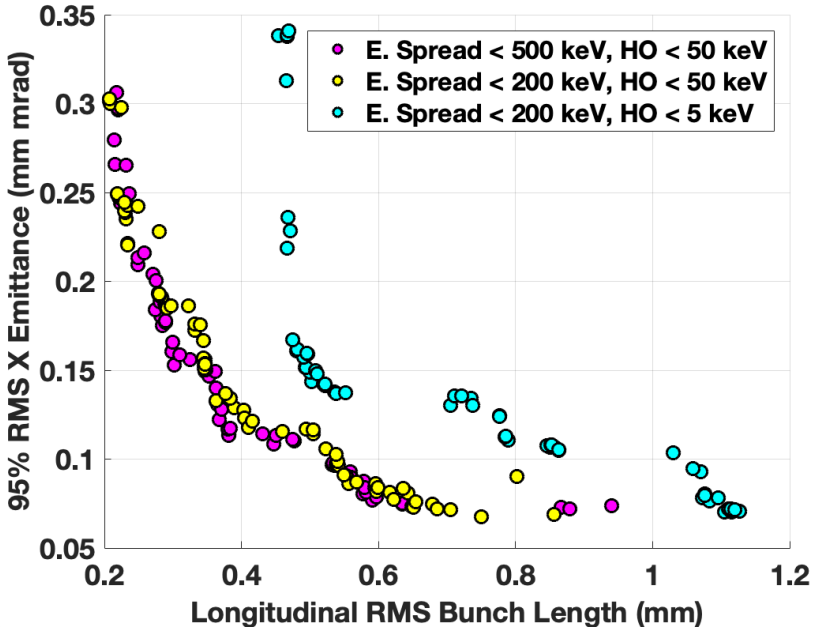

Figure 2.8: APEX Gun: Pareto Fronts for the APEX gun and a perfect cathode that pictorially show the impact of imposing FEL specific energy constraints.

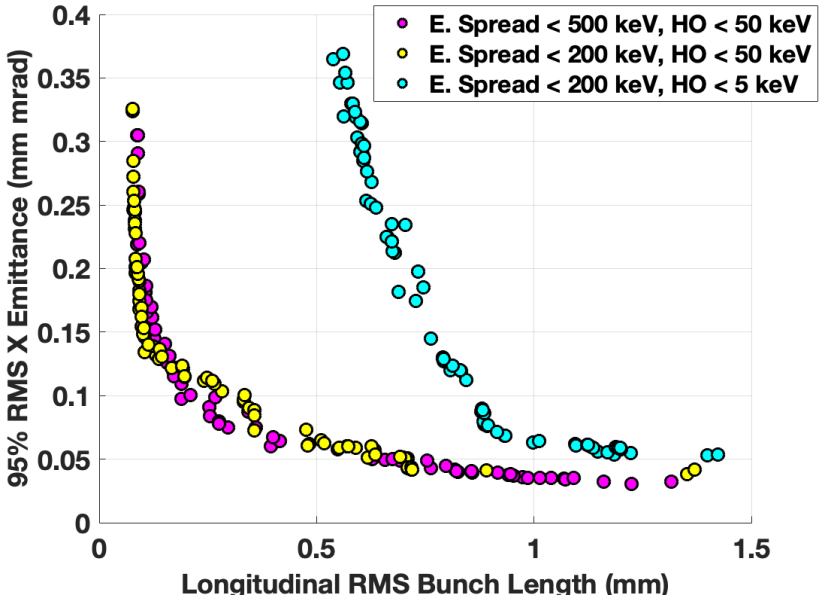

Figure 2.9: WiFEL Gun: Pareto Fronts for the WiFEL gun and a perfect cathode that pictorially show the impact of imposing FEL specific energy constraints.

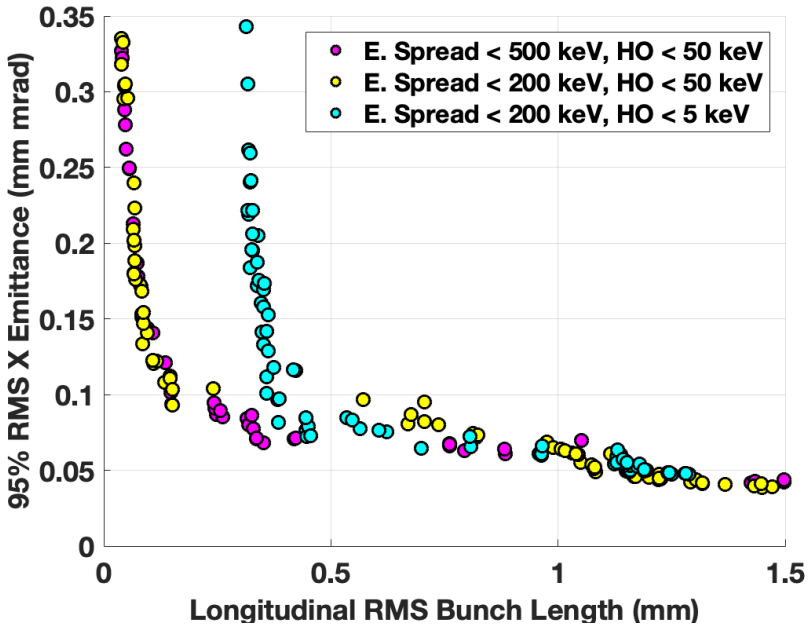

Figure 2.10: KEK Gun: Pareto Fronts for the KEK gun and a perfect cathode that pictorially show the impact of imposing FEL specific energy constraints.

or emittance per mm spot size, value to describe the initial momentum distribution for the electron beam off of the cathode. We selected an isotropic momentum distribution to describe the beam off of the cathode. An isotropic momentum distribution models the excess energy the electrons have after being freed by the photoelectric effect as a momentum vector that can be in any direction in a half sphere direction off of the cathode. The isotropic momentum distribution is common in other injector simulation work as it realistically couples the initial electron beam's transverse and longitudinal momentum spreads [27][12].

To help mitigate the concern of getting stuck in a local minimum, I started the cathode portion of the study with a cathode having a thermal emittance of 1 mm mrad/mm rms without seeding with the end population members of previously run configurations, instead opting to have the knob settings for the first generation assigned at random. I ran the simulations for intermediary cathode emittances

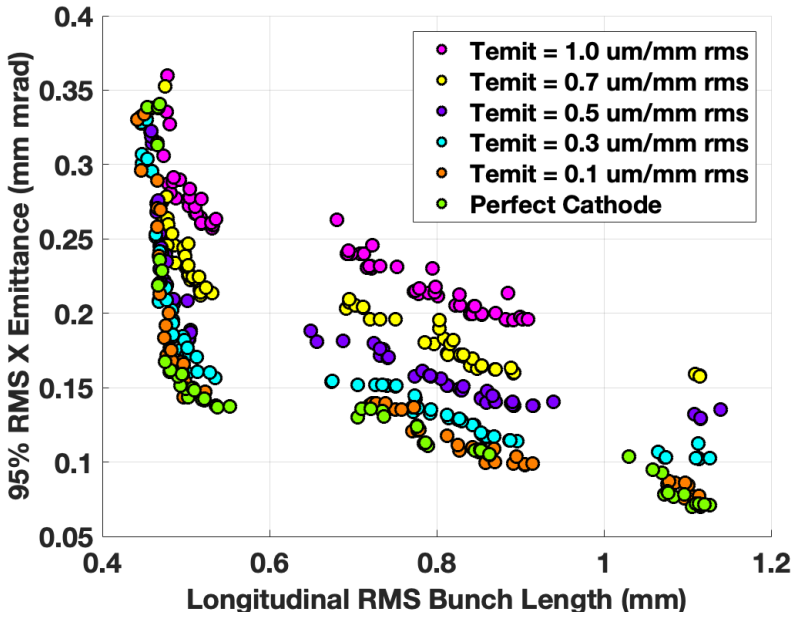

Figure 2.11: APEX Gun: Pareto Fronts that pictorially show the dependence of the cathode emittance on the final Pareto Fronts. The gaps in the Pareto Front around 0.6 mm and 1 mm showcase a limitation in the NSGA-II algorithm as, while solutions undoubtedly exist at these bunch lengths, the algorithm was unsuccessful at finding solutions there. Additionally, the perfect cathode results should always perform better than results with cathode emittance, showing that sometimes a local minimum is found as opposed to a true global minimum. For the units in the legend, I condensed mm mrad to um.

by seeding the initial population with 40 members each from the perfect cathode end population with stricter energy constraints and the 1 mm mrad/mm rms cathode baseline. The MOGA algorithm then ran for sufficient generations to let the Pareto Front converge. The Pareto Front solutions for lattices with the three guns with cathodes of various thermal emittances are shown in Figure 2.11 to Figure 2.13. Discussion on how the Pareto Fronts are impacted by various levels of cathode emittance will be provided in Section 2.4 below.

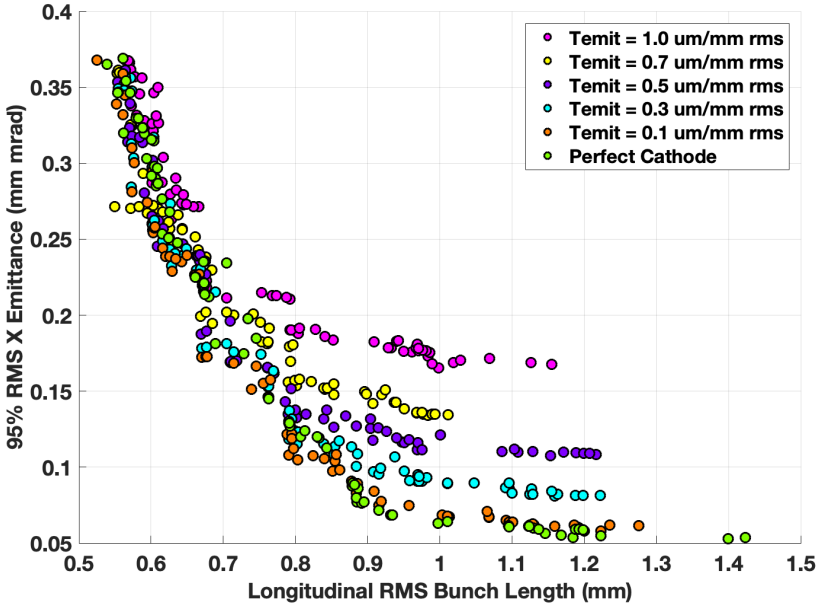

Figure 2.12: WiFEL Gun: Pareto Fronts that pictorially show the dependence of the cathode emittance on the final Pareto Fronts. For the units in the legend, I condensed mm mrad to um.

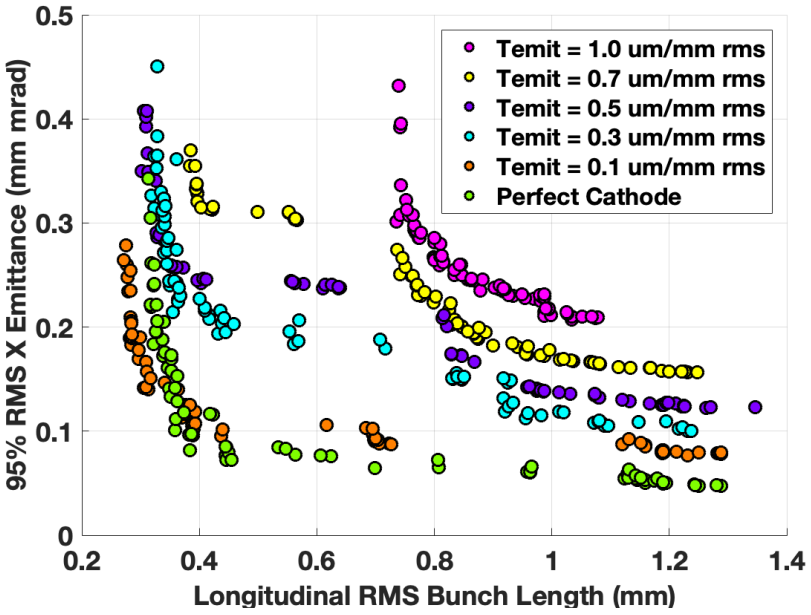

Figure 2.13: KEK Gun: Pareto Fronts that pictorially show the dependence of the cathode emittance on the final Pareto Fronts.

2.4 Analysis

Through this simulation campaign, we aimed to decouple the cathode and injector lattice emittance contributions towards the final injector emittance. With Pareto Fronts in hand, we can now answer the questions we initially set out to address: What are the emittance benefits of switching to an SRF gun cavity? And how good of a cathode do we need with each gun type to achieve 0.1 mm mrad RMS emittance at the end of the injector system?

The LCLS-II project is interested in a beam with a longitudinal length of around 1 mm at the end of the injector system so I manually picked the lowest emittance population member in the 0.9-1.2 mm range to compare and represent their population. Highlights of figures of merit for individual members of their respective populations are shown in Table 2.4. All displayed results are with 10,000 ASTRA particles with 100 pC but there is typically a 10% emittance reduction when 200,000 particles are used with finer meshing so we rounded down in the estimation of the cathode quality needed to meet the LCLS-II HE specification of 0.1 mm mrad 95% emittance.

The objective of the Pareto Fronts provided are to start documenting the benefits from further cathode research versus pursuing harder gun technologies, such as SRF guns. While the Pareto Fronts presented are not perfect and contain markers for being in a local minimum instead of at a true optimized front, the Pareto Fronts still represent an informative solution set that gives conservative guidance on the quality of cathode needed for each of the three gun types explored.

It is interesting to note that if we found a perfect cathode, all three guns investigated would meet the sub 0.1 mm mrad /mm rms emittance goal set by the LCLS-II HE project. From the best Pareto Fronts found so far, we estimate that we would need cathodes with 0.3, 0.5 and 0.3 mm mrad/ mm for lattices

APEX Gun Configs	Emit. at Cath. mm mrad	100% X Emit. mm mrad	95% X Emit. mm mrad	Long. Size mm	E. Spr. keV
E. Sp., HO < 500, 50 keV	0	0.111	0.074	0.94	296.7
E. Sp., HO < 200, 50 keV	0	0.108	0.069	0.86	157.7
E. Sp., HO< 200, 5 keV	0	0.113	0.070	1.11	66.6
TEmit = 0.1 $\frac{\text{mm mrad}}{\text{mm rms}}$	0.017	0.122	0.076	1.1	104
Therm Emit. = 0.3	0.054	0.152	0.103	1.07	131.9
Therm Emit. = 0.5	0.087	0.181	0.130	1.12	77.2
Therm Emit. = 0.7	0.122	0.215	0.158	1.12	76.9
Therm Emit. = 1.0	0.16	0.261	0.196	0.91	185.4
WiFEL Gun Configs	Emit. at Cath. mm mrad	100% X Emit. mm mrad	95% X Emit. mm mrad	Long. Size mm	E. Spr. keV
E. Sp., HO < 500, 50 keV	0	0.071	0.035	1.07	325.5
E. Sp., HO < 200, 50 keV	0	0.072	0.041	0.89	54.8
E. Sp., HO < 200, 5 keV	0	0.091	0.063	1.0	98.7
TEmit = 0.1 $\frac{\text{mm mrad}}{\text{mm rms}}$	0.022	0.096	0.068	1.01	81.9
Therm Emit. = 0.3	0.065	0.122	0.089	1.01	82.0
Therm Emit. = 0.5	0.088	0.140	0.110	1.11	71.7
Therm Emit. = 0.7	0.108	0.169	0.134	0.98	116.5
Therm Emit. = 1.0	0.127	0.211	0.165	1.0	129.1
KEK Gun Configs	Emit. at Cath. mm mrad	100% X Emit. mm mrad	95% X Emit. mm mrad	Long. Size mm	E. Spr keV
E. Sp., HO < 500, 50 keV	0	0.098	0.049	1.16	109.6
E. Sp., HO < 200, 50 keV	0	0.098	0.049	1.16	109.6
E. Sp., HO < 200, 5 keV	0	0.107	0.054	1.12	119.1
TEmit = 0.1 $\frac{\text{mm mrad}}{\text{mm rms}}$	0.050	0.145	0.088	1.12	140.1
Therm Emit. = 0.3	0.060	0.140	0.105	1.09	152.0
Therm Emit. = 0.5	0.101	0.181	0.136	1.03	194.2
Therm Emit. = 0.7	0.146	0.207	0.161	1.13	87.9
Therm Emit. = 1.0	0.185	0.269	0.207	1.03	192.0

Table 2.4: From each of the Pareto Fronts displayed in this dissertation, we selected one population member with a longitudinal length around 1 mm long to compare in this table. All simulations were done with 10,000 ASTRA particles.

with the APEX, WiFEL and KEK guns respectively. The higher gun gradient of the WiFEL gun did provide an emittance advantage over the similar NCRF APEX cavity indicating that SRF cavities could significantly ease the cathode requirement needed to achieve the 0.1 mm mrad emittance goal for the LCLS-II HE project.

2.4.1 Knob Responses to Pareto Front Settings

There is an onslaught of data to sift through to determine how all the variables change to accommodate either larger cathode emittance or different energy constraints. Here we will describe some noteworthy knob changes that had to happen to accommodate either changing energy spread constraint thresholds or variable cathode emittance levels. In Figure 2.14 through Figure 2.16, we plot the energy spread, 95% RMS transverse emittance and the bunch length as a function of the injector position, z, for the population members near 1 mm that are represented in Table 2.4. These plots as a function of z, coupled with the lattice field files shown in Figure 2.7, try to pictorially show which injector knobs had to change to accommodate either a harder energy spread constraint value, or a change in initial electron transverse spot size that was needed to minimize the spot size dependent thermal emittance off of the cathode for cathodes of decreasing quality.

For the APEX gun, as seen in Figure 2.8, reaching the 200 keV energy spread specification was almost immediate for the Pareto Front solution set. However achieving the 5 keV higher order (HO) energy spread constraint had a more pronounced impact. No configuration initially met the HO energy constraint and the only populations that could survive this harder constraint had a much smaller initial spot size on the cathode, slightly shorter initial beam off the cathode as well as different capture cavity and cryomodule phases. For the population members

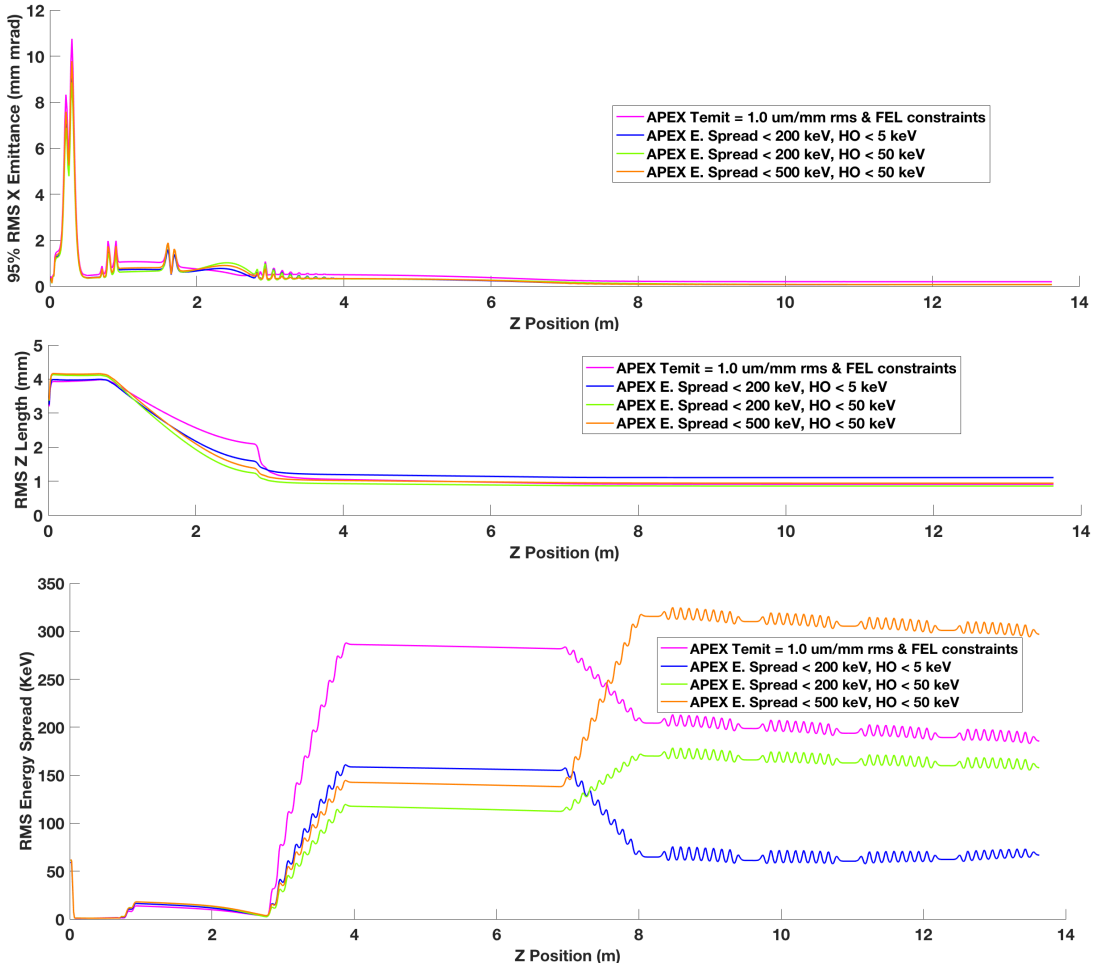

Figure 2.14: APEX Gun: Emittance, bunch length and energy spread comparisons for a population with an end bunch length around 1mm. The APEX gun lattices naturally selected for a smaller RMS spot size of the initial electron beam off of the cathode. For minimizing the HO energy spread, that phase and magnitude of cavity four (located around z = 7.5 m) proved to be the most impactful knob. For the units in the legend, I condensed mm mrad to um.

with a small initial spot size, the HO energy spread was then seemingly fixed by adjusting the cavity 4 phase as can be visually seen in the APEX energy spread plot as seen in Figure 2.14. Because the HO energy spread constraint already necessitated the smaller spot size, the variables did not change very much when the cathode emittance was added back in. The plots coupled with the table indicate that we would need a cathode around 0.3 mm mrad/mm rms thermal emittance to have a chance of meeting the 0.1 mm mrad emittance specification with the normal conducting APEX gun.

The WiFEL, quarter cell gun had similar tendencies to the APEX gun which makes logical sense as the field files and frequencies are similar, with the main difference the maximum achievable gun gradient. Imposing a harder energy spread constraint was ultimately recoverable but the WiFEL population did not initially have any configuration that met the harder HO energy spread constraint. The population had to find solutions with smaller initial spot sizes (around 0.2 mm) on the cathode, increased buncher gradient and different downstream phases of the first two cavities of the cryomodule to ultimately decrease the HO energy spread. The small spot size on the cathode then led to an easier time dealing with degrading cathode qualities and a straight forward cathode dependency is shown in Figure 2.12.The plots and table demonstrate that we would need a cathode of 0.5 um/mm rms with a SRF quarter cell gun to have a chance of meeting the 0.1 mm mrad specification.

The KEK gun had the easiest time meeting the harder energy spread constraints as the algorithm naturally selected for short pulses with a larger transverse spot size, minimizing the RF induced energy spread. With a perfect cathode, the bunch is actually short enough straight off the cathode that the initial capture cavity is purely accelerating the beam. The larger spot sizes proved difficult to

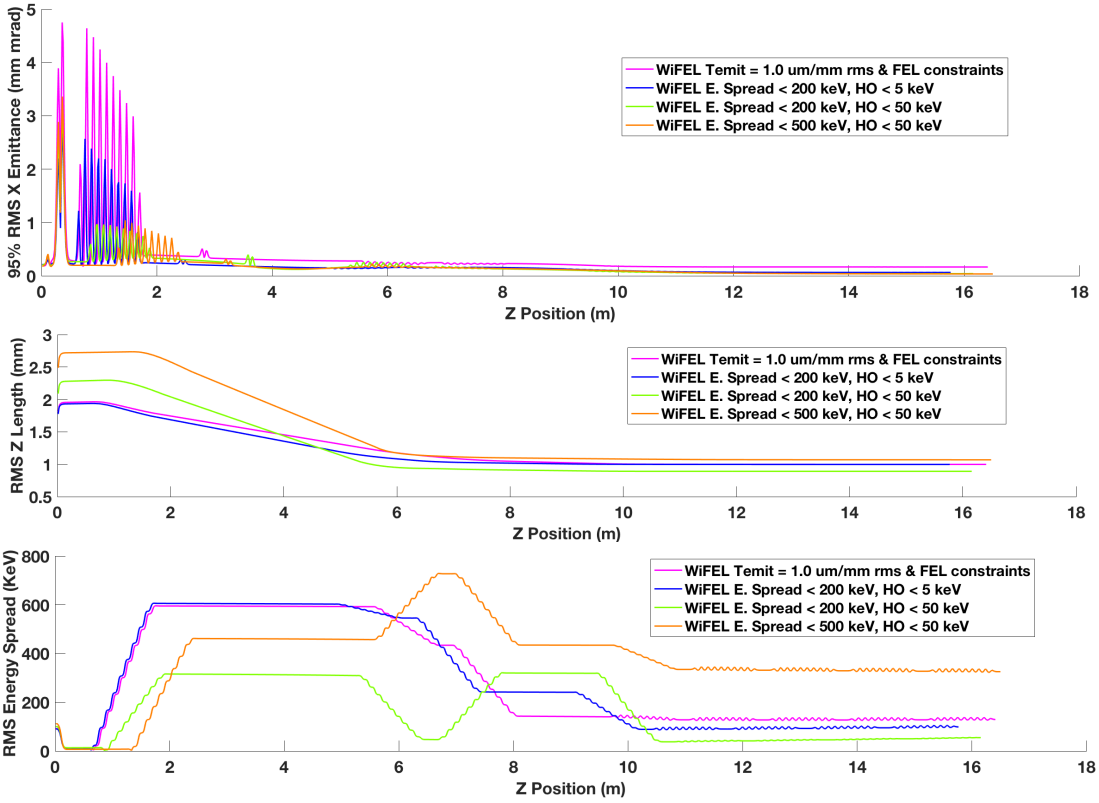

Figure 2.15: WiFEL Gun: Emittance, bunch length and energy spread comparisons for a population with an end bunch length around 1mm. The WiFEL gun naturally selected for a smaller spot size so the lattice did not have to change drastically to accommodate a higher cathode emittance. Several RF cavity phases had to change to accommodate the various energy spread constraints, as evidenced by the energy spread versus z plot.

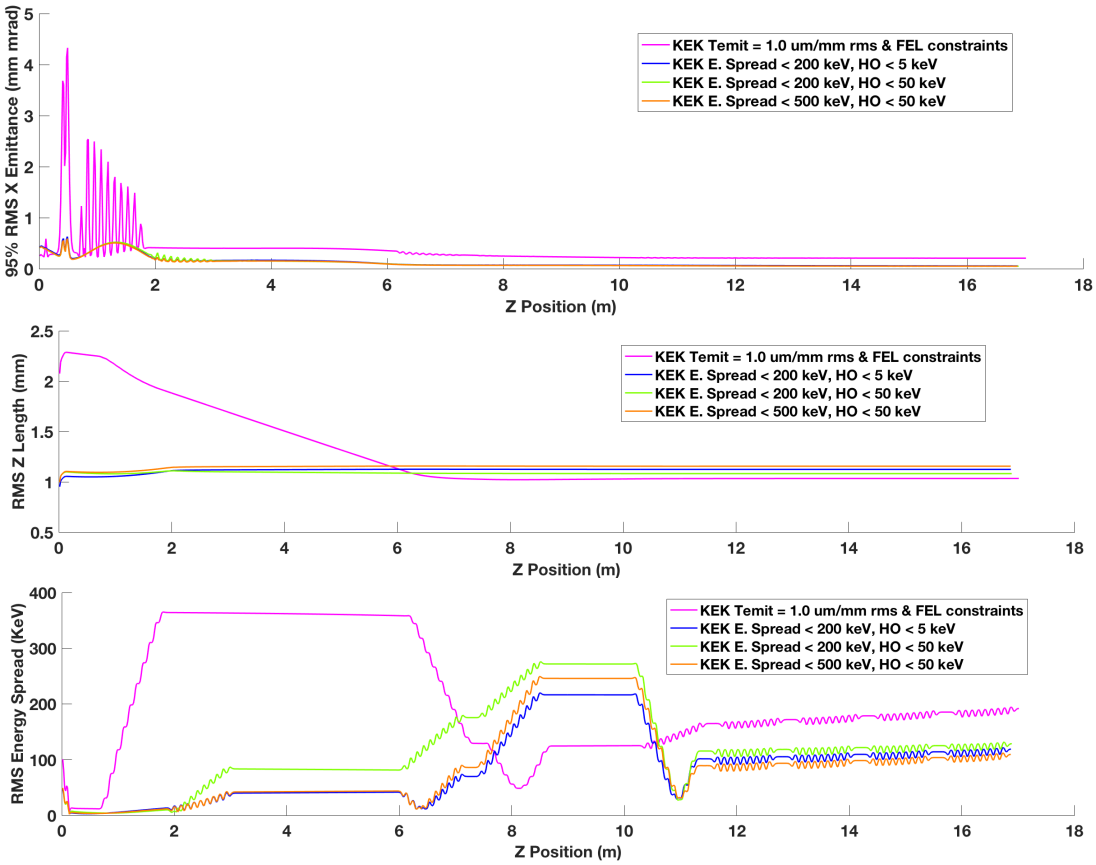

Figure 2.16: KEK Gun: Emittance, bunch length and energy spread comparisons for a population with an end bunch length around 1mm. The perfect cathode scenarios optimized with a larger initial beam spot size on the cathode meaning the lattices with larger cathode emittance had to completely re-optimize which is visually apparent between the different lattice responses between the TEmit = 1 config (Pink) and the perfect cathode configurations.

shift when the cathode emittance was added back in as there are dependancies between too many variables. We ran a fresh baselines with a cathode that produced a beam with 1 mm mrad/ mm rms thermal emittance and then combined perfect cathode results with the 1 mm mrad/ mm rms cathode baseline to promote merging between the two vastly different populations. However, in practice, the fronts depict when the perfect cathode population settings become more preferential to the 1 mm mrad/ mm rms cathode population. Results so far indicate that an injector with a KEK gun would need a cathode emittance of around 0.3 um/ mm rms to meet a 0.1 mm mrad 95% emittance goal.

2.5 Closing Thoughts: Next Steps and Study Limitations

The followup opportunities for this simulation work are plentiful: there are infinite injector scenarios to try to keep decreasing the emittance contributions from the injector system to ease the cathode requirements. Just to highlight a few, we could continue the study with lattices with more capture cavities in the lattice, various initial beam shapes emitted from the cathode as well as exploring guns at different frequencies.

The MOGA optimization strategy, while very useful to explore a vast parameter space to optimize an injector system, does have limitations to note here. The main limitation of the simulation study is that there is no way to definitively know that the Pareto Front produced is truly the global optimum. Especially for the KEK gun, the algorithm proved to be slow to adapt for all the variables needed to change to accommodate a smaller spot size on the cathode when this is penalized with larger cathode emittance. The algorithm mutation and crossover parameters

were played with but a perfect recipe of number of generations, algorithm hyper-parameter and ASTRA particle size that prevents getting in local minimum with reasonable computation time is still elusive.

Chapter 3

Designing a Solenoid for a Superconducting RF Photoinjector System

3.1 KEK SRF Gun Overview

The simulation work in the previous chapter showed the potential of Superconducting Radio Frequency (SRF) photoinjector systems to decrease the beam emittance out of the injector. SRF injectors enable the possibility of a higher gun acceleration gradient than their Normal Conducting RF gun counterparts while meeting the demands of a high beam repetition rate. Motivated by the desire to understand the current state of SRF photoinjector technology, I performed the work presented in this chapter during a 2019, year-long research stint at Japan's KEK laboratory in Tsukuba, Japan to get hands-on experience with these SRF injectors.

KEK is building and developing an SRF photoinjector that will provide a

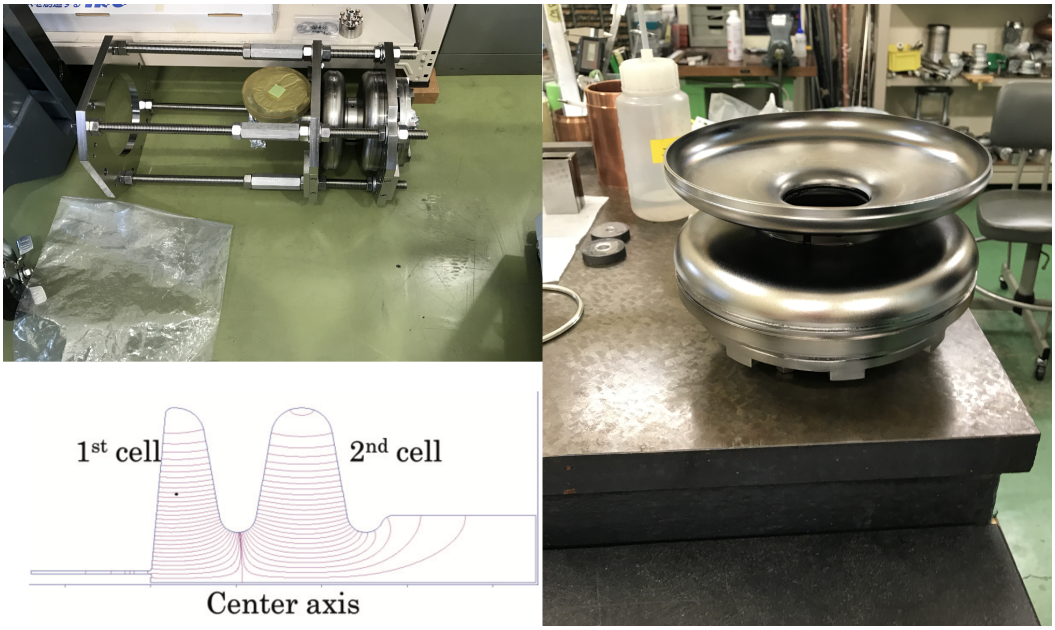

Figure 3.1: The KEK gun cavity designed by Taro Konomi. Top Left: The Niobium cavity in the cavity stand. Bottom Left: The 3D field file for the KEK gun done in SuperFish. Right: The bare KEK niobium gun cavity.

high quality beam for the KEK compact Energy Recovery Linac (cERL) facility. Presently, the cERL can operate an infrared FEL with 60 pC bunches at 81.25 MHz [15]. Currently the cERL utilizes a DC gun to get the high average current required for an ERL but the goal is to ultimately upgrade the cERL facility from a 17.5 MeV to a 3 GeV facility. The DC gun delivers a 500 keV electron beam with an emittance of 3 mm mrad at the undulators. The goal is to upgrade the DC gun to the KEK SRF gun, which is expected to provide a higher quality beam that reduces the emittance down to 0.6 mm mrad [23]. The KEK gun cavity was designed by Taro Konomi and the KEK SRF gun group as a 1.3 GHz, 1.5 cell SRF electron gun. The gun cavity prototype is shown in Figure 3.1 and full design parameters are listed in Table 3.1 [18].

Prior to my arrival, my KEK mentor, Taro Konomi, had already fabricated the gun cavity. I entered the research group during the process of testing the

Design Parameter	Value
Beam Energy	2 MeV
RF Frequency	1.3 GHz
Bunch Charge	80 pC
Peak Electric Field	41.9 MV/m
Bunch Length (rms)	3 ps
Normalized Emittance	0.6 mm mrad
Energy Spread	$< 0.1\%$

Table 3.1: The design specs for the KEK gun cavity [18]

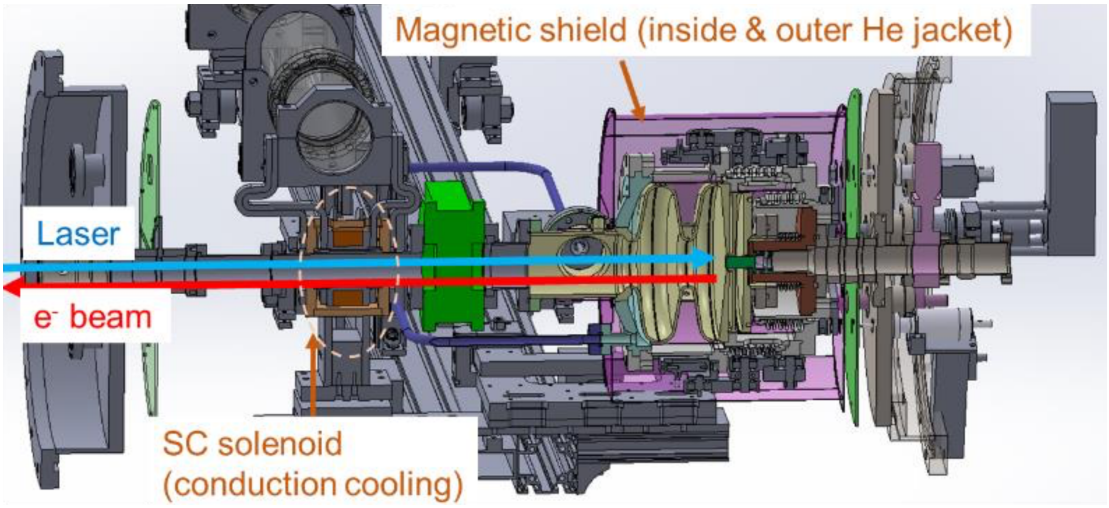

Figure 3.2: The CAD design of the KEK Gun Test Stand Cryomodule. The KEK gun cavity is inside the pink magnetic shielding. CAD image curtesy of Taro Konomi.

RF field performance of the cavity. After the cavity RF field characterization, the next gun commissioning step is to generate a beam with the SRF gun cavity and characterize the performance of the generated beam. In anticipation of this future commissioning milestone, we needed to design a gun test stand lattice. The exit of the RF gun cavity acts as a defocusing lens for the electron beam and we need a way to capture the beam coming out of the gun cavity to allow the beam to traverse the rest of the lattice and get useful characterization measurements. Therefore, the next part of a gun test stand is usually a solenoid that acts as a

focusing lens. The rest of the lattice consists of beam diagnostics to measure the beam emittance, energy and charge generated. I was placed in charge of designing the solenoid for the KEK SRF photoinjector test stand, a crucial item for not just the test stand but for the eventual full photoinjector lattice. The CAD model of the cryomodule test stand that shows the position of the solenoid relative to the gun cavity is shown in Figure 3.2.

3.2 Design Considerations for a Superconducting Solenoid

Solenoid magnets have been a common component of injector lattices for decades but there are additional design considerations when the solenoid accompanies an SRF gun cavity. As a refresher from Section 1.4.4, the solenoid component is needed to serve two functions in the injector lattice: first, the solenoid is crucial as a focusing lens for the beam that is defocused as it exits the RF gun cavity, as described in Chapter One Eq. 1.11. Secondly, the solenoid is an important component of the emittance compensation process that aligns the phase space slices in the beam to lower the overall emittance. We used a Multi-Objective Genetic Algorithm described in Chapter Two to determine the optimal maximum field produced by the solenoid that optimized the emittance compensation done by the solenoid for the respective injector lattices. The solenoid's general purpose is the same for all gun cavity type but SRF gun cavities necessitate solenoid design changes that are unique to SRF gun injectors.

The biggest complication for designing a solenoid for a superconducting gun cavity comes from the inability of the Niobium gun cavity material to become superconducting if there are sufficiently large magnetic fields present. If the mag-

netic field from the solenoid is too high on the cavity walls, the cavity material will quench, or stop being superconducting. Typically, for a Normal Conducting RF (NCRF) gun, the solenoid magnet either goes around the gun cavity to focus the electron beam right off the cathode or is directly after the cavity exit. These solutions are not an option for an SRF gun cavity, as the gun cavity would experience strong magnetic fields in these scenario. However, having the solenoid as close to the exit of the gun cavity as possible is necessary to prevent the beam from defocusing excessively as it exits the gun cavity. SRF injector systems require a compromise between the solenoid being as close as possible to the gun cavity and far enough away that we can still limit the magnetic field at the cavity down to a safe level.

The KEK test stand will be housed in an existing KEK cryomodule which motivated some design choices. The gun cavity extends about 0.25 meters from the location of the cathode. If we define $z = 0$ meters as the location of the cathode, the closest we could put the center of the solenoid due to an existing valve in the cryomodule is at 0.5 m. Therefore we started the solenoid designs with the solenoid centered around $z = 0.5$ meters to be as close as possible in the existing cryomodule design with the expectation that if we could not mitigate the magnetic field on the gun cavity wall down to sufficiently negligible levels, the solenoid could be moved further away from the gun cavity. The gun will be housed in a permalloy magnetic shield and from previous experience by KEK staff, they advised that the solenoid field levels before shielding should not exceed 0.5 G at the gun cavity exit ($z = 0.25$ m) and 10 mG at the cathode so that this remaining magnetic field can be sufficiently mitigated by the permalloy shield.

Although a strong magnetic field is required while the beam is in the solenoid, we would like to design the solenoid so that the field outside of the solenoid

magnet, called fringe fields, decays as rapidly as possible. To help minimize the strength of the fringe fields of the solenoid to further minimize the magnetic field strength on the gun cavity material, we included an iron yoke in the design. The iron yoke provides good shielding against fringe fields at low fields (under 1 T) as iron is a material with a high magnetic susceptibility and provides a preferred path for the magnetic field relative to air. However, the addition of the iron yoke necessitated the addition of another constraint that we do not exceed 1 T in the yoke to avoid magnetic saturation in the iron that would cause non-linear field effects.

To be placed 0.5 meters after the cathode, the solenoid needs to be inside the cryomodule that houses the gun cavity. This is another complication as a normal conducting solenoid has too high of a heat load from the resistance of the current going through the magnet coils to go inside a cryomodule. Therefore, an additional challenge to SRF photoinjectors is that the coils that make up the solenoid have to be superconducting. A KEK magnet engineer advised that the solenoid be wound with Niobium Titanium (NbTi) wire which necessitates a 8K maximum operating temperature to maintain superconductivity. The standard KEK cryomodule has a 4K liquid helium pipe that would be the cooling source for the magnet. KEK engineers have past experience using conduction cooling systems for superconducting magnets. Therefore we decided to design this KEK solenoid with rods that would connect to a bobbin holding the coils of the solenoid. The rods and bobbin would thermally connect the coils to the 4K liquid helium bath in the cryomodule. The rods and bobbin would be made of a material with low magnetic susceptibility and high thermal conductivity in order to move heat out of the magnet coils efficiently while not distorting the magnetic field.

The last design requirement of note is not unique to a superconducting solenoid

Requirement	Value
Required focusing strength for 2 MeV beam	200 mm
Max magnetic field in Iron	1 T
Max magnetic field at edge of gun cavity	0.5 G
Max magnetic field at cathode (0 m)	10 mG
Solenoid position after cathode	0.5 m
Max temperature of solenoid wire coil	8 K

Table 3.2: Requirements for the superconducting solenoid design for the KEK gun test stand.

but still crucially important: the focal length. We can determine the transverse emittance of the beam by scanning the solenoid strength versus the transverse spot size. The KEK gun test stand will have a profile monitor to perform this measurement, the position of which necessitates a center focus of 200 mm for the expected 2 MeV electron beam coming out of the gun cavity. For the solenoid design process, in my simulations, I made use of a scan range of 100-300 mm for the focal length to bracket the 200 mm design parameter. To calculate the solenoid focus, we make use of Eq. 3.1 which is derived in detail in Appendix A:

$$\text{focal length} = \text{f} \ = \frac{v_z^2 4m^2\gamma^2}{q^2 \int B^2 dz} \tag{3.1}$$

Here, v_z is the average longitudinal velocity of the electron beam going through the solenoid, γ is the average electron Lorentz factor, and $\int B^2 dz$ is the integral of the square of the magnetic field magnitude produced by the solenoid on the center beam axis.

Via simulation work presented in the forthcoming section, we will vary the solenoid length, radius and iron yoke dimensions to document the impact these parameters have on the field in the iron yoke, the magnitude of the fringe magnetic fields at the cathode and gun cavity edge locations while maintaining the required 200 mm focusing. We will keep the position of the solenoid fixed at the closest

possible position $z = 0.5$ m to determine if we can meet the requirements at this location or if a location further from the gun exit is required. We will model a conduction cooling system that can cool the superconducting magnet and determine how the magnetic fields are effected when the cooling rods are inserted through the iron yoke. Lastly, we will investigate the material of the bobbin and conduction cooling rods to determine the impact to the expected solenoid operating temperature. The summary of the full design requirements for the SRF solenoid are listed in Table 3.2.

3.3 Design Studies for a Superconducting Solenoid

This section will detail the design studies I performed to determine the design parameters of the superconducting solenoid that will be used on the KEK gun cavity test stand. There are still so few SRF photoinjectors that not many superconducting solenoids have had to be designed for this purpose. There are only two SRF guns regularly operating, only one of which has a superconducting solenoid: the SRF Gun II at the Helmholtz-Zentrum Dresden-Rossendorf (HZDR) that currently drives the ELBE project [24] [19].

The HZDR solenoid file was used to perform a solenoid length study. I simulated the expected magnetic field using the Poisson Superfish codes [21]. For each length simulation, I scaled the magnetic field strength to provide the desired focusing: a focal length of either 100 mm or 300 mm to bracket the 200 mm focal length. The focus of 200 mm was selected due to the downstream location of a profile monitor component but we needed a range of focuses to account for scanning the solenoid current to measure beam characteristics such as emittance. I tested 100 mm and 300 mm focuses for each of four solenoid lengths: 28 mm, 38 mm, 68 mm and 138 mm. I considered the magnetic field generated from the

solenoid at the cathode and edge of the gun cavity positions, and recorded the maximum field within the solenoid for reference. Results showing the effect of various solenoid lengths on the magnetic fringe field strengths are shown in Table 3.3.

Length mm	**Focus** mm	**B, Gun Exit** Gauss	**B, Cathode** mGauss	**Max B** T
28 mm	100 mm	0.473 G	0.032 mG	0.257 T
28 mm	300 mm	0.273 G	0.019 mG	0.148 T
38 mm	**100 mm**	**0.481 G**	**0.033 mG**	**0.245 T**
38 mm	**300 mm**	**0.278 G**	**0.019 mG**	**0.142 T**
68 mm	100 mm	0.594 G	0.040 mG	0.210 T
68 mm	300 mm	0.343 G	0.023 mG	0.121 T
138 mm	100 mm	1.63 G	0.1 mG	0.153 T
138 mm	300 mm	0.944 G	0.06 mG	0.088 T

Table 3.3: The summary of the solenoid length study with the HZDR solenoid design. Since the desired focus was 200 mm, we looked at parameters in a 100 mm focus range on either side. We ultimately decided to go with a solenoid that was 38 mm long.

Shorter solenoids produced smaller magnetic fields at the cathode and gun exit locations for the same focusing effect, which is desired. We ultimately decided to go with 38 mm as shorter solenoids provided diminishing returns in terms of magnetic field on the cathode and gun cavity but 38 mm was still long enough to be feasible to engineer.

To look at the impact various solenoid lengths had on the magnetic field strength at the gun exit and cathode locations, I changed the bobbin and coil length dimension of the HZDR solenoid and scaled the current through the coils to produced the desired focusing. However, the HZDR design had a specialized yoke that was not applicable to the KEK use case. Therefore, to study the yoke dimensions, I changed the design file away from the HZDR solenoid file to better tailor the design to the specific constraints of the KEK test stand. A 2D model

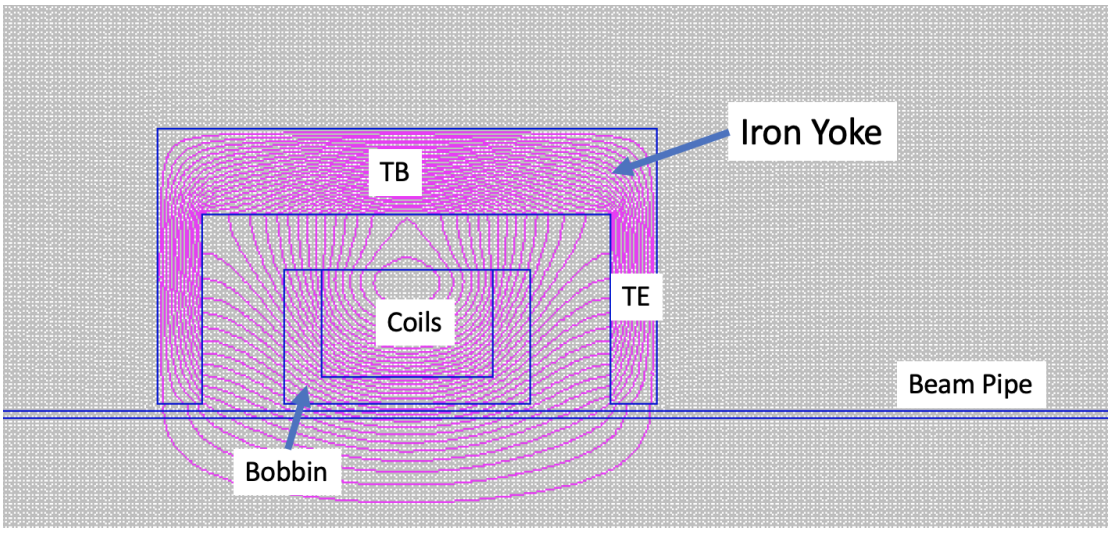

Figure 3.3: A 2D slice of the cylindrically symmetric solenoid model used for many of the design studies. The coils are a collection of wires that are wound around a bobbin that is necessary for mechanical support for the wires. The Iron yoke goes around the bobbin and coil and has a thickness of the outer washers TE, and thickness of the main cylinder, TB that were varied. TB and TE are pictorially defined here to show what dimensions were changed during the Yoke dimension study.

overview sketch of the simulated KEK solenoid used throughout the remainder of the design studies is shown in Figure 3.3.

In parallel, I set up a 3D version of the solenoid in CST Studio Suite and went back and forth between the two models as needed in the completed design studies. A 3D model is needed in order to start assessing the impact of the practical means to cool the solenoid coils. To provide cooling to the coils, rods will attach at specific angles to the bobbin holding the coils, go through holes in the iron yoke and connect to a 4K liquid helium bath. I used CST Studio Suite to setup the solenoid model in 3D so that I could break cylindrical symmetry to model the rods that will penetrate through the iron yoke. The 3D CST model and the axial magnetic field comparison between the solenoid with and without the cooling rods is shown in Figure 3.4.

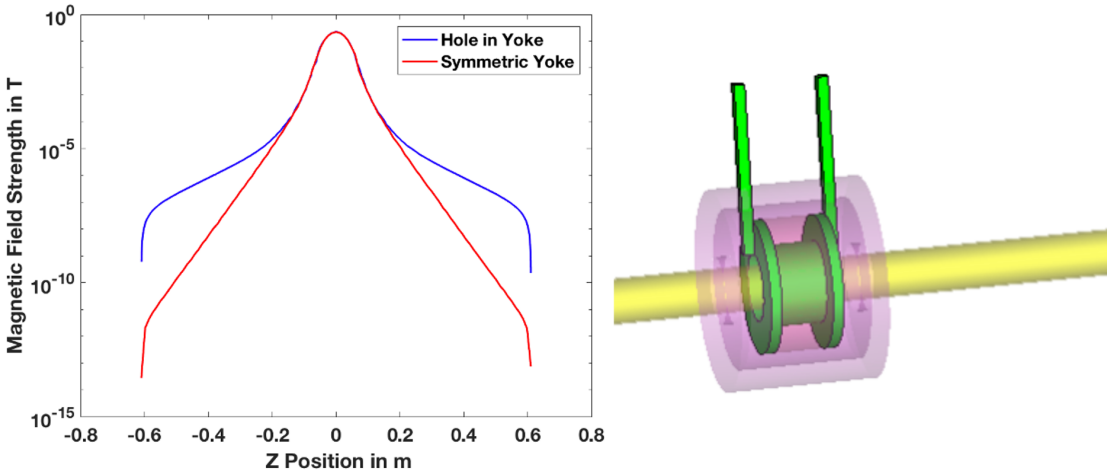

Figure 3.4: Left: The magnetic field magnitude at the center of the beam pipe as a function of the z position in the beam pipe. The solenoid is located at $z = 0$, the end of the gun cavity is at $z = -0.25$ and the cathode is at $z = -0.5$. Right: The 3D model of the KEK solenoid in CST with the cooling rods inserted.

I next investigated the dimensions of the iron yoke that will go around the coils to provide magnetic shielding to minimize the solenoid fringe fields. I kept the solenoid length constant at 38 mm for the yoke investigations. To start, in order to showcase the importance of the yoke with the 2D model, I started with no iron yoke. The magnetic field lines and axial field plot for a magnet with no yoke are shown in Figure 3.6. Next, I added an iron yoke to compare the effect. The iron yoke has a high magnetic susceptibility that provides a preferred path, relative to air, for the magnetic field, minimizing the fringe solenoid field strength. A pictorial demonstration of how the magnetic field changes with the addition of yoke is shown in Figure 3.5. Figure 3.6 compares the axial magnetic field between a simulation with and without a yoke and shows how the fringe fields decay much faster when an iron yoke is included in the design.

Lastly, I changed the dimensions of the yoke edge thickness, TE, and the cylinder wall thickness, TB, in 5 mm increments between 5 mm and 15 mm. The TB and TE dimensions are defined pictorially in Figure 3.3. The full iron yoke

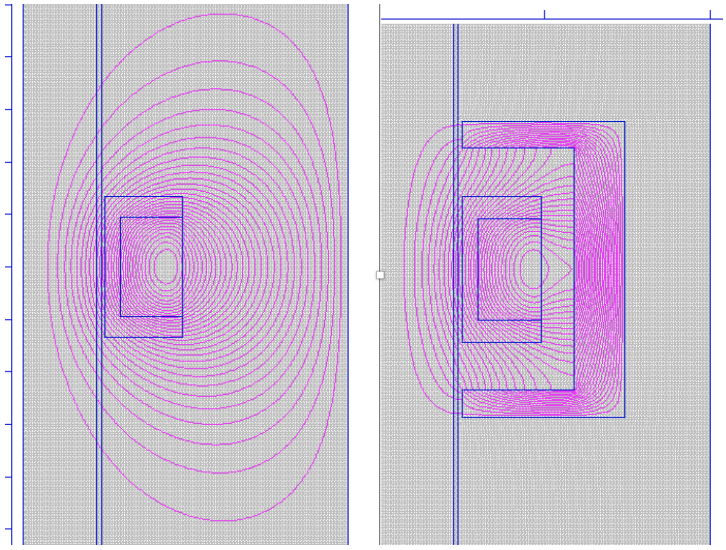

Figure 3.5: The field line comparison between using an iron yoke and not using a yoke.The left most image is a 2D slice of the coils and bobbin where the right image adds the iron yoke. Both images show magnetic field lines that result from current moving out of the page in the coil section of the magnet. Note that in this figure, the direction of the beam is vertical on the page.

dimension study done with the 3D solenoid model is shown in Table 3.4. While thicker dimensions of the yoke minimized the magnetic field at the cathode and gun exit locations, less yoke material is desirable to minimize the material that had to be cooled to cryogenic temperatures. Technically, all yoke dimensions met the magnetic field design requirements so we opted to go with less yoke material despite the slightly higher magnetic field results. After consulting with engineers, the 5mm iron yoke dimension was deemed too thin for good structural integrity so we decided to go with $TB = 10mm$, $TE = 10mm$.

After deciding the yoke dimensions, I looked at how the solenoid radius impacted our parameters of interest. We were limited to a solenoid radius no less than 25mm by the cryomodule beam pipe design. The summary of the solenoid parameters at various radii is shown in Table 3.5. To compare results, the maximum solenoid field was scaled to keep the focusing at 100 mm for each option.

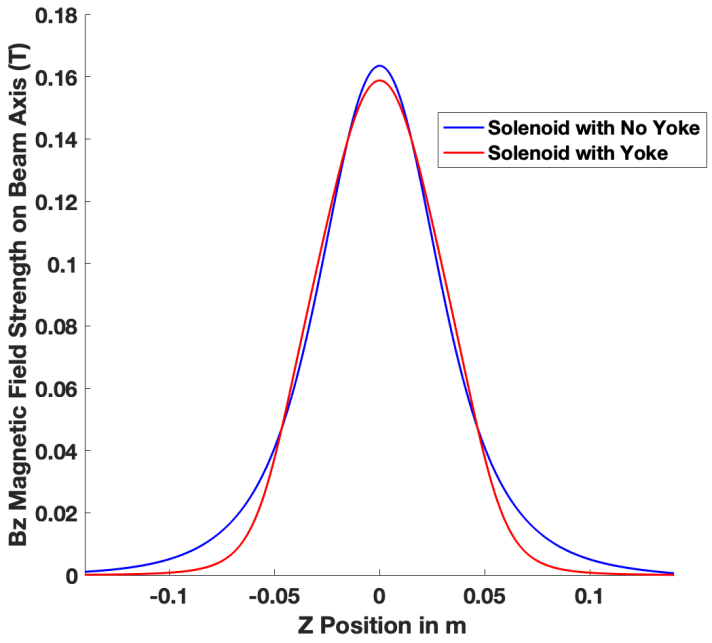

Figure 3.6: The plot compares the B_z field component on the beam axis for the solenoid with and without the iron yoke. Note that the axial fields fall off much faster when the yoke is used, which is critical for the design of an SRF gun.

TB mm	**TE** mm	**B, Gun Exit** Gauss	**B, Cathode** mGauss	**Max B, Z axis** T	**Max B, Yoke** T
15	10	0.07	2.9	0.226	0.3
10	**10**	**0.08**	**3.4**	**0.227**	**0.4**
5	10	0.09	4.0	0.224	0.7
15	5	0.11	4.6	0.223	0.5
10	5	0.11	5.2	0.222	0.5
5	5	0.14	6.0	0.223	0.7

Table 3.4: The summary of the study to change the the solenoid yoke dimensions. The TB and TE dimensions are pictorially defined in Figure 3.3. We chose to go with $TB = 10$ mm, $TE = 10$ mm to minimize the field on the cathode but still have an acceptable B field in the Iron yoke. 5mm was deemed too thin for structural integrity.

Radius mm	**B, Gun Exit** Gauss	**B, Cathode** mGauss	**Max B, Z axis** T
25	**0.075**	**4.1**	**0.228**
30	0.150	7.8	0.214
35	0.274	13.0	0.214

Table 3.5: Study results to see the impact of the solenoid radius on the magnetic field at the cathode and gun cavity. We ultimately selected to the solenoid as close to the beam pipe as possible.

The magnetic field simulated at the cathode and gun exit decreased as the radius of the solenoid radius decreased. Therefore, we ultimately chose to have the solenoid windings as close to the beam pipe as possible.

After all the solenoid dimensions were determined, the last parameter to check was if the solenoid would stay sufficiently below the 8K cooling requirement to ensure the niobium titanium wire of the solenoid would become superconducting. The solenoid will be inside a cryomodule, in vacuum, with an 80 K thermal shield between the cryomodule interior and outer world. The goal of the thermal simulations was to determine if more thermal shielding would be needed to keep the solenoid sufficiently cool.

I used a software package, ANSYS, to model the thermal effects for our proposed conduction cooling scheme. The thermal load on the solenoid was simulated from the 80K heat radiation from inside the cryomodule as well as from surface to surface radiation between the beam pipe and the solenoid. I looked at both aluminum rods and bobbin versus copper rods and bobbin and assumed the ends of the conduction cooling rods connected to a 4K liquid helium bath. The thermal model is shown in Figure 3.7 with the maximum recorded temperature in the coil recorded in Table 3.6. Both copper and aluminum materials provided sufficient thermal margin. These simulations indicated that we do not need to provide extra thermal shielding in addition to the 80K thermal shield. We ultimately chose to

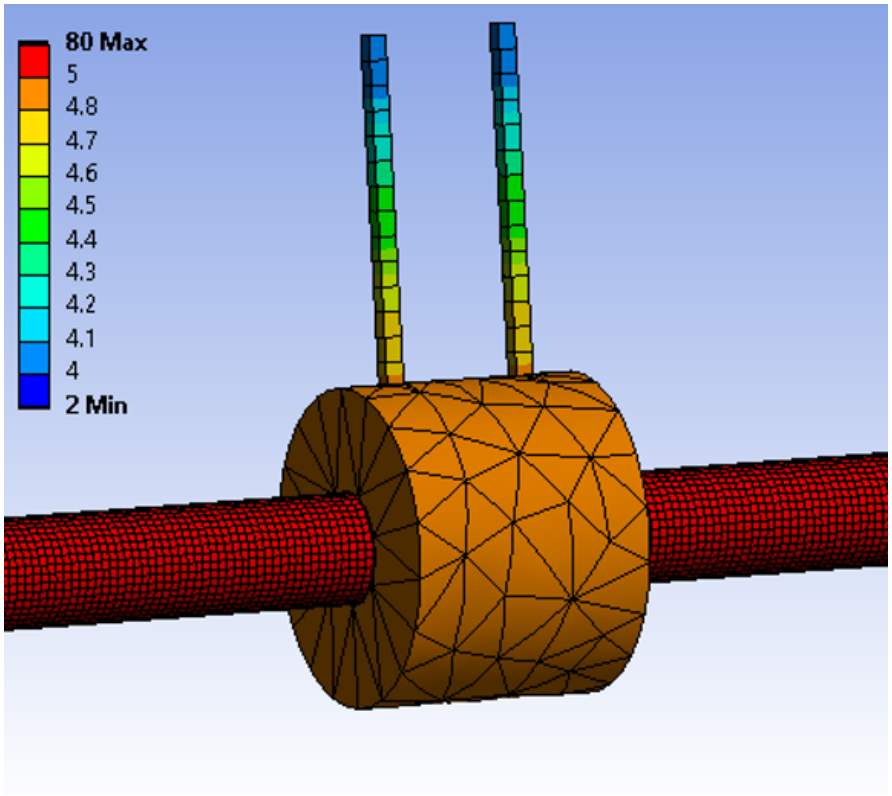

Figure 3.7: The thermal simulations of solenoid from the ANSYS simulation package. The ends of the rods were held at 4K. The heat flow into the solenoid was simulated from 80K heat radiation from the inside of the cryomodule as well as surface to surface radiation from the beam pipe. No heat is dissipated from the solenoid as the solenoid wires are superconducting.

go with an aluminum alloy with similar thermal material properties to aluminum as KEK engineers had used the material as superconducting magnet bobbins in the past.

Scenario	Max Coil Temp K
Aluminum Rods and Bobbin	5.04 K
Copper Rods and Bobbin	4.65 K

Table 3.6: The thermal comparisons between using copper versus aluminum for the bobbin and rod material.

To wrap up all of the design studies, we were able to find and simulate a design that met all the design requirements with the solenoid location at 0.5 m. The solenoid specifications are listed in Table 3.7 and a summary of the final performance parameters versus the design specification are displayed in Table 3.8.

Solenoid Parameter	Value
Length	38 mm
Radius	25 mm
Iron Yoke Edge Thickness	10 mm
Yoke Cylinder Thickness	10 mm
Wire Material	NbTi
Bobbin and Rod Material	Al Alloy

Table 3.7: The final selected solenoid parameters.

Parameter	Requirement	Simulated Value
Max magnetic field in Iron	1 T	0.4 T
Max magnetic field at edge of gun cavity	0.5 G	0.1 G
Max magnetic field at cathode (0 m)	10 mG	4 mG
Max temperature of solenoid wire coil	8 K	5 K

Table 3.8: The final simulated design metrics against the original design specification.

3.3.1 Asymmetrical Solenoid Implication Study

A big concern with the solenoid conduction cooling system was how inserting the rods through the iron yoke would impact the magnetic field as particles deviated from the center z axis. The concern was two fold: Firstly, could there be non-symmetrical field effects that could negatively impact the beam emittance. Secondly, the electron particle tracking simulation software ASTRA (the simulation tool used heavily in Chapter Two) takes in 2D axial field files of z position versus axial field magnitude and extrapolates off-axis fields assuming cylindrical symmetry. We wanted to make sure any future ASTRA simulations with a generated axial field file would still be a valid approximation. These concerns motivated a study to look at the off axis field perturbation to see if the insertion of the rods appreciably broke symmetry, changing the expected transverse magnetic component as we moved away from the center z axis.

The derivations of the expected transverse field components as we move away from the axis of symmetry, assuming cylindrical symmetry, is done in detail in Appendix B. To summarize from Appendix B, on the beam axis we expect no radial magnetic field. However as we move away from the beam axis, we expect, to first order, the radial field component to change at a specific z' location as:

$$B_r(r) = -\left(\frac{1}{2}\frac{dB_o}{dz}\bigg|_{z=z'}\right) r + O(r^3)... \tag{3.2}$$

where $B_o(z)$ is the magnetic field magnitude on axis, modeled to only have a longitudinal, $B_z(z)$, magnetic field component.

Our goal was to use the 3D CST model that included the rod cooling system, pictured in Figure 3.4, and compare the 3D model outputs to the outputs we would expect if we had perfect cylindrical symmetry to see if there was an appreciable difference. To do this, we recorded the transverse magnetic field component of the

solenoid as a function of z at x displacements of 0, 1 and 2 mm. Results are shown in Figure 3.8. Next, we looked at the z location with the maximum transverse magnetic field when estimated off axis, $z = 35$ mm. $z = 35$ mm is the edge location of the solenoid yoke. At $z = 35$ mm, I used CST to estimate the magnetic field at various displacement offset away from the center axis and recorded the respective field component. For example, if I displaced in x, I would record the magnitude of the B_x field. This was a fast way to compare the radial magnetic field component at two different ϕ values, 0 and $\pi/2$. Figure 3.9 demonstrates that the radial fields modeled in CST are very similar at the two different ϕ values which implies that the inclusion of the rods did not break symmetry and make the radial magnetic field ϕ dependent. Additionally, both the slope from theory (Eq. 3.2) and the calculated slope of the lines in Figure 3.9 match at 0.0022 T/mm. I took from this result that, even with the rods inserted, we can still assume cylindrical symmetry is sufficiently intact.

3.3.2 Solenoid Emittance Contribution Study

With a larger goal of reducing the emittance contributions from electron injector system in mind, for completeness I wanted to investigate the expected emittance contribution I could expect as the beam went through the solenoid. The solenoid adds emittance to the beam in two ways: chromatic and geometric aberration emittance contributions. Chromatic emittance growth occurs when there is an energy spread in the beam and arises from the different focal length electrons of different energy will have. The chromatic emittance is highly dependent on the energy spread of the incoming beam out of the injector so we chose to not model this with a stand alone solenoid and instead let the multi-objective genetic algorithm simulations detailed in Chapter Two investigate this multivariable

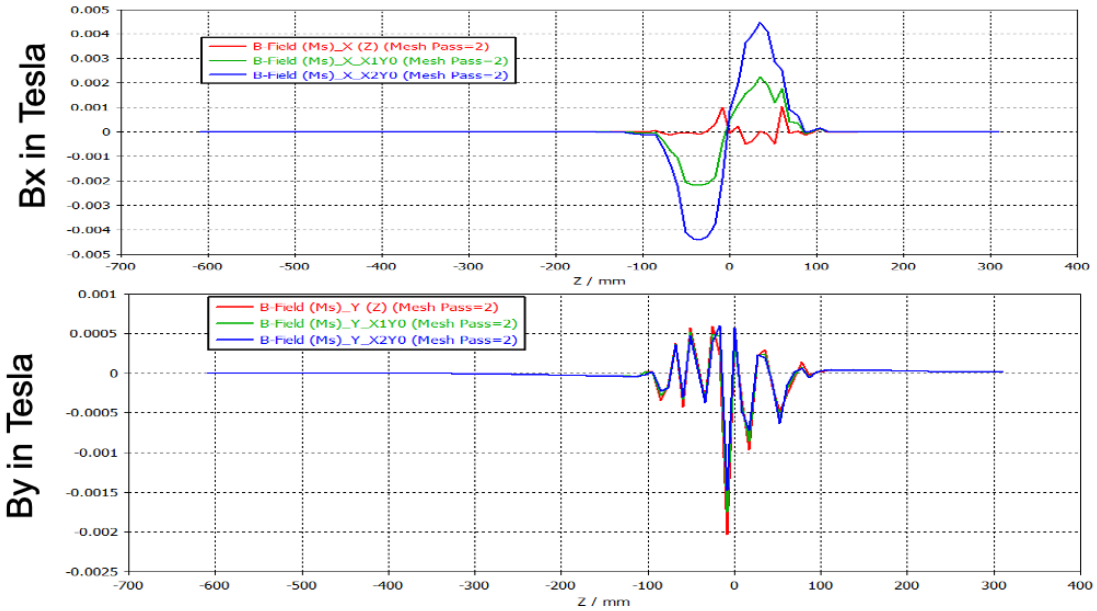

Figure 3.8: The impact of the transverse magnetic fields as we venture away from the center z axis in the 3D CST solenoid model. Red = magnetic field through center. Green = magnetic field through a 1 mm x offset. Blue = magnetic field with a 2 mm x offset. The top plot is showing the B_x magnitude while the bottom plot shows the B_y magnitude for an x offset. Since the perturbation is in the x direction, B_x sees a change that is approximated by Eq. 3.2.

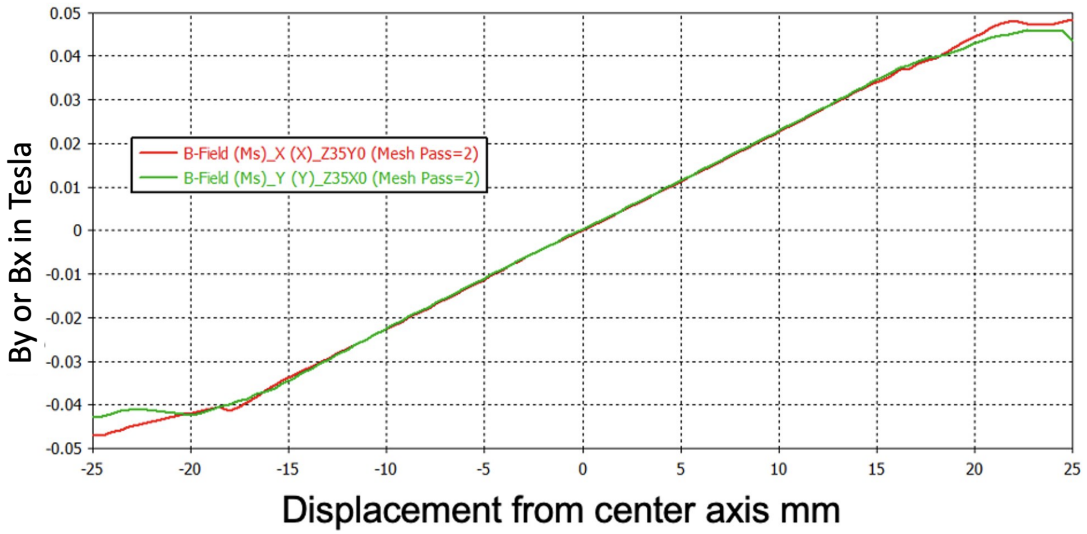

Figure 3.9: Red = $B_x(x)$ at $z = 35mm$, $y = 0$ mm. Green = $B_y(y)$ at $z = 35$ mm, $x = 0$ mm. The red and green lines show the radial field components at two different ϕ values. The similarity motivates that cylindrical symmetry is intact.

dependent emittance trade-off.

The geometric aberration emittance arises from the transverse field contributions that are introduced as we move away from the axis of cylindrical symmetry. These field perturbations are described in Eq. 3.2. However, the aberrations from non-linear off-axis fields are not the only contributor to the expected emittance growth and the current way to calculate the expected geometric aberration emittance growth is to do so numerically in order to take into account beam dynamic effects. Investigating the geometric emittance provide a useful visual representation of how the spot size going into the solenoid relates to the outgoing geometric emittance. To isolate the geometric emittance of the solenoid, I set up an idealized study with the ASTRA particle tracking software. I simulated a perfect 2 MeV cylindrically uniform beam with no initial angular divergence (the famous "Beer Can" beam approximation) going though just the solenoid magnet. For this simulation study, we ignored space charge effects. These steps ensure there is no initial emittance in the beam and no emittance growth from space charge effect, effectively isolating any emittance growth to the solenoid. For a focus of 200 mm, I measured the beam emittance of this beer can beam as it moved through the solenoid. The results of the ASTRA simulation for the size and emittance of the beam as a function of longitudinal position into and through the solenoid is shown in Figure 3.10.

I then simulated the same perfect Beer Can beam through solenoid field files of varying solenoid radii, scaling the field to maintain the same focus. The beam spot size was also kept constant for each radius step point. The result is show in Figure 3.11. The plots indicate that at a sufficient longitudinal location where the solenoid fields are negligible, the emittance of the various solenoids converge to an identical value. This result demonstrates a noteworthy takeaway from this study:

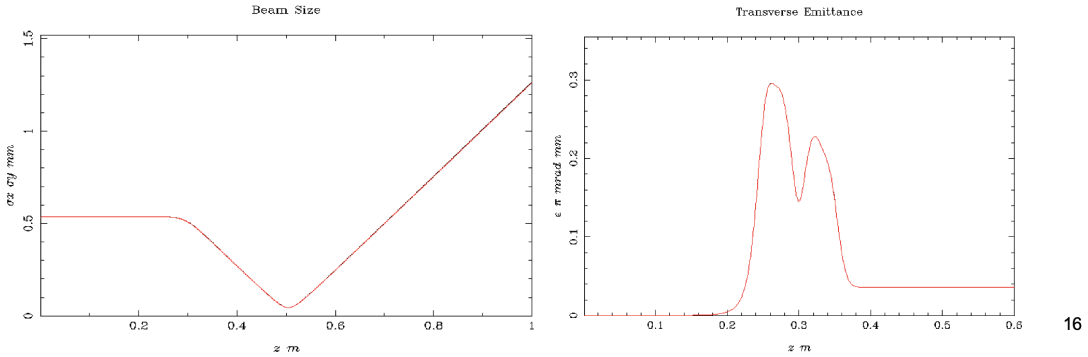

Figure 3.10: We put a solenoid centered at 0.3 meters in an ASTRA lattice. We then tracked a 2 MeV beam through the solenoid field, ignoring space charge effects. The beam started as a cylindrically uniform beam with no initial transverse or longitudinal energy spread. The left image shows the beam rms beam size versus z position. The right image shows the emittance versus z position. The remaining emittance on the right-hand side, after $z = 0.4$ m , is the geometric emittance contribution of the solenoid.

as long as the focus and incoming spot size were kept the same, the expected geometric emittance contribution was constant for differing solenoid fields.

Lastly, to close out the expected geometric emittance study, I mapped the expected solenoid geometric emittance growth as the beam size increases. As a point of general interest, it is of interest to show the dependance of the emittance on the initial radius from an initially zero emittance beam. This physics was in the simulation effort done in Chapter Two and this study develops intuition for how the emittance scales.

The relation of emittance versus initial RMS beam size is shown in Figure 3.12. I fitted the final emittance to the polynomial of best fit to show that we expect an emittance growth on the order of $\propto 0.0049\sigma^4$, where σ is the incoming RMS beam size. This plot isolates one type of emittance contribution of one component in an injector lattice. In isolation, this plot would motivate that an incoming beam spot size be as small as possible. However, as a reminder from Section 1.4, the solenoid is just one of many injector components that grow the emittance. Figure

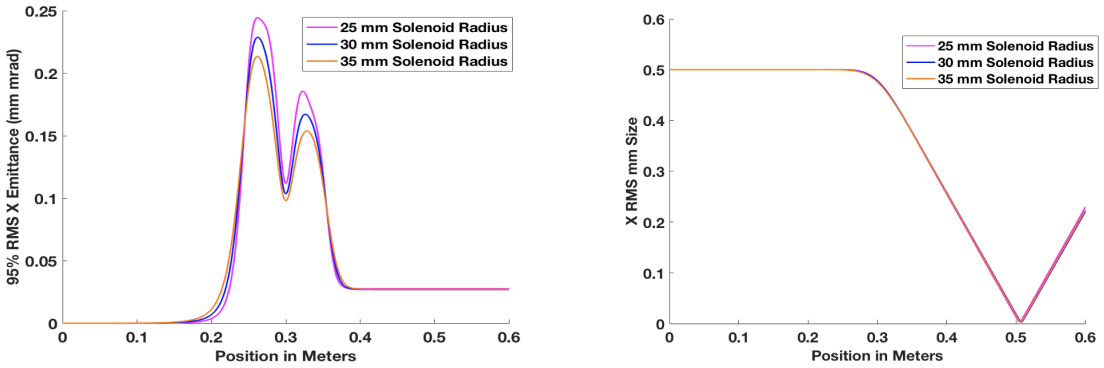

Figure 3.11: The emittance comparison difference between the same 2 MeV perfect beer can beam going through solenoids with various radii. The current going through the solenoid was changed to maintain a 200 mm focus.

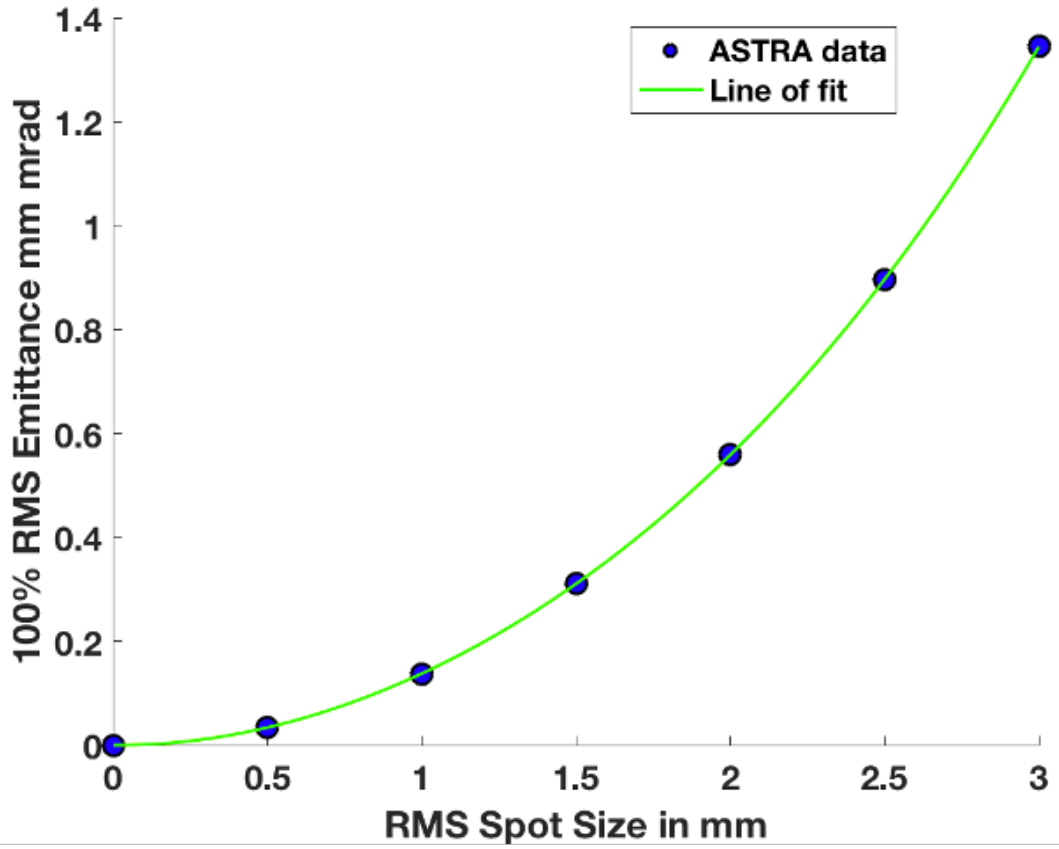

Figure 3.12: The expected geometric emittance growth of a 2MeV beam at various starting beam spot sizes as the beam goes through the proposed KEK solenoid design.

3.12 demonstrates that an incoming smaller spot size is advantageous to minimize emittance growth from the solenoid but the emittance growth from space charge effects or the RF cavities would have a different relationship of emittance versus spot size. While it is interesting to see the expected geometric emittance growth from the solenoid for various spot sizes, the genetic algorithms simulations that are detailed in Chapter Two are still needed to determine the ideal spot size through the solenoid that minimizes the emittance effects from all the emittance contributors described in Section 1.4.

3.4 Solenoid Manufacturing and Measure Results

Once we locked in the design, KEK engineers ordered the bobbin and wire components for the solenoid. KEK had an existing setup to wind magnets that was similar to and elongated spinning wheel. I hand-wound the solenoid at KEK with 1,728 turns and 32 layers over a two day period. The finished solenoid is shown in Figure 3.13. When I departed KEK in March 2020, the solenoid was scheduled to be filled with epoxy to solidify the coil positions. Additionally, KEK staff manufactured and connected the iron yoke and the aluminum alloy rod thermal connection, shown in Figure 3.14.

In November 2021, KEK staff led by my KEK mentor, Taro Konomi, installed the solenoid into a test cryostat to measure the field profile of the solenoid at cryo-temperatures. The solenoid test setup is shown in Figure 3.15. KEK staff used a 3D Hall probe that moved and measured the magnetic field along the beam axis.

The comparison between the measured and simulated field shapes is shown

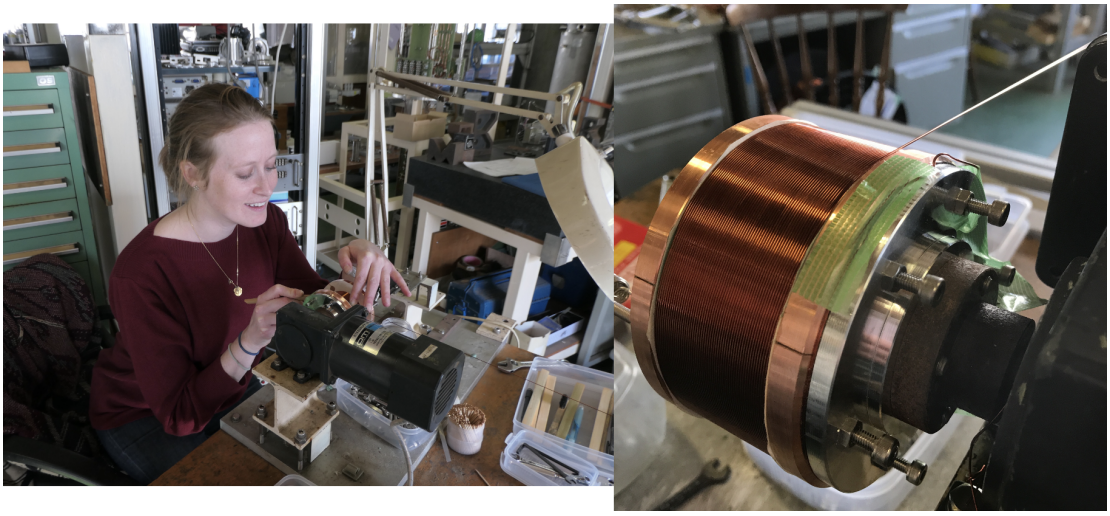

Figure 3.13: Left: The author winding her solenoid magnet. Right: The KEK Solenoid after winding is complete.

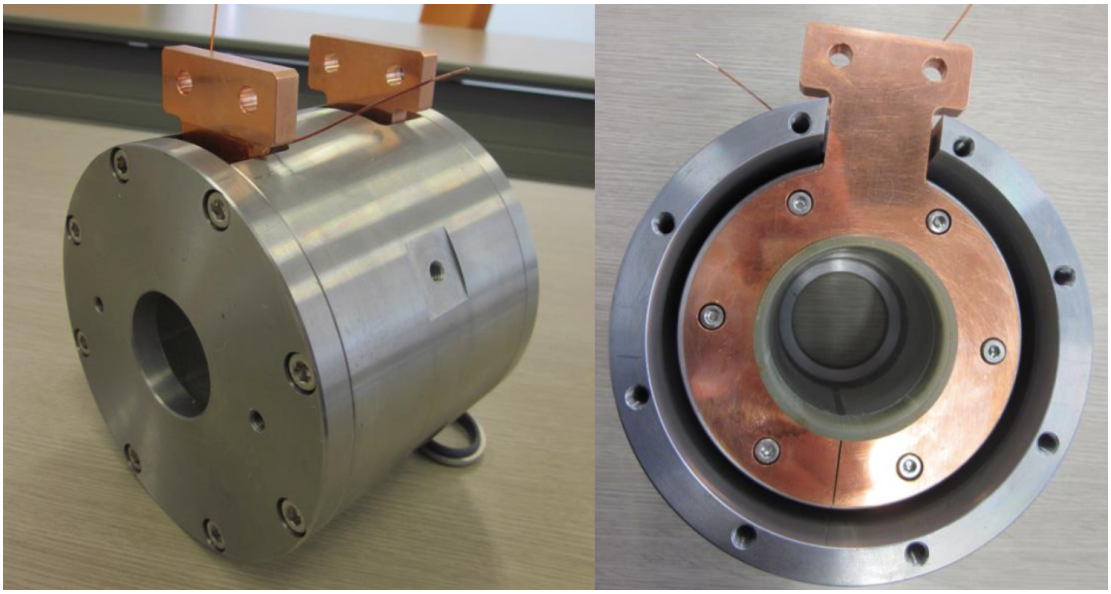

Figure 3.14: The KEK Solenoid in the iron yoke with the rods that will act as the thermal connection to perform conduction cooling.

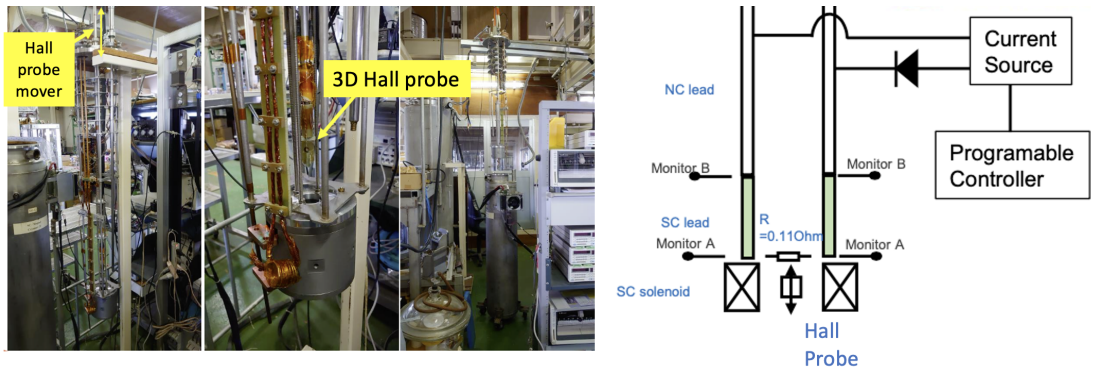

Figure 3.15: The solenoid test setup at KEK. Images curtesy of Taro Konomi.

in Figure 3.16 with the field maximums scaled to one to easily compare. The measured field profile agrees well with the simulated solenoid field file but the measured field is offset by a non-physical negative magnetic field strength. The Hall probe measured a minimum voltage reading of -0.07 mV at the solenoid edge readings that corresponded to a magnetic field of -0.1 kG. Taro Konomi estimates that sources of measurement error come from a variety of sources: The Hall probe only has a readout precision of ± 0.01 mV and had an operational current that had a 5% error margin. We believe these probe factors can satisfactorily explain the -0.07 mV reading at the edge of the solenoid. Additional sources of error include the current source that drove the solenoid coil had a value error of $\pm 3.5\%$. There was a small fabrication error (< 0.1 mm) in the gap of the iron yoke. Lastly, a protective resistor of 0.11 Ohm was installed during the test that was not included in the simulations. In total, the error was estimated to be 10% and sufficiently explains the mismatch between the simulated and measured field files.

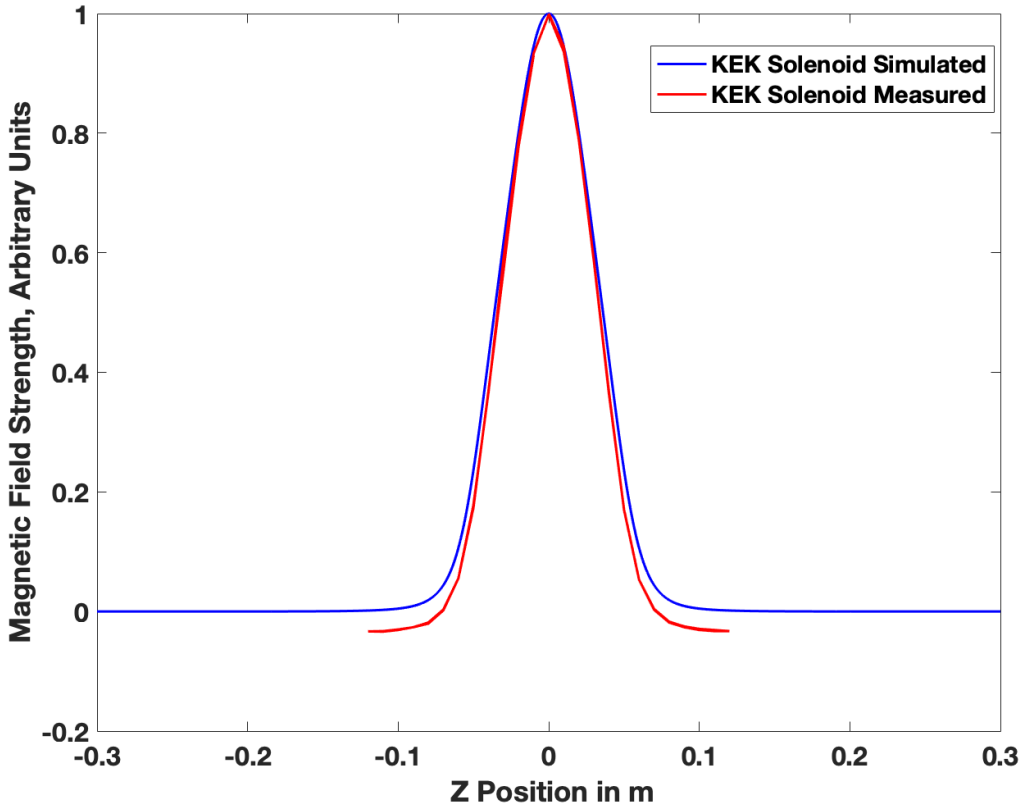

Figure 3.16: The KEK solenoid field profile comparison between measured (red) and simulated (blue) with the center of the solenoid centered around 0 m. The shape of the solenoid fields match well with a noticeable exception the non-physical negative magnetic field measured at the edges of the solenoid. This error is believed to be due to error from the Hall probe.

3.5 Impact of Measured Solenoid Field on Simulation Results

Chapter Two describes a large body of simulation work to optimize injector systems with various gun cavities and layouts. In that previous simulation work, the KEK solenoid, described in an earlier section of this chapter, had not been simulated or made yet. I had access to the Wisconsin FEL (WiFEL) solenoid field file that was developed for a test lattice for a quarter cell SRF gun cavity at the University of Wisconsin Madison. Thus, I used the WiFEL solenoid field file with the original KEK gun simulation lattice in the studies of Chapter Two. With the simulated and measured field result of the KEK solenoid now in hand, I wanted to investigate how sensitive the simulation work described in Chapter Two is to using an entirely different solenoid. If this different solenoid file had an appreciable impact on the Pareto Fronts from Chapter Two, it could potentially motivate a rerun of the KEK lattice simulations to establish a new baseline capability with this new solenoid, substituted for the WiFEL solenoid. This would necessitate a time-intensive reoptimization to adjust lattice parameters. In particular, I wanted to investigate the impact to the Pareto Fronts when I used a measured, instead of simulated, solenoid field file. The WiFEL solenoid field is compared to both the simulated and measured KEK solenoid fields in Figure 3.17.

The first study I did was to see the impact to a Pareto Front if I changed the WiFEL solenoid file to the simulated KEK solenoid field file. This swap took a little care to ensure that it was a fair comparison. The multi-objective genetic algorithm used in Chapter Two optimized the solenoid with the maximum field strength parameter and then would scale the solenoid field file to the selected maximum field. Figure 3.17 shows the significant differences between the WiFEL

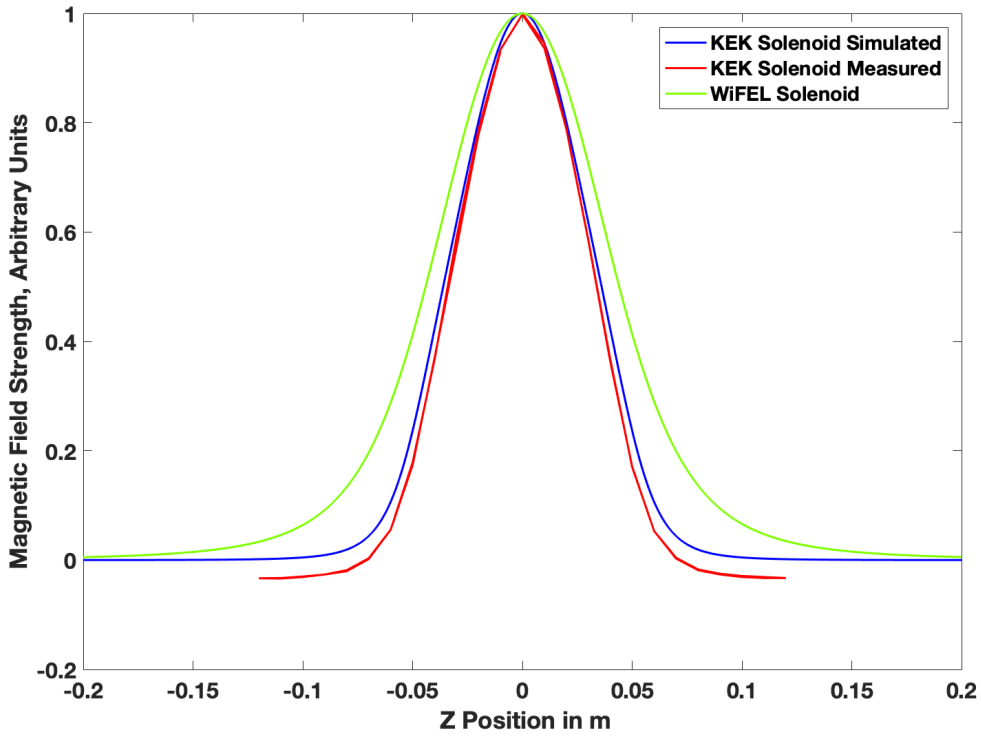

Figure 3.17: The KEK solenoid measured (red) and simulated (blue) field files compared with the WiFEL (green) field file.

and KEK solenoid fields scaled to the same maximum. A primary mission of the solenoid is to counter the defocusing effect of the gun cavity. The amount of focusing the solenoid performs varies as the integral of $|B^2|$ over the entirety of the solenoid field. Thus, the KEK solenoid would give a lower focusing effect than the WiFEL solenoid for the same maximum field strength. In order to compare the Pareto Front impact between two different solenoids with different field shapes, I took the optimized WiFEL solenoid maximum field parameter from a Pareto Front and calculated the focus from the magnetic field using Eq 3.1. I then determined the maximum field strength the KEK simulated field file needed to have to give the same focus as with the WiFEL solenoid. I input that new solenoid maximum field parameter as the optimized parameter with the KEK solenoid and reran the front. The Pareto Front comparison is shown in Figure 3.18. With the simulated solenoid files, we were able to closely reproduce the simulation results despite using a solenoid with a different field shape. The evolution of the emittance versus the z position is shown in Figure 3.19. While the emittance does differ while the beam is traveling through the solenoid, the emittance evolution matches for the rest of the lattice when the focusing is matched. Therefore, the end lattice parameters, such as emittance and bunch length, were not significantly changed between lattices that used the WiFEL solenoid versus the KEK solenoid.

I followed the exact same protocol with the measured KEK solenoid file but the Pareto Front did not reproduce satisfactorily. The Pareto Front comparison is shown in Figure 3.20. Figure 3.20 appears to show that there is significant degradation to the end emittance when a measured field file is used in the lattice. This was surprising as the measured and simulated field values were very similar. Undeterred and motivated by the stellar Pareto Front reproductions with the simulated KEK solenoid file, I investigated a few options to address the poor

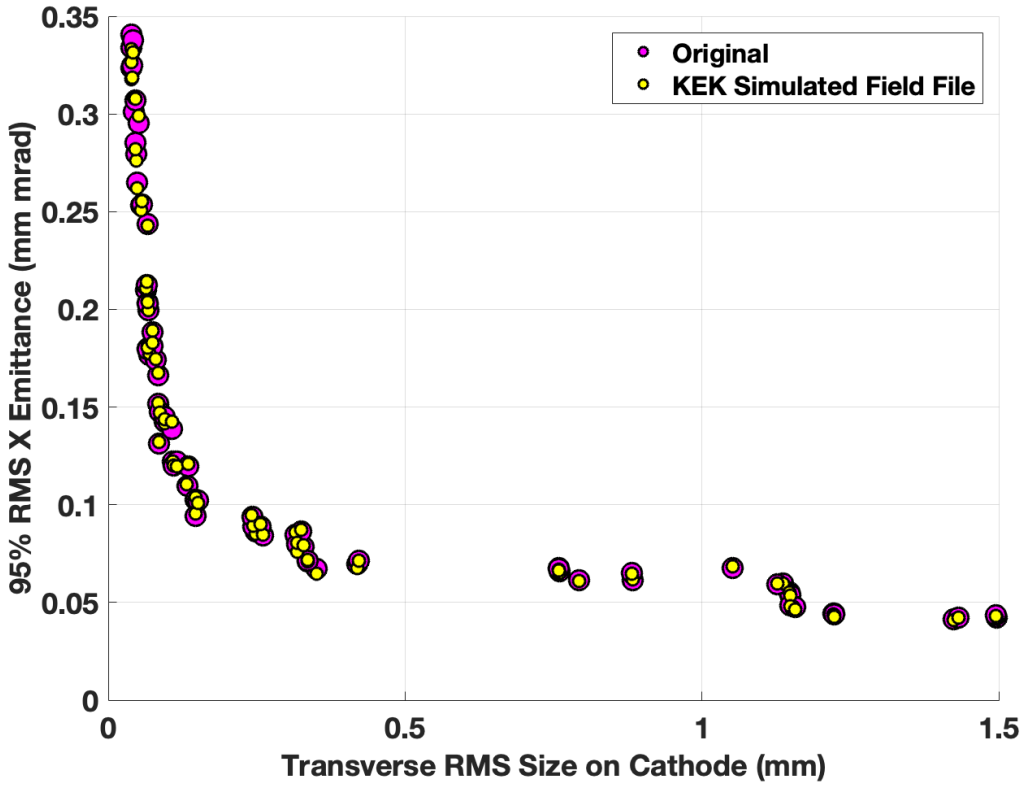

Figure 3.18: The Pareto Front comparison between using the simulated KEK solenoid file (yellow) and the WiFEL solenoid field file (pink) used in the simulation results in Chapter Two. The solenoid fields were normalized to maintain the same focus with the optimized lattice.

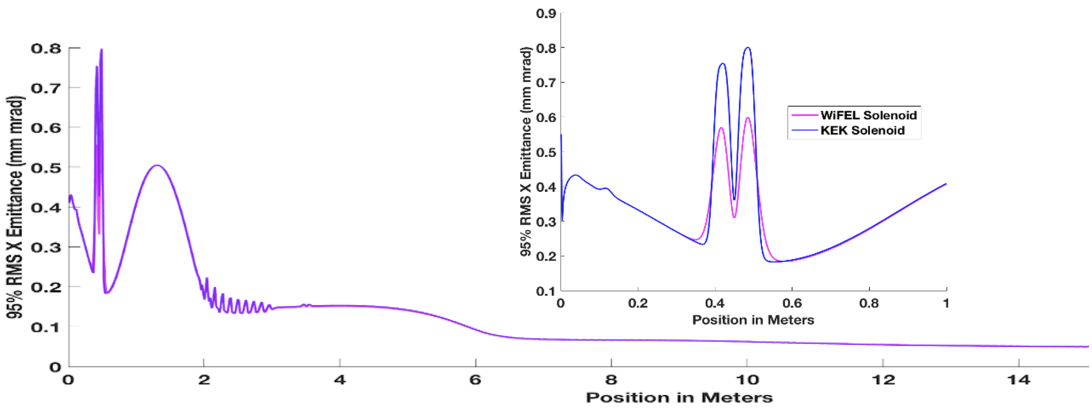

Figure 3.19: The emittance versus position comparison of an optimized KEK lattice with the WiFEL solenoid (Pink) and the KEK simulated solenoid field (Blue/Purple) with the solenoid focus matched. Despite a different projected emittance response in the solenoid, the emittance out of the two different solenoids match up and the end lattice emittance is unchanged.

Pareto Front reproduction.

The first idea was to assess if the non-physical negative solenoid field values shown for the measured solenoid file in Figure 3.17 significantly impacted the Pareto Front. I shifted up the measured solenoid field file by +0.1 gauss to set the minimum field value to zero and eliminate the non-physical negative magnetic field. The rerun Pareto Front was similar to the Pareto Front generated with the unshifted measured solenoid field, indicating the negative pedestal had no appreciable impact.

The next concerning item from the measured solenoid field was the coarseness of the data. There were only 25 points measured for the solenoid field after averaging for duplicate points. To improve the field file fidelity, I next fit the data to a 12th order polynomial. The data points along with the polynomial of best fit is shown in Figure 3.21. The Pareto Front was rerun and this time the Pareto Front did reproduce. The Pareto Front comparisons between the measured data with

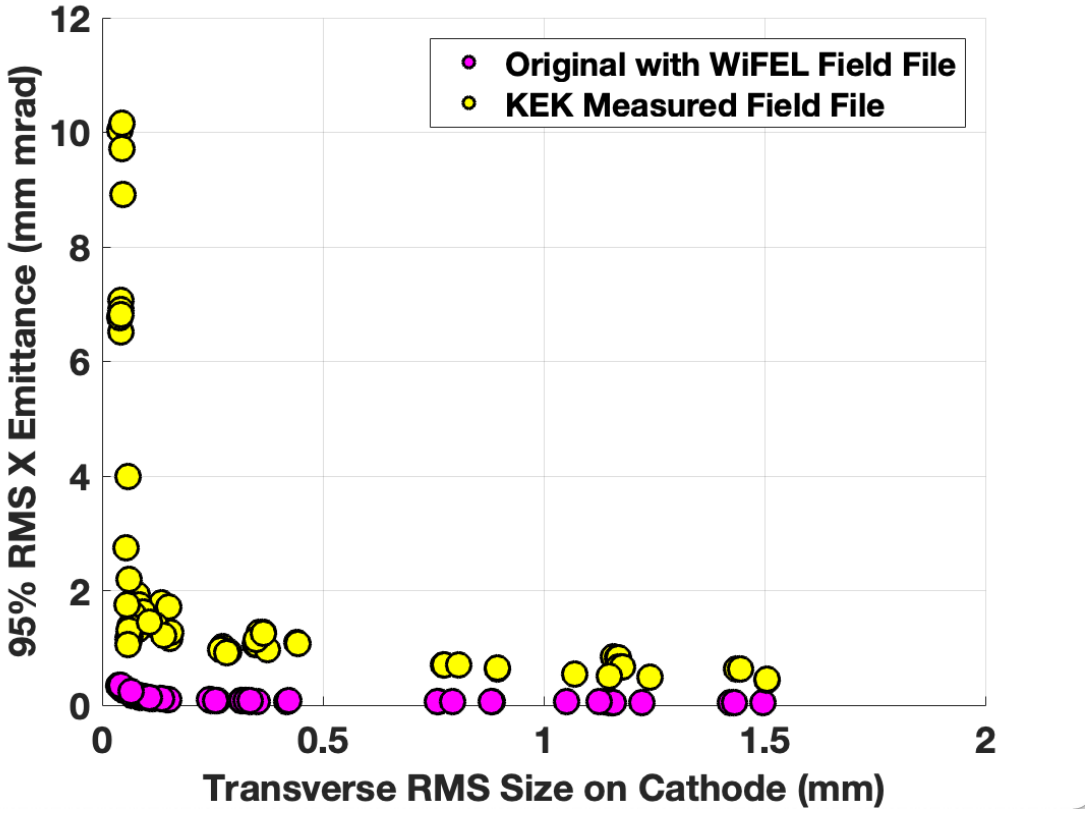

Figure 3.20: The Pareto Front comparison between using the measured KEK solenoid file (yellow) and the WiFEL solenoid field file (pink) used in the simulation results in Chapter Two. The solenoid fields were normalized to maintain the same focus with the optimized lattice.

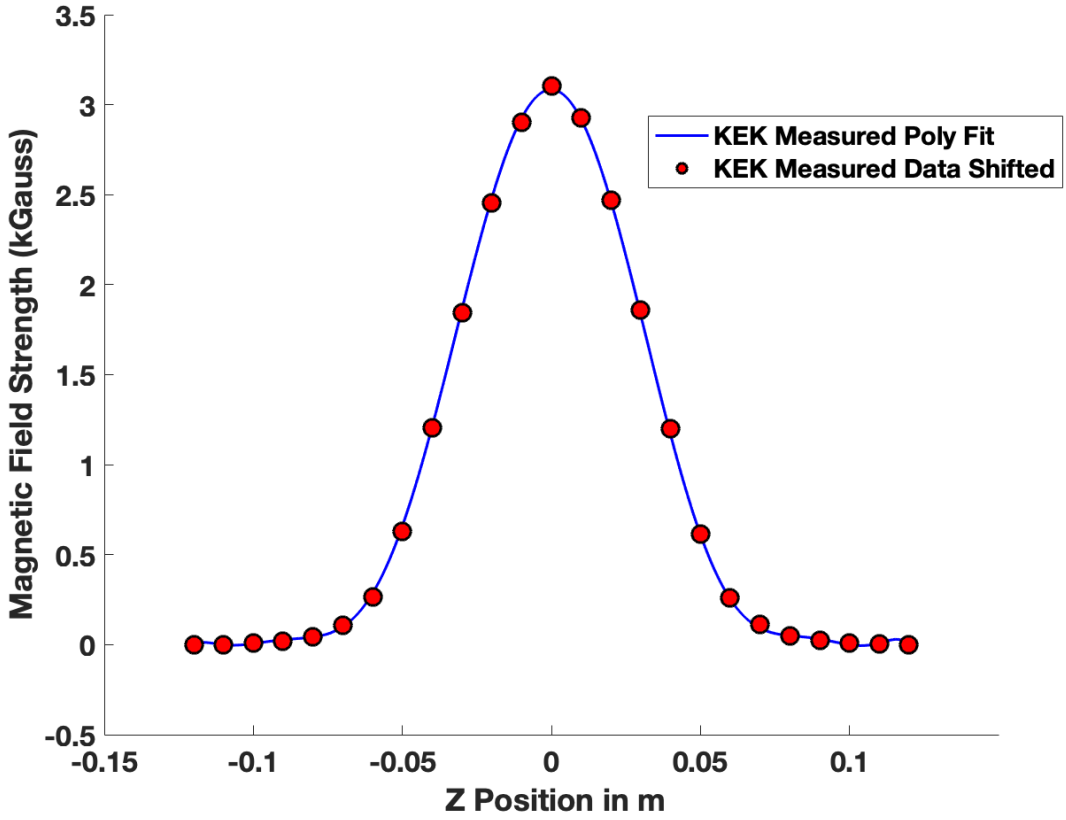

Figure 3.21: The measured magnetic field data versus the polynomial fit used to increase the number of points from 25 to 1000.

increased fidelity and the original WiFEL lattice is shown in Figure 3.22. We can conclude that 25 data points was insufficient for the particle tracking simulation tool, ASTRA and that ASTRA was incorrectly interpolating the expected field between the relatively sparse data measurements.

In summary, the simulations described here in Chapter Three confirm that the physical solenoid provided performance acceptably close to that of an ideally designed solenoid.This confirms the suitability of the solenoid design and build work described in this chapter for use in a Superconducting RF gun source R&D and commissioning.

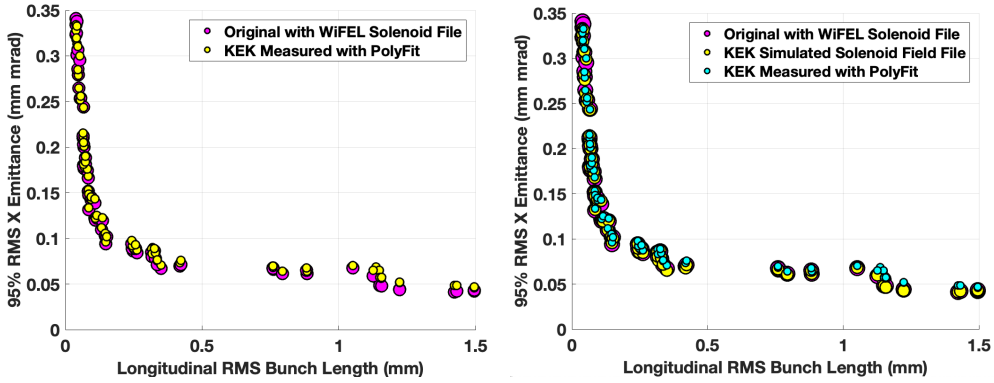

Figure 3.22: The final comparison plots showing the susceptibility to measured data. The left plot shows just the Pareto Front comparison between the original simulation run and the fitted measured data. The right plot compares the original, KEK simulated solenoid file and the KEK fitted measured data.

Chapter 4

Conclusion

The work described in this dissertation helps to clarify the direction of how to advance and improve electron photoinjectors for high repetition rate machines. We started this research by identifying two promising areas of photoinjector research: improving the cathode quality and increasing the RF gradient in the gun cavity. In these research areas, I quantified how improvements should map to photoinjector figures of merit such as beam emittance, bunch length and energy spread. Additionally, I helped further develop superconducting RF technology by building a superconducting solenoid for an SRF gun cavity test stand.

In Chapter Two, I performed a simulation campaign that decouples cathode improvements from SRF gun cavity gradient improvements. I mapped out the expected change of the emittance at the end of the injector system for various quality of cathodes while still satisfying other key requirements to run a Free Electron Laser (FEL). I focused specifically on quantifying how cathode and gun improvements for the LCLS-II injector system would allow the LCLS-II injector to produce an electron beam with an emittance of 0.1 mm mrad at the end of the injector system. I demonstrated that if we only improved the cathode quality of the LCLS-II injector system, the LCLS-II would require a cathode that produced

an electron beam with 0.3 mm mrad/ mm rms spot size thermal emittance to meet the 0.1 mm mrad emittance goal. As a reminder from Chapter Two, the original thermal emittance estimate was 1 mm mrad/ mm rms with 0.75 mm mrad/ mm rms the current best measured result for the cesium telluride cathodes [33]. 0.3 mm mrad/mm rms would be a substantial improvement for cathode researchers. However, a higher gradient can help decrease the cathode quality requirement to achieve a similar end injector emittance. I demonstrated that with a quarter cell SRF gun cavity with a maximum gradient of 50 MV/m, we could ease the cathode quality requirement to 0.5 mm mrad/ mm rms, a still ambitious but more feasible goal. In summary, we need both cathode quality and gun cavity gradient improvements to meet the injector quality goals for the high repetition rate accelerator community.

In Chapter Three, I designed a solenoid magnet to go on a SRF gun cavity test stand that will help researchers gain experimental experience with SRF gun technology. I laid out the steps taken to design a solenoid that accommodates the unique requirements of a SRF gun cavity to have negligible magnetic fields reach the walls of the superconducting cavity. With operational test results done by KEK staff, I confirmed that the physical solenoid performance was within an acceptable range of the expected design performance. Currently, there are few superconducting solenoids used with superconducting gun cavities. KEK staff now has this solenoid to use with an SRF gun test stand in order to gain more operational experience with SRF gun technology.

4.1 Research Epilogue

The work done in this dissertation was largely performed in 2018 through 2019 which presents a unique opportunity to provide a 2022 epilogue with the benefit of

knowing the direction the field has taken three years on. In general, the electron photoinjector FEL community has taken steps to move in a research direction that aligns with the take aways from this dissertation's body of work to pursue both SRF and cathode research in parallel.

The LCLS-II High Energy Project submitted a conceptual design report (CDR) in March 2022 for a new Low Emittance Injector (LEI)[26]. The LEI will initially function as a SRF gun cavity development test stand but will be built next to the current LCLS-II injector so that the LEI can one day take over and provide the electron beam to the larger LCLS-II linac once emittance improvements are demonstrated.

The LEI CDR clearly states that the LCLS-II HE project team's strategy to lower injector emittance is to use both a higher gun cathode gradient and a cathode with a lower intrinsic emittance. To achieve the needed cathode improvements, the LCLS-II HE project is collaborating with SLAC National Lab to perform cathode R&D that looks at the following areas of study: the impact of multi-photon process, cathode roughness, field emission and temperature dependence. In parallel, Michigan State University is leading a collaboration to develop a new SRF quarter cell gun cavity, similar to the WiFEL gun cavity used in the simulation work in Chapter Two, that is expected to be the gun cavity for the LEI. This MSU SRF team includes previous KEK Physicist and mentor to this thesis writer, Taro Konomi. The LEI CDR anticipates the LEI project will go into 2030.

Appendix A

Calculating the Focus of a Solenoid

Questions: How much does a beam focus when it goes through a solenoid?

I am using the following assumptions:

- Ignoring space charge effects
- Cold beam approximation, ie initial transverse velocity is zero
- Cylindrical beam

With a long solenoid, the magnetic field in the center approaches a uniform field. However, interesting things happen at the edges that impact beam dynamics that I would like to determine. For a long solenoid with length L, I can approximate the field as a uniform B_z from $0 < z < L$. However we require $\nabla \cdot B = 0$ and $\nabla \times B = 0$ and there are beam dynamics effect that make it so I cannot ignore $\nabla \cdot B = 0$. Magnetic fields must form closed loops. Therefore there must be a radial component of the field at the edges.

I'm going to approximate the B_z field as a Heaviside function and then use delta functions for the B_r component at the edges.

$$\vec{B} = \left(\int_{-\infty}^{z} dz' B_o \delta(z') - B_o \delta(z' - L) \right) \hat{z} + \left(-A(r)\delta(z) + A(r)\delta(z - L) \right) \hat{r}$$

Now I get to determine $A(r)$ to make sure that we are not violating $\nabla \cdot B = 0$. In cylindrical coordinates this means

$$\frac{dB_r}{dr} + \frac{B_r}{r} + \frac{dB_z}{dz} = 0$$

$$-\frac{dA}{dr}\delta(z) + \frac{dA}{dr}\delta(z - L) - \frac{A\delta(z)}{r} + \frac{A\delta(z - L)}{r} + B_o\delta(z) - B_o\delta(z - L) = 0$$

Let's group by delta function!

$$\delta(z)\left(-\frac{dA}{dr} - \frac{A}{r} + B_o \right) + \delta(z - L)\left(\frac{dA}{dr} + \frac{A}{r} - B_o \right) = 0$$

This motivates that we need to solve the below ODE:

$$-\frac{dA}{dr} - \frac{A}{r} + B_o = 0$$

From inspection, we see that $A = \frac{B_o r}{2}$.

Ampere's law dictates that $\nabla \times B = 0$, or that $\frac{dB_z}{dr} = \frac{dB_r}{dz}$. This would require $\frac{dB_r}{dz} = 0$ but the derivatives of delta functions don't have beam dynamic repercussions so we are okay violating $\nabla \times B = 0$ for this exercise.

We have an approximated magnetic field that we can use to see how the beam responds!

$$\vec{B} = \left(\int_{-\infty}^{z} dz' B_o \delta(z') - B_o \delta(z' - L) \right) \hat{z} + \left(-\frac{B_o r}{2} \delta(z) + \frac{B_o r}{2} \delta(z - L) \right) \hat{r}$$

I will split up the beam into three areas: (I) the transverse delta function at $z = 0$, (II) the uniform B_o from $0 < z < L$, and (III) the transverse delta function at $z = L$. In region I, we only see the field $\frac{-B_o r}{2} \delta(z)$, so the effect on the beam is described as:

$$m\gamma \frac{d\vec{v}}{dt} = q \left(v_z \hat{z} \times \frac{-B_o r}{2} \delta(z) \hat{r} \right)$$

$$\frac{dv_\theta}{dt} \hat{\theta} = -\frac{q B_o r v_z \delta(z)}{2m\gamma} \hat{\theta}$$

$$v_\theta = \int_{-\epsilon}^{+\epsilon} \frac{-q B_o r \delta(z)}{2m\gamma} \frac{dz}{dt} dt$$

$$v_\theta = \frac{-q B_o r_o}{2m\gamma} = -\omega r_o$$

where $\omega = \frac{q B_o}{2m\gamma}$ and r_o is the radius of the particle at $z = 0$. We pick up an angular velocity when we go into the solenoid. Now we get to consider how the beam behaves in region II when we introduce a constant $B_o \hat{z}$ field component. At the beginning of region II, we have the following velocity vector:

$$\vec{v}(z = 0) = -\omega r_o \hat{\theta} + v_z \hat{z}$$

I want to solve the equations of motion in the solenoid with cylindrical coordinates because then I can exploit the theorem that in an axially symmetric field, $\dot{\theta}$ is constant and equals my calculated ω.

I need to remember a few things about dealing with cylindrical coordinates that I will document here. The tricky part about cylindrical coordinates is that the unit vectors move in time. We can start with the unit vectors as reflected in cartesian coordinates since those do not change in time...

$$\hat{r} = cos(\theta)\hat{x} + sin(\theta)\hat{y}$$

$$\hat{\theta} = -sin(\theta)\hat{x} + cos(\theta)\hat{y}$$

Now let's take time derivatives and see that happens!

$$\dot{\hat{r}} = -\dot{\theta}sin(\theta)\hat{x} + \dot{\theta}cos(\theta)\hat{y}$$

$$\dot{\hat{\theta}} = -\dot{\theta}cos(\theta)\hat{x} - \dot{\theta}sin(\theta)\hat{y}$$

$$\dot{\hat{r}} = \dot{\theta}\hat{\theta}$$

$$\dot{\hat{\theta}} = -\dot{\theta}\hat{r}$$

Another useful thing is to make the position, velocity and acceleration vectors in cylindrical coordinates

$$\vec{x} = r\hat{r} + z\hat{z}$$

$$\dot{\vec{x}} = \dot{r}\hat{r} + r\dot{\theta}\hat{\theta} + \dot{z}\hat{z}$$

$$\ddot{\vec{x}} = (\ddot{r} - r\dot{\theta}^2)\hat{r} + (2\dot{r}\dot{\theta} + r\ddot{\theta})\hat{\theta} + \ddot{z}\hat{z}$$

Now equipped with these relations, I can now solve the equations of motion for the beam in region II.

$$m\gamma\ddot{\vec{x}} = qB_o(\dot{\vec{x}} \times \hat{z})$$

$$\ddot{\vec{x}} = 2\omega(r\dot{\theta}\hat{r} - \dot{r}\hat{\theta})$$

I now have three equations of motion by equating the vector components!

$$\ddot{r} - r\dot{\theta}^2 = 2\omega r\dot{\theta}$$

$$2\dot{r}\dot{\theta} + r\ddot{\theta} = -2\omega\dot{r}$$

$$\ddot{z} = 0$$

Now, I get to employ fact that $\dot{\theta} = \text{constant} = -\omega$ to simplify things.

$$\ddot{r} - r\omega^2 = -2\omega^2 r$$

$$-2\dot{r}\omega = -2\omega\dot{r}$$

So everything has simplified to one ODE that I know how to solve!

$$\ddot{r} = -\omega^2 r$$

$$r = Acos(\omega t) + Bsin(\omega t)$$

At the entry of region II we assume no radial velocity (cold beam approximation) so with boundary conditions of $r(0) = r_o$ and $\dot{r}(0) = 0$ then we get the below solution for r. I am also going to employ the paraxial beam approximation

and rewrite the position variable as $t = \frac{z}{v_z}$. I will use r(z) and $\theta(z)$ from here on out when possible.

$$r = r_o cos(\frac{\omega z}{v_z})$$

$$\theta = \theta_o + \omega \frac{z}{v_z}$$

$$\frac{dr}{dz} = -\frac{r_o \omega}{v_z} sin\left(\frac{\omega z}{v_z}\right)$$

And now onto region III. We have another delta function to deal with at $z = L$ where $\vec{B} = \frac{B_o r}{2}\delta(z-L)\hat{r}$. But there are now more vector components to deal with so we'll see what happens. The solenoid is a length L so at the end of region II we have the following velocity vector.

$$\dot{\vec{x}}(z = L) = -r_o \omega sin(\frac{\omega L}{v_z})\hat{r} + r_o \omega cos(\frac{\omega L}{v_z})\hat{\theta} + \dot{z}\hat{z}$$

Now we can do the $\dot{\vec{x}} \times \vec{B}$. We technically get a $\hat{z}$ component but I am going to assume any changes to the longitudinal velocity will be small and negligible and that $\hat{z}$ is ignorable. Now we only have to deal with the θ component of the cross product:

$$\ddot{\vec{x}} = \frac{v_z q}{m\gamma}\frac{B_o r}{2}\delta(z-L)\hat{\theta} = r_o v_z \omega cos\left(\frac{\omega z}{v_z}\right)\delta(z-L)\hat{\theta}$$

$$2\dot{r}\dot{\theta} + r\ddot{\theta} = v_z r_o \omega cos\left(\frac{\omega z}{v_z}\right)\delta(z-L)$$

Let's integrate over t for the t when z= $L-\epsilon$ to $L+\epsilon$. There are some subtleties with this integral. Notably, over this impulse, $\dot{r}$ is unaffected and the integral of $\dot{\theta}$ over the delta function is just $\theta(L+\epsilon) - \theta(L-\epsilon)$ which equals zero. So we only have to deal with the second term!

$$\int r\ddot{\theta}dt = \int_{L-\epsilon}^{L+\epsilon} \omega r(z)\frac{dz}{dt}\delta(z-L)dt$$

$$v_\theta = r\dot{\theta} = \omega r(L) = \omega r_o cos\left(\frac{\omega L}{v_z}\right)$$

$\dot{\theta} = +\omega$ and perfectly cancels the $\dot{\theta}$ we acquired in by going through region I! Now we are past region III and into free space with no field. As a result $\ddot{r} = 0$ so the $\frac{dr}{dz} = r' = \text{constant} = -\frac{r_o\omega}{v_z} sin\left(\frac{\omega L}{v_z}\right)$.

We are now interested in what happens when the solenoid is short or when $\omega L \ll v_z$. We then approximate $sin\left(\frac{\omega L}{v_z}\right)$ as $\frac{\omega L}{v_z}$ to get the r' in this limit.

$$r' = -\frac{\omega^2 r_o L}{v_z^2} = -\frac{r_o L q^2 B_o^2}{v_z^2 4m^2\gamma^2}$$

Now the whole point of this exercise was to determine how much a solenoid focuses the beam. The focal length is the length it takes a parallel ray to be bent to the axis. We can calculate this by investigating an electron that enters at r_o and determining the distance z it takes to reach $r = 0$

$$r(z) = r_o - \frac{r_o L q^2 B_o^2}{v_z^2 4m^2\gamma^2} z$$

$$\text{At r} = 0,\ r_o = \frac{r_o L q^2 B_o^2}{v_z^2 4m^2\gamma^2} z$$

$$\boxed{\text{focal length} = \text{f} = \frac{v_z^2 4m^2\gamma^2}{Lq^2 B_o^2}}$$

A useful observation is that we can write any arbitrary field as a sum of delta functions and Heaviside functions. The v_θ term will cancel after each entrance and exit delta function and all that we are left is the velocity change in r. We

can then rewrite the $B_o^2 L$ as the integral over any magnetic field to get the very useful equation below:

$$r' = -\frac{r_o q^2}{v_z^2 4m^2\gamma^2} \int B^2 dz$$

Appendix B

Off-Axis Field Perturbations

If I know the on-axis $E_o(z)$ field at r=0, how would I calculate how the field changes off-axis?

I will be assuming cylindrical symmetry in a cavity and static fields.

To solve how the field changes off-axis we have to start with equations that govern how fields behave: Maxwell's equations!

$$\text{Gauss's Law: } \nabla \cdot E = \frac{\rho}{\epsilon_o}$$

$$\nabla \cdot B = 0$$

$$\text{Faraday's Law: } \nabla \times E = -\frac{dB}{dt}$$

$$\text{Ampere's Law with Maxwell's correction: } \nabla \times B - \epsilon_o \mu_o \frac{dE}{dt} = \mu_o J$$

However, for this problem, I am assuming static fields and fields in vacuum. Therefore there is no time component or charge density. The equations then reduce to:

$$\nabla \cdot E = 0$$

$$\nabla \cdot B = 0$$

$$\nabla \times E = 0$$

$$\nabla \times B = 0$$

The things I know is the field on axis $E_z(z)|_{r=0} = E_o(z)$ and that $E_r(z)|_{r=0} = 0$. Because I will assume that the off-axis perturbation, it makes sense to write the r component as a Taylor series. I am going to write the equations for E_z and E_r as follows:

$$E_z(r,z) = \sum_{n=0}^{\infty} a_n(z) \cdot r^n$$

$$E_r(r,z) = \sum_{n=0}^{\infty} b_n(z) \cdot r^n$$

With some reasonable thought, there must be x and y even symmetry in our cavities for the E_z component, ie $E_z(x) = E_z(-x)$. Now we have to determine what this means for $E_z(r)$ with $r = \sqrt{(}x^2 + y^2)$. We start by writing E_z in terms of x and y instead of r.

$$E_z(r,z) = \sum_{m=0}^{\infty} \sum_{n=0}^{\infty} a_{n,m}(z) \cdot x^{2n} \cdot y^{2m}$$

We want to see if the even symmetry of x and y can tell use something useful about the r component of E_z. Therefore we take a derivative of E_z with respect to r and see what happens at $r = 0$ to learn about the $a_1(z)$ term.

$$\frac{dE_z}{d_r} = \frac{dE_z}{dx}\frac{dx}{dr} + \frac{dE_z}{dy}\frac{dy}{dr}$$

$$\frac{dE_z}{d_r} = \sum_{m=0}^{\infty}\sum_{n=1}^{\infty} a_{n,m} 2n x^{2n-1} y^{2m} \frac{r}{x} + \sum_{m=1}^{\infty}\sum_{n=0}^{\infty} a_{n,m} 2m x^{2n} y^{2m-1} \frac{r}{y}$$

I can pull out an r which means the $\frac{dE_z}{dr}|_{r=0}$ is zero. This also means that $a_1(z)$ is zero. I will continue taking derivatives to fully demonstrate the pattern but will get sloppy and only note the sums as $\sum$ in the equation. An r will pop out whenever I take a derivative of a $\sum$. The $\sum$ will have some terms that will not be zero and I am only interested on which a_n terms are zero...

$$\frac{dE_z}{dr} = r \cdot \sum = a_1{=}0$$

$$\frac{d^2E_z}{dr^2} = \sum + r^2 \cdot \sum^{'} = a_2 \neq 0$$

$$\frac{d^3E_z}{dr^3} = r \cdot \sum^{'} + 2r \cdot \sum^{'} + r^3 \sum^{''} = a_3{=}\ 0$$

And the pattern continues.... $E_z(z,r)$has only even r terms!! Even better, we can use the even r symmetry in E_z to tell us useful things about E_r using the relation that the $\nabla \times E = 0$. With no E_θ component, $\nabla \times E = 0$ mandates that $\frac{dE_z}{dr} = \frac{dE_r}{dz}$. This means that the r component of the E_r field goes as $\frac{dE_z}{dr}$ meaning r has odd symmetry in $E_r(z,r)$.

Now that we've determine that $E_z(r,z)$ is even and $E_r(r,z)$ is odd we can rewrite our Taylor expansions

$$E_z(r,z) = \sum_{n=0}^{\infty} a_n(z) \cdot r^{2n}$$

$$E_r(r,z) = \sum_{n=0}^{\infty} b_n(z) \cdot r^{2n+1}$$

Now I get to plug these into Maxwell's equation. In cylindrical coordinates,

Gauss's law and Faraday's law produces the following relations that I must satisfy:

$$\frac{dE_r}{dr} + \frac{E_r}{r} + \frac{dE_z}{dz} = 0$$
$$\frac{dE_z}{dr} = \frac{dE_r}{dz}$$

We can do all these derivatives with our Taylor series forms of E_z and E_r. I will look at the top equation first.

$$\frac{E_r}{r} = \sum_{n=0}^{\infty} b_n(z) \cdot r^{2n}$$
$$\frac{dE_r}{dr} = \sum_{n=0}^{\infty} b_n(z) \cdot (2n+1) \cdot r^{2n}$$
$$\frac{dE_z}{dz} = \sum_{n=0}^{\infty} \frac{da_n}{dz} \cdot r^{2n}$$

Putting these all together we get:

$$\sum_{n=0}^{\infty} b_n(z) \cdot r^{2n} + \sum_{n=0}^{\infty} b_n(z) \cdot (2n+1) \cdot r^{2n} + \sum_{n=0}^{\infty} \frac{da_n}{dz} \cdot r^{2n} = 0$$

Now all the summations are the same and have the same order in r. Let's re-organize:

$$\sum_{n=0}^{\infty} r^{2n} \left(b_n(z) \cdot (2n+2) + \frac{da_n}{dz} \right) = 0$$

Each r^{2n} term must equal to zero so we get the relation:

$$b_n(z) = \frac{-1}{2n+2} \frac{da_n}{dz}$$

Luckily from the $E_z(z)|_{r=0} = E_o(z)$ we know that $a_0 = E_o(z)$ so with only 1 out of 2 equations we can get the b_0 term:

$$b_0 = \frac{-1}{2}\frac{dE_o}{dz}$$

However, I would like more than one term so, alas, I have to consult the second equation.

$$\frac{dE_r}{dz} = \sum_{n=0}^{\infty} \frac{db_n}{dz} \cdot r^{2n+1}$$

$$\frac{dE_z}{dr} = \sum_{n=1}^{\infty} a_n \cdot (2n) \cdot r^{2n-1}$$

$$\frac{dE_r}{dz} - \frac{dE_z}{dr} = \sum_{n=0}^{\infty} \frac{db_n}{dz} \cdot r^{2n+1} - \sum_{n=1}^{\infty} a_n \cdot (2n) \cdot r^{2n-1} = 0$$

We now want to group the same order r terms together which gives us the following recursive relationship when we adjust for the different n values:

$$a_n = \frac{1}{2n}\frac{db_{n-1}}{dz}$$

This gives us our solution:

$$\boxed{\begin{aligned} b_n &= \frac{-1}{2n+2}\frac{da_n}{dz} \\ a_n &= \frac{1}{2n}\frac{db_{n-1}}{dz} \end{aligned}}$$

Let's get the first few terms of our field expansions:

$$E_z(z,r) = E_o(z) - \frac{1}{4}\frac{d^2E_o}{dz^2}r^2 + \frac{1}{64}\frac{d^4E_o}{dz^4}r^4 + ...$$

$$E_r(z,r) = -\frac{1}{2}\frac{dE_o}{dz}r + \frac{1}{16}\frac{d^3E_o}{dz^3}r^3 - \frac{1}{96}\frac{d^5E_o}{dz^5}r^5 + ...$$

Bibliography

[1] LCLS homepage, https://lcls.slac.stanford.edu/.

[2] *RF Injector Beam Dynamics Optimization for LCLS-II*, number 5. JACoW, July 2014.

[3] History: of X-rays and Synchrotrons, https://lightsources.org/history/, December 2022.

[4] Ivan V. Bazarov and Charles K. Sinclair. Multivariate optimization of a high brightness DC gun photoinjector. *Phys. Rev. ST Accel. Beams*, 8:14, March 2005.

[5] J. Bisognano et al. Wisconsin SRF electron gun commissioning. In *Proc. NAPAC'13*, 2013.

[6] Philip Bucksbaum and Nora Berrah. Brighter and faster: The promise and challenge of the X-ray free-electron laser. *Physics Today*, 2015.

[7] Bruce Carlsten. Space-charge-induced emittance compensation in high-brightness photoinjectors. *Particle Accelerators*, 49, 1995.

[8] Alexander Wu Chao, Karl Hubert Mess, Maury Tigner, and Frank Zimmermann, editors. *Handbook of Accelerator Physics and Engineering*. World Scientific Publishing Co., second edition, 2013.

[9] Kalyanmoy Deb et al. A fast and elitist multiobjective genetic algorithm: NSGA-II. *Transaction on Evolutionary Computation*, 6(2):182–197, April 2002.

[10] David H. Dowell et al. Results of the SLAC LCLS gun high-power RF tests. Technical report, SLAC National Laboratory, 2007.

[11] Klaus Floettmann. Some basic features of the beam emittance. *Physical Review Special Topics - Accelerators and Beams*, 6(3), 2003.

[12] Klaus Floettmann. *A Space Charge Tracking Algorithm Manual*. DESY, 2017.

[13] Zhirong Huang and Kwang-Je Kim. Review of X-ray free-electron laser theory. *Phys. Rev. ST Accel. Beams*, 10:26, March 2007.

[14] Matthew Johnson. Injector source system functional requirements specification document. Technical Report LCLSII-2.3-FR-0397-R0, SLAC National Accelerator Laboratory, 2015.

[15] R. Kato et al. Construction of an infrared FEL at the compact ERL. In *12th International Particle Accelerator Conference*, 2021.

[16] Kwang-Je Kim, Zhirong Huang, and Ryan Lindberg. *Synchrotron Radiation and Free-Electron Lasers: Principles of Coherent X-Ray Generation*. Cambridge University Press, 2017.

[17] T. Konomi et al. Development of SRF gun applying new cathode idea using a transparent superconducting layer. In *Proc. ERL'17*, 2017.

[18] T. Konomi et al. Development of high intensity, high brightness, CW SRF gun in KEK. In *19th International Conference on RF Superconductivity*, 2019.

[19] Taro Konomi. Overview on worldwide development of SRF-gun cavities. In *2021 International Conference on RF Superconductivity*, 2021.

[20] R. Legg et al. Status of the Wisconsin SRF gun. In *Proceedings of IPAC2012, New Orleans, Louisiana, USA*, 2012.

[21] M. T. Menzel and H. K. Stokes. *User's Guide for the POISSON/SUPERFISH Group of Codes*. Los Alamos National Laboratory, January 1987.

[22] C.E Mitchell et al. Beam dynamics optimization in high-brightness electron injectors. In *38th Free-Electron Laser Conference*, number 38, 2017.

[23] Tsukasa Miyajima. Studies of CERL injector. In *48th ICFA Advanced Beam Dynamics Workshop on Future Light Sources*, 2010.

[24] P. Murcek, A. Arnold, J. Teichert, R. Xiang, P. Lu, H. Vennekate, and P. Kneisel. The SRF photo injector at ELBE - design and status 2013. In *Proceedings of SRF2013, Paris, France*, 2013.

[25] Department of Energy. Accelerators for Americas future. Technical report, Department of Energy, 2010.

[26] Linac Coherent Light Source II High Energy Upgrade (LCLS-II-HE) Project. LCLS-II-HE low emittance injector conceptual design report. Technical Report LCLSIIHE-1.1-DR-0418-R0, SLAC National Accelerator Laboratory, March 2022.

[27] Triveni Rao and David H. Dowell, editors. *An Engineering Guide to Photoinjectors*. CreateSpace Independent Publishing, 2013.

[28] Tor Raubenheimer. LCLS-II-HE FEL facility overview. In *Workshop on Scientific Opportunities for Ultrafast Hard X-Rays at High Rep. Rate*. SLAC, SLAC, 2016.

[29] Martin Reiser. *Theory and Design of Charged Particle Beams*. Wiley-VCH, second edition, 2008.

[30] F. Sannibale et al. Advanced photoinjector experiment photogun commissioning results. *Physical Review Special Topics - Accelerators and Beams*, 15:9, October 2012.

[31] F. Sannibale et al. Status of the APEX project at LBNL. In *Proc. IPAC'14*, 2014.

[32] Amanda Solliday. Scientists see molecules 'breathe' in remarkable detail, July 2017.

[33] LCLS-II Project Team. LCLS-II final design report. Technical report, SLAC National Accelerator Laboratory, 2015.

[34] F. Zhou, Y. Ding, J.P. Duris, S. Gilevich, P. Hering, and S. Vetter. Evaluation of FEL performance with longer injector drive laser pulse at the LCLS. In *Proc. of International Particle Accelerator Conference (IPAC'17), Copenhagen, Denmark, 14-19 May, 2017*, number 8, pages 1651–1654. JACoW, May 2017.